


FULL PAPER

Open Access



# Magma ascent and degassing processes of the 2011 and 2017–18 eruptions of Shinmoedake in Kirishima volcano group, Japan, based on petrological characteristics and volatile content of magmas

Genji Saito<sup>1\*</sup> , Teruki Oikawa<sup>1</sup> and Osamu Ishizuka<sup>1</sup>

## Abstract

The eruption activity of Shinmoedake in the Kirishima volcanic group of Japan resumed in 2017–18, following a quiet period during 2011–17. Subplinian eruptions preceded lava effusion in 2011; however, no subplinian eruption occurred during 2017–18. Petrological studies and melt inclusion analyses were conducted to investigate the ascent and degassing of the magma to understand the cause of the different eruption styles. Chemical analysis of the melt inclusions from the 2011 eruption indicates that mafic magma with high volatile content (6.2 wt% H<sub>2</sub>O, 0.25–1.4 wt% CO<sub>2</sub>) ascended into the shallow felsic magma (1.9–3.7 wt% H<sub>2</sub>O, 0.025–0.048 wt% CO<sub>2</sub>) at depths of 5–6 km. Calculations indicate that the mafic magmas were of lower density (1717–1835 kg m<sup>-3</sup>) than the felsic magma (2264–2496 kg m<sup>-3</sup>) at 125 MPa and that the two magmas were mixed. The 2011 mixed magma with high volatile content (4.0 wt% H<sub>2</sub>O, 0.14–0.70 wt% CO<sub>2</sub>) had a bubble volume of approximately 50 vol% at 50 MPa, which is likely to have caused the subplinian eruption. The whole-rock and chemical compositions of the plagioclase, clinopyroxene, and orthopyroxene phenocryst cores from 2018 and 2011 were similar, suggesting that the 2018 magma was a remnant of the 2011 magma. Chemical analyses of the groundmass from 2018 and the MELTS calculation indicate that the magma approached chemical equilibrium during 2011–18. Melt inclusion analyses and volcanic gas observation noted a lower bulk volatile content in the 2018 magma (2.1–3.0 wt% H<sub>2</sub>O, 0.087–0.10 wt% CO<sub>2</sub>) than that in the 2011 magma. Comparison of the degassed-magma volumes estimated from the S and Cl contents of the melt inclusions, SO<sub>2</sub> flux and volcanic gas composition, and erupted-magma volume indicates that excess degassing has been occurring in the magma due to convection since February 2011, which may have decreased the volatile content of the magma. The relatively low volatile content meant that the 2018 magma could not erupt explosively and lava was instead erupted via effusion.

**Keywords** Kirishima volcano, Shinmoedake, Eruption, Petrology, Magma mixing, Magma ascent, Degassing, Melt inclusions, Volatile content, Bubble volume

\*Correspondence:

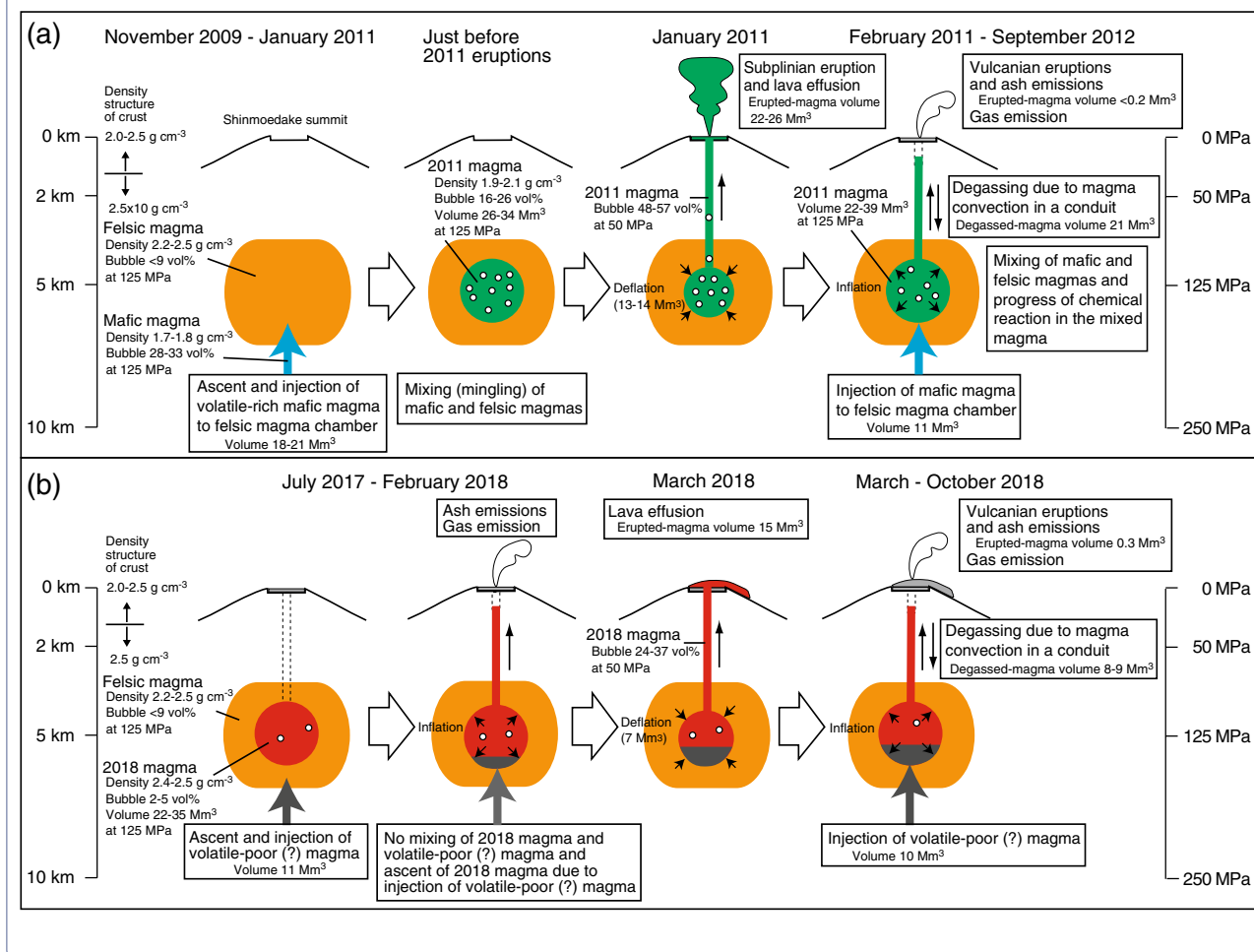
Genji Saito  
saito-g@aist.go.jp

Full list of author information is available at the end of the article



© The Author(s) 2023. **Open Access** This article is licensed under a Creative Commons Attribution 4.0 International License, which permits use, sharing, adaptation, distribution and reproduction in any medium or format, as long as you give appropriate credit to the original author(s) and the source, provide a link to the Creative Commons licence, and indicate if changes were made. The images or other third party material in this article are included in the article's Creative Commons licence, unless indicated otherwise in a credit line to the material. If material is not included in the article's Creative Commons licence and your intended use is not permitted by statutory regulation or exceeds the permitted use, you will need to obtain permission directly from the copyright holder. To view a copy of this licence, visit <http://creativecommons.org/licenses/by/4.0/>.

**Graphical Abstract**



**Introduction**

The behavior of volatiles in magma chambers is a highly important factor that influences and controls eruptions. A vapor phase of  $>5$  vol% that accumulated in the magma chamber of Mt. Pinatubo in 1991 may have been associated with the Plinian eruption that occurred shortly after (Gerlach et al. 1996). However, the effective degassing of magma in the chamber of an approximately  $1 \text{ km}^3$  dacitic-lava dome at Mt. Unzen in 1991–95 resulted in an effusive eruption (Ohba et al. 2008). These results indicate that eruption styles depend on the volatile content and degassing processes of a magma chamber. Therefore, studying the volatile behavior and degassing processes of magmas is important to better understand the mechanisms underlying the volcanic eruption. Petrological investigation of volcanic rocks allow elucidation of the physical and chemical conditions of a magma chamber, including factors such as temperature, chemical

composition, and the properties of an end-member magma if mixing occurred. Melt-inclusion analysis is a powerful method for estimating the volatile content of the melt in a magma prior to eruption [e.g., Anderson 1973; Anderson et al. 1989; Johnson et al. 1994; Lowenstern 2003]. Because melt inclusions preserve the chemical compositions of a melt during phenocryst growth, the volatile content of the melt in each end-member magma resulting from the magma-mixing process can be estimated. Moreover, combining melt-inclusion analysis with volcanic gas observation can be used to estimate the volume of a degassed magma (e.g., Kazahaya et al. 2004; Saito et al. 2018).

This study is an investigation of the magma ascent and degassing processes that occurred during a series of eruptions from 2011–18 at Shinmoedake in the Kirishima volcanic group. The 2011 eruptions were marked by a series of phreatomagmatic and subplinian

eruptions followed by vulcanian explosions and effusion of lava within the summit crater during January–February (Nakada et al. 2013). The volcano had intermittent vulcanian eruptions and ash emissions through September 2011 (Nakada et al. 2013). Degassing activity was observed throughout the 2011 eruption series until September 2012 (Mori and Kato 2013; JMA 2014). The 2017–18 eruptions started with small ash eruptions in October 2017, followed by vulcanian explosions and lava effusion in the summit crater during March 2018; however, no subplinian eruptions occurred. Such differences provide an opportunity to investigate the relationship between eruption style and the physical and chemical conditions of a magma. Petrological studies and melt-inclusion analyses of the Shinmoedake eruptions were therefore conducted to understand the physical and chemical conditions in the magma chambers and the amount of degassed magma present during the different active periods. Geological, geophysical, and geochemical observations were thus combined to model the magma ascent and degassing

processes during the 2011 and 2017–18 Shinmoedake eruptions.

**Overview of the Kirishima volcanic group and the 2011 and 2017–18 Shinmoedake eruptions**

The Kirishima volcanic group is located in southern Kyushu, Japan (Fig. 1). The group extends over an area of approximately 20 × 30 km<sup>2</sup> and contains more than 20 small volcanoes (Imura and Kobayashi 2001). Historically, the group can be divided into older and younger volcanoes. Activity in the older volcanoes began at approximately 1.2 Ma and continued until several hundred thousand years ago, whereas the younger volcanoes first became active approximately 300 ka, with activity continuing to the present time. The composition of the rocks in the younger Kirishima volcanoes ranges from olivine basalt to pyroxene andesite and hornblende-bearing pyroxene dacite. Shinmoedake, one of the younger volcanoes, first became active at approximately 18 ka. Since 742, all eruptions have occurred at the Shinmoedake and Ohachi volcanoes in the southeastern part of

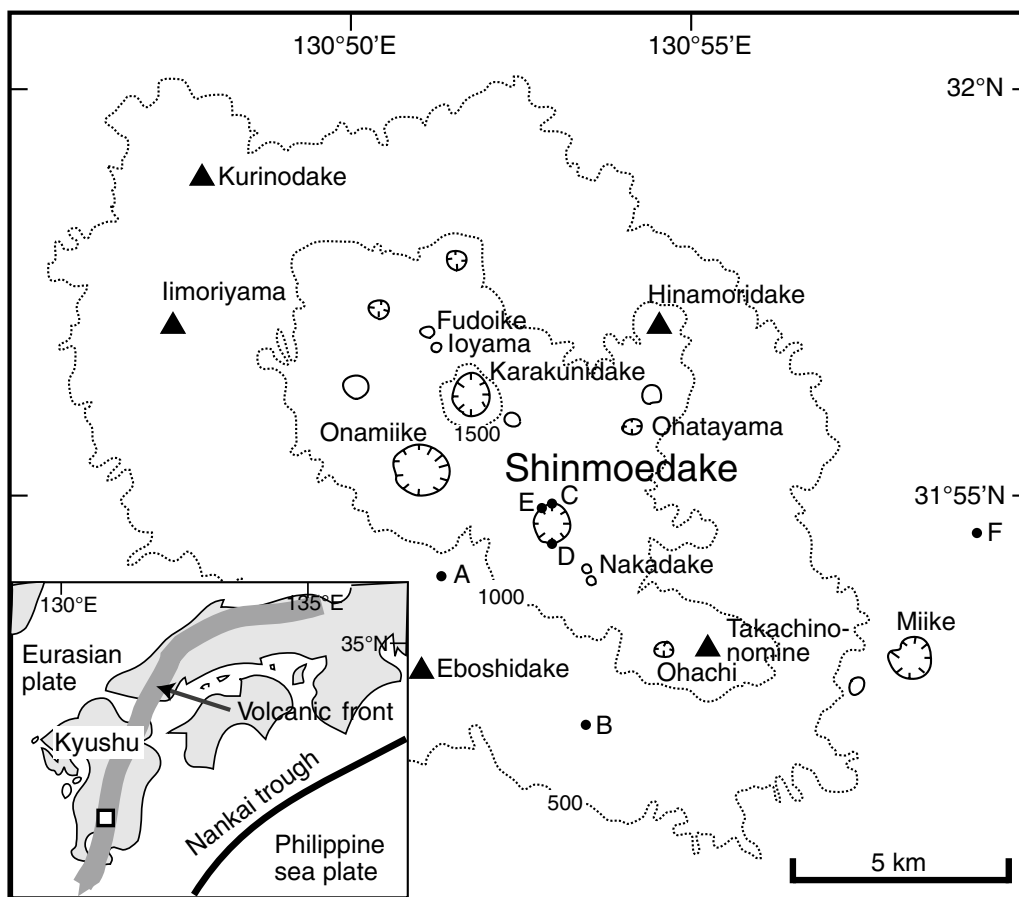


**Fig. 1** Location map showing Shinmoedake, part of the Kirishima volcanic group. Sampling points (A–F) are also shown. **A**: 2018-1VGP and 2018-1VS, **B**: 2018-2VGP and 2018-2VS, **C**: 2018-3BB1, **D**: 2018-3BB2 to BB3, **E**: 2018-4L1 to L5, and **F**: 1235S. Refer to Table 1 for sample names

the Kirishima volcanic group, except for Ioyama (Fig. 1). The eruptions at Ohachi in 788 and 1235 and at Shinmoedake over 1716–17 were explosive and ejected pyroclastic flows that caused significant disasters. Some minor and phreatic eruptions also occurred at Shinmoedake in 1959, 1991, and 2008 (Geshe et al. 2010).

The 2011 series of Shinmoedake eruptions started with phreatomagmatic eruptions on 19 January 2011 (Kato and Yamasato 2013; Miyabuchi et al. 2013; Nakada et al. 2013). Three subplinian eruptions on 26–27 January (the “P1, P2, and P3 events”) produced a total tephra mass of  $1.7\text{--}2.8 \times 10^{10}$  kg (Maeno et al. 2014). These eruptions were followed by lava effusion within the summit crater (28 January–1 February) and vulcanian explosions. A dense-rock equivalent (DRE) of approximately  $15 \times 10^6$  m<sup>3</sup> of effused lava was produced (Kozono et al. 2013; Nakada et al. 2013). The Global Positioning System (GPS) observations indicated that the volcano was undergoing continuous inflation from December 2009 (Kawamoto et al. 2011), whereas significant deflation by approximately  $13\text{--}14 \times 10^6$  m<sup>3</sup> was observed as a result of the subplinian eruptions and lava effusion (GIAJ 2012; Nakao et al. 2013; JMA 2019a). Vulcanian explosions and continuous ash emissions from the summit crater occurred intermittently between February–September (Nakada et al. 2013), and an estimated  $4.2 \times 10^8$  kg of tephra was erupted during seven events from 24 February to 7 September (Nishiki et al. 2013). Petrological study of ash samples from the eruptions during March–June indicated that more than half of the volume of the ash was composed of essential material (Oishi et al. 2013; Suzuki et al. 2013a). GPS observation indicated that inflation restarted on 2 February and continued until November 2011, at which point it ceased (Nakao et al. 2013). The intense gas emission that started with the eruptive activity peaked at  $490 \text{ kg s}^{-1} \text{ SO}_2$  ( $42,600 \text{ t d}^{-1} \text{ SO}_2$ ) on 28 January (Mori and Kato 2013), after which it gradually decreased to reach approximately  $1 \text{ kg s}^{-1} \text{ SO}_2$  by the end of 2011 (Mori and Kato 2013).

The activity then resumed with small eruptions of ash on 11–16 October 2017 after a rest period of approximately 6 y. A small ash eruption that started on 1 March 2018 rapidly changed to ash eruptions with vulcanian explosions and lava effusion within the summit crater on 6 March 2018. The lava effusion continued until 9 March, and the vulcanian explosions and ash eruptions continued intermittently until 27 June 2018. One difference observed in the 2011 and 2017–18 eruption styles is that subplinian eruptions did not occur in 2017–18. Approximately  $15 \times 10^6$  m<sup>3</sup> DRE of effused lava was produced during this period (Chiba et al. 2018; Oikawa et al. 2018). Continuous inflation of the volcano observed from 1 July 2017 to 1 March 2018 (JMA 2019b) was followed

by deflation of approximately  $7 \times 10^6$  m<sup>3</sup> (JMA 2019a) during the vulcanian eruptions and the lava effusion of 1–10 March 2018. The inflation then restarted and continued until 31 January 2019. The intense gas emission that started in October 2017 and peaked at  $390 \text{ kg s}^{-1} \text{ SO}_2$  ( $34,000 \text{ t d}^{-1} \text{ SO}_2$ ) on 7 March 2018 (JMA 2019b) decreased gradually to reach approximately  $1 \text{ kg s}^{-1}$  by October 2018 (JMA 2019a).

## Sampling and analytical methods

### Samples

The analyzed eruptive products from the 1716–17 and 2011 Shinmoedake volcanic eruptions (Table 1) include gray- and white-colored pumices from the 1716–17 eruption (hereafter “1716-17GP” and “1716-17WP,” respectively; Table 1), pumices from the phreatomagmatic eruption on 19 January 2011 (hereafter “2011-1PP”), gray and white pumices from the subplinian eruptions during events P2 and P3 on 26–27 January 2011 (hereafter “2011-2SGP and 2011-2SWP” for event P2 and “2011-3SGP” for event P3), and a bomb and lapillus from the vulcanian explosions of February 2011 (“2011-4VB” and “2011-5 VL”). Although both gray and white pumices were ejected during the 2011 subplinian eruptions (Suzuki et al. 2013b; Tomiya et al. 2013), the majority was gray. Ash particles and lapilli from the vulcanian and ash eruptions during March–August 2011 were also examined in this study (“2011-6VA,” “2011-7VL,” “2011-8A,” and “2011-9A;” Table 1) along with eruptive products from the 2018 eruptions (Table 1); gray-colored pumices and scoria from the vulcanian explosion on 6 and 9 March 2018 (hereafter “2018-1VGP” and “2018-1VS” for the 6 March products and “2018-2VGP” and “2018-2VS” for the 9 March products; Table 1), three ballistic blocks from the vulcanian eruptions (“2018-3BB1, BB2, and BB3”), two dark-gray and lithic lava fragments (“2018-4L1 and L2”), a gray and porous lava fragment (“2018-4L3”), and a banded and porous lava fragment (“2018-4L4, L5”). Scoria from the 1235 eruption of Ohachi volcano was also analyzed (“1235S” in Table 1). Detailed descriptions of the samples are summarized in Table 1 and their sampling locations are noted in Fig. 1.

### Analytical methods

The major-element compositions of the 1235S, 2011-7VL, and 2018 eruptive products were determined using wavelength-dispersive X-ray fluorescence analysis (XRF; Table 2; Additional file 1; Ishizuka et al. 2014). Glass beads, prepared by fusing 1:10 mixtures of 0.5 g subsamples and lithium tetraborate, were analyzed using a Panalytical Axios XRF spectrometer at the Geological Survey of Japan (GSJ), Advanced Industrial Science and Technology (AIST). The pumices, scoria, bomb, lapilli, ashes, and

**Table 1** Sample list of rock samples from the Kirishima volcano analyzed in this study

Date and location	Eruption style <sup>a</sup>	Sample description <sup>b</sup>	Sampling points in Fig. 1	Sample name in this study <sup>c</sup>	Abbreviation for inclusion No	MI analysis <sup>d</sup>
1235 eruption at Ohaci volcano	Magmatic	Scoria (150 mm)	F	1235S	TS	4/4
1716–17 eruptions at Shinmoedake	Phreatic to magmatic	Gray pumices (~0.5 mm)		1716-17GP	KP	4/16
	Phreatic to magmatic	White pumices		1716-17WP		
2011 eruptions at Shinmoedake						
19 January	Preatomagmatic	Gray pumices (~0.5 mm)		2011-1PP	11-1P	7/10
26–27 January (event P2)	Subplinian	Gray pumices (16~20 mm)		2011-2SGP	11-2SG	18/31
26–27 January (event P2)	Subplinian	White pumices (2–12 mm)		2011-2SWP	11-2SW	0/5
26–27 January (event P3)	Subplinian	Gray pumices (16~20 mm)		2011-3SGP	11-3SG	0/10
1 February	Vulcanian and lava flow	A bomb		2011-4VB	11-4V	7/12
14 February	Vulcanian	A lapillus (~30 mm)		2011-5VL	11-5V	0/7
13 March	Vulcanian	Ash particles (1–3 mm)		2011-6VA	11-6V	0/2
18 April	Vulcanian	Lapilli (5–10 mm)		2011-7VL	11-7V	0/2
29 June	Continuous ash emission	Ash particles (0.25–0.50 mm, P, S and GG-types)		2011-8A	11-8	
31 August	Continuous ash emission	Ash particles (0.25–0.50 mm, S and GG-types)		2011-9A	11-9	
2018 eruptions at Shinmoedake						
6 March	Vulcanian and lava flow	Gray pumices (1~10 mm)	A	2018-1VGP	18-1V	9/24
6 March	Vulcanian and lava flow	Scoria (1~10 mm)	A	2018-1VS		
9 March	Vulcanian and lava flow	Gray pumices (2~10 mm)	B	2018-2VGP		
9 March	Vulcanian and lava flow	Scoria (2~10 mm)	B	2018-2VS		
March	Vulcanian and lava flow	Ballistic blocks (3 blocks)	C, D	2018-3BB1, BB2, BB3		
March	Vulcanian and lava flow	Dark-gray and lithic lava fragments	E	2018-4L1, L2		
March	Vulcanian and lava flow	A gray and porous lava fragment	E	2018-4L3		
March	Vulcanian and lava flow	A banded and porous lava fragment	E	2018-4L4, L5		

<sup>a</sup> The eruption styles of the 2011 eruptions are after Nakada et al. (2013)

<sup>b</sup> P, S, GG-types were defined for the ash particles by Oishi et al. (2013)

<sup>c</sup> 2018-4L4 is a dark-gray part of the banded and porous lava fragment and 2018-4L5 is a gray part of it

<sup>d</sup> x/y; x, number of melt inclusions analyzed by SIMS; y, total number of melt inclusions analyzed in this study

lava fragments from the 2011 and 2018 eruptions were mounted in epoxy resin, ground with sandpaper, and polished with diamond powder (1 μm). The mode compositions and porosities of the samples were determined

using backscattered electron (BSE) images by scanning electron microscopy (SEM; Additional file 2). Chemical analyses of the phenocrysts, melt-inclusions, groundmass microlites (<0.1 mm), and the bulk composition of the

**Table 2** Whole-rock compositions (in weight percent) of volcanic rocks from the 1716–17, 2011, and 2018 eruptions of the Shinmoedake volcano, 1235 eruption of the Ohachi volcano, and 7 ka eruption of the Takachihonome volcano. Refer to Table 1 for sample names

Sample name	7 ka lava <sup>a</sup>	1235S	1716-17GP <sup>b</sup>			1716-17WP <sup>b</sup>					
Notes											
SiO <sub>2</sub>	53.63	53.58	57.82 (0.65)			63.01					
TiO <sub>2</sub>	0.89	0.80	0.75 (0.02)			0.72					
Al <sub>2</sub> O <sub>3</sub>	19.06	19.16	17.55 (0.21)			16.56					
FeOt	8.98	8.29	7.48 (0.33)			5.61					
MnO	0.15	0.16	0.14 (0.01)			0.11					
MgO	3.77	4.54	4.06 (0.24)			2.45					
CaO	9.07	9.84	7.70 (0.18)			6.22					
Na <sub>2</sub> O	3.25	2.81	2.90 (0.09)			2.91					
K <sub>2</sub> O	1.21	0.81	1.59 (0.10)			2.42					
Sample name	2011-2SGP <sup>b</sup>	2011-2SWP <sup>b</sup>	2011-3SGP <sup>b</sup>	2011-4VB <sup>b</sup>	2011-5VL <sup>b</sup>	2011-7VL					
Notes						5 fragments					
SiO <sub>2</sub>	57.87 (0.32)	63.24 (0.10)	57.28 (0.46)	57.73 (0.06)	57.36 (0.97)	57.55					
TiO <sub>2</sub>	0.71 (0.02)	0.06 (0.01)	0.74 (0.04)	0.72 (0.00)	0.71 (0.02)	0.71					
Al <sub>2</sub> O <sub>3</sub>	17.48 (0.26)	16.66 (0.11)	17.33 (0.64)	17.41 (0.26)	17.58 (0.73)	17.11					
FeOt	7.36 (0.22)	5.46 (0.04)	7.73 (0.55)	7.47 (0.13)	7.65 (0.30)	7.79					
MnO	0.14 (0.01)	0.11 (0.00)	0.15 (0.01)	0.15 (0.01)	0.15 (0.01)	0.15					
MgO	4.10 (0.18)	2.71 (0.07)	4.41 (0.49)	4.31 (0.26)	4.43 (0.36)	4.53					
CaO	7.81 (0.15)	6.18 (0.15)	7.97 (0.19)	7.79 (0.07)	7.76 (0.14)	7.72					
Na <sub>2</sub> O	2.91 (0.04)	3.15 (0.00)	2.85 (0.13)	2.86 (0.03)	2.83 (0.08)	2.88					
K <sub>2</sub> O	1.60 (0.05)	2.44 (0.03)	1.54 (0.11)	1.57 (0.00)	1.52 (0.08)	1.57					
Sample name	2018-1VGP	2018-2VGP	2018-2VS	2018-3BB1	2018-3BB2	2018-3BB3	2018-4L1	2018-4L2	2018-4L3	2018-4L4	2018-4L5
Notes		3 fragments	5 fragments	Porous	Porous	Lithic	Dark gray, lithic	Dark gray, lithic	Gray, porous	Dark gray, porous	Gray, porous
SiO <sub>2</sub>	58.15	58.80	58.39	58.17	58.18	58.27	58.21	58.21	62.65	58.41	63.04
TiO <sub>2</sub>	0.68	0.69	0.70	0.71	0.71	0.69	0.71	0.72	0.66	0.71	0.66
Al <sub>2</sub> O <sub>3</sub>	18.13	17.48	17.79	17.35	17.52	17.53	17.45	17.41	16.26	17.32	16.13
FeOt	6.71	6.86	6.89	7.29	7.09	7.05	7.19	7.18	5.78	7.13	5.70
MnO	0.12	0.13	0.13	0.14	0.14	0.14	0.14	0.14	0.12	0.14	0.12
MgO	3.92	3.97	3.94	4.13	3.98	4.10	4.04	4.17	2.91	4.09	2.87
CaO	7.79	7.43	7.64	7.60	7.76	7.60	7.66	7.57	6.12	7.55	5.94
Na <sub>2</sub> O	2.94	2.93	2.88	2.95	2.94	2.96	2.94	2.96	3.09	2.97	3.09
K <sub>2</sub> O	1.57	1.69	1.65	1.64	1.67	1.67	1.65	1.64	2.42	1.68	2.46

FeOt, total iron as FeO. The chemical compositions are recalculated to 100%

Chemical compositions of 1235S, 2011-7VL, 2018 eruption products were measured using XRF in this study. Analytical errors for each element are shown in Ishizuka et al. (2014)

<sup>a</sup> Chemical composition of lava of 7 ka eruption at Takachihonome volcano is after Imura and Kobayashi (2001)

<sup>b</sup> Chemical compositions of 1716-17GP, 1716-17WP, 2011-2SGP and 2011-3SGP, 2011-2SWP, 2011-4VB and 2011-5VL are after Tomiya et al. (2013). Standard deviation of each analysis is also shown in parenthesis

groundmass were performed using electron probe micro-analyzers (EPMA; JEOL JXA-8900 at GSJ, AIST). The experimental conditions used for the analysis of minerals and groundmass were identical to those reported by Saito et al. (2001, 2002). Compositional profiles across the olivine, plagioclase, and pyroxene phenocrysts from core to rim were also determined by EPMA. The major-element and minor S and Cl contents of the melt inclusions were determined by EPMA, with accelerating voltage of 15 keV, beam current of 10 nA, and defocused beam with a diameter of 5  $\mu\text{m}$  (Table 3). The S K $\alpha$  radiation wavelength was used for S analysis to determine the sulfide and sulfate proportions in the inclusions (Wallace and Carmichael 1994).

The H<sub>2</sub>O and CO<sub>2</sub> contents of the melt inclusions in the eruptive products from 1235, 1716–17, 2011, and 2018 were measured by secondary ion mass spectrometry (SIMS) (Tables 1 and 3). The mounted samples were polished with Al<sub>2</sub>O<sub>3</sub> powder (1  $\mu\text{m}$ ) and coated with gold prior to the SIMS analyses with a Cameca ims-1270 SIMS (installed at GSJ, AIST). Cs<sup>+</sup> ions were used in the analyses as the primary beam and negatively charged secondary <sup>1</sup>H, <sup>12</sup>C, and <sup>30</sup>Si ions were collected (Hauri et al. 2002). A detailed description of the SIMS analyses performed can be found in Saito et al. (2010, 2018). A Cameca nanoSIMS 50L (installed at GSJ, AIST) was used to measure the H<sub>2</sub>O and CO<sub>2</sub> contents in the melt inclusions from the 2018 eruptions. The analyses used focused Cs<sup>+</sup> ions and scanned 5  $\times$  5  $\mu\text{m}^2$  on the polished section's surface. The negatively charged-secondary ion count ratio of <sup>12</sup>C/<sup>30</sup>Si and <sup>16</sup>OH/<sup>30</sup>Si was used for CO<sub>2</sub> and H<sub>2</sub>O analysis. A detailed description of the nanoSIMS analyses performed can be found in Miyagi et al. (2023). A normal-incidence electron gun was used for charge compensation of the sample based on the methods by Kita et al. (2004). SIMS calibration lines were made for H<sub>2</sub>O and CO<sub>2</sub> on each measurement day using the reference glasses. Repeated analyses of the same melt inclusions indicated an analytical error of not more than  $\pm 0.2$  wt % for H<sub>2</sub>O and  $\pm 0.0028$  wt % for CO<sub>2</sub> (Saito et al. 2010).

## Results

### Whole-rock and mode compositions

Major-element composition of 1235S is basaltic andesite and is similar to lava from the 7-ka eruption at Takachi-honimine (Table 2). The products of the 2011 eruptions (2011-2SGP, 2011-3SGP, 2011-4VB, 2011-5VL, and 2011-7VL) were found to have an andesite composition (SiO<sub>2</sub> = 57–58 wt.%) similar to that of 1716-17GP (Table 2; Fig. 2). Dacite composition of 2011-2SWP (SiO<sub>2</sub> = 63 wt.%) is similar to that of 1716-17WP.

Suzuki et al. (2013b) concluded that most of the ejecta from the 2011 eruptions are mixed magma products (SiO<sub>2</sub> = 57–58 wt.%, 960–980 °C) of felsic (silicic andesite with SiO<sub>2</sub> = 62–63 wt.% and 870 °C) and mafic magma (basaltic andesite with SiO<sub>2</sub> = 55 wt.% and 1030 °C). The products of the 2011 eruptions (2011-2SGP, 2011-3SGP, 2011-4VB, 2011-5VL, and 2011-7VL) with andesite composition are therefore mixed products and 2011-2SWP, with a dacite composition, was derived from the silicic andesite magma chamber.

The products of the 2018 eruptions have SiO<sub>2</sub> content of 58–59 wt% and K<sub>2</sub>O content of 1.6–1.7 wt%, which is similar or slightly more evolved than 2011-2SGP and 2011-3SGP. However, the porous gray lava samples from the 2018 eruptions (2018-4L3 and 2018-4L5) (Table 2; Fig. 2) and 2011-2SWP have similar chemical compositions. This result indicates that two different magmas that were similar to those from 2011 and 1716–17 were erupted in 2018; one was an andesitic magma with SiO<sub>2</sub> = 57–59 wt% and K<sub>2</sub>O = 1.5–1.7 wt% and the other was dacite with SiO<sub>2</sub> = 63 wt% and K<sub>2</sub>O = 2.4–2.5 wt%. This suggests that the same magma system was present at least from 1716–17 to 2018. Composition of 2011-2SGP and 2011-3SGP: 20–21 vol% plagioclase phenocrysts, 1–2 vol% clinopyroxene and orthopyroxene phenocrysts, <1 vol% olivine phenocrysts, <1 vol% Fe–Ti oxides, and 72–74 vol% groundmass (Additional file 2). Mode composition of 2011-2SWP is similar to that of the subplinian gray pumice. Mode compositions of 2011-4VB, 2011-5VL, 2011-6VA, and 2011-7VL are similar to those of the subplinian gray pumices from January 2011; however, their groundmass contents (66–71 vol%) are slightly lower. The porosities of products from the subplinian eruptions (42–54 vol% of 2011-2SGP, 2011-2SWP, and 2011-3SGP) are a little higher than those of the vulcanian bomb, ash, and lapilli (2–40 vol% of 2011-4VB, 2011-5VL, 2011-6VA, and 2011-7VL; Additional file 2). Composition of 2018-1VGP and 2018-2VGP: 20–22 vol% plagioclase phenocrysts, 8 vol% clinopyroxene and orthopyroxene phenocrysts, <1 vol% Fe–Ti oxides, and 70–72 vol% groundmass (Additional file 2). Samples 2018-1VS and 2018-2VS have slightly less plagioclase (16–17 vol%) and a slightly higher pyroxene content (11 vol% clinopyroxene and orthopyroxene phenocrysts) than the vulcanian gray pumices, although they have similar groundmass contents (72–73 vol%). The groundmass contents of 2018-4L1, 2018-4L2 (67–69 vol%), and 2018-4L3 (54 vol%) are lower than those of the vulcanian gray pumices and scoria. Sample 2018-4L3 has the highest phenocryst content of 46 vol% (and the lowest groundmass content of 54 vol%). Considering its SiO<sub>2</sub> content (62.65 wt%; Table 2), it is likely a

**Table 3** Chemical compositions (in weight percent) of melt inclusions in the phenocrysts within eruptives from the 1235, 1716–17, 2011, and 2018 eruptions analyzed by EPMA and SIMS. The major element compositions were recalculated on a volatile (H<sub>2</sub>O, CO<sub>2</sub>, S, and Cl)-free basis. Refer to Table 1 for sample names and inclusion numbers

Sample name	12355				1716-17GP			
	TS-p1i1	TS-p2i1	TS-p3i1	TS-p3i2	KP-p1i1	KP-p2i1	KP-p3i1	KP-p4i1
Inclusion No <sup>a</sup>	TS-p1i1	TS-p2i1	TS-p3i1	TS-p3i2	KP-p1i1	KP-p2i1	KP-p3i1	KP-p4i1
Host phenocryst <sup>b</sup>	ol	cpx	cpx	cpx	pl	cpx	cpx	cpx
Host chemistry <sup>c</sup>	Fo73	Wo41En41Fs18	Wo41En44Fs15	Wo41En44Fs14	An63	Wo42En42Fs16	Wo42En42Fs16	Wo44En41Fs15
Inclusion size (max, mm)	0.05	0.06	0.03	0.04	0.08	0.06	0.05	0.05
Accompanying phase <sup>d</sup>								
Bubble (vol%) <sup>e</sup>								
Overgrowth (in weight) <sup>f</sup>	0.053							
SiO <sub>2</sub>	59.44	63.45	68.14	65.90	72.91	72.03	71.14	62.17
TiO <sub>2</sub>	1.16	0.57	1.05	1.14	0.66	0.66	0.74	0.92
Al <sub>2</sub> O <sub>3</sub>	15.26	15.08	17.12	17.27	14.49	13.26	13.17	15.74
FeOt	8.37	5.68	2.67	2.87	1.60	3.48	3.94	7.26
MnO	0.18	0.20	0.08	0.11	0.04	0.10	0.10	0.19
MgO	3.57	2.86	1.03	1.64	0.26	0.85	0.84	1.86
CaO	7.92	6.80	4.58	5.82	2.53	2.87	2.57	5.55
Na <sub>2</sub> O	2.79	3.39	3.76	3.70	3.03	2.81	2.82	3.54
K <sub>2</sub> O	1.31	1.96	1.57	1.54	4.48	3.94	4.69	2.79
S	0.065	0.012	0.079	0.086	0.014	0.014	0.005	0.040
Cl	0.076	0.039	0.088	0.101	0.150	0.105	0.135	0.101
H <sub>2</sub> O <sup>g</sup>	3.1	3.7	3.1	3.2	2.0	2.4	2.6	0.8
CO <sub>2</sub> <sup>g</sup>	0.023	n.a	0.004	0.014	0.040	0.012	0.008	0.000
S(+6)/total S <sup>h</sup>	0.8	n.a	n.a	0.9	0.9	0.9	n.a	1.0
log fO <sub>2</sub> <sup>i</sup>	-9	n.a	n.a	-9	-10	-10	n.a	-9
Fe(+2)/total Fe <sup>j</sup>	0.7	n.a	n.a	0.7	0.7	0.7	n.a	0.6
FMQ (log unit) <sup>j</sup>	2.1	n.a	n.a	2.2	2.5	2.3	n.a	3.4
Sat. Press. (MPa) <sup>k</sup>	156/-	-/-	89/-	113/-	106/95	71/-	71/-	7/-
Temperature (°C) <sup>l</sup>	(919)	(1053)	989	(1031)	953	969	(960)	1014
Pressure (MPa) (host-liquid) <sup>l</sup>	-	(520)	460	(470)	-	630	(570)	250
K <sub>D</sub> <sup>m</sup>	(0.19)	(0.48)	0.30	(0.41)	0.06	0.20	(0.18)	0.21
Sample name	2011-1PP							
Inclusion No. <sup>a</sup>	11-1P-p1i1	11-1P-p1i2	11-1P-p1i3	11-1P-p2i1	11-1P-p3i1	11-1P-p4i1	11-1P-p5i1	
Host phenocryst <sup>b</sup>	ol	ol	ol	ol	ol	ol	ol	
Host chemistry <sup>c</sup>	Fo76	Fo75	Fo75	Fo74	Fo75	Fo76	Fo76	
Inclusion size (max, mm)	0.09	0.05	0.04	0.04	0.07	0.06	0.04	
Accompanying phase <sup>d</sup>	A bubble (0.02)				A bubble (0.02)	A bubble (0.02)	Bubbles (<0.001)	
Bubble (vol%) <sup>e</sup>	1				2	4	<0.002	
Overgrowth (in weight) <sup>f</sup>	0.024			0.009		0.003	0.037	
SiO <sub>2</sub>	61.16	58.60	56.98	56.49	57.88	55.22	59.36	
TiO <sub>2</sub>	0.75	0.78	0.99	0.73	0.74	0.98	0.00	
Al <sub>2</sub> O <sub>3</sub>	14.21	17.37	17.92	17.38	18.21	19.58	18.52	
FeOt	7.88	7.45	7.92	7.59	6.54	7.58	5.82	
MnO	0.17	0.15	0.16	0.11	0.12	0.15	0.12	
MgO	3.28	3.18	3.26	2.68	3.11	3.05	2.58	
CaO	6.90	8.31	8.23	8.25	8.98	9.45	8.97	
Na <sub>2</sub> O	2.81	2.89	3.23	5.31	3.28	2.86	3.35	
K <sub>2</sub> O	2.84	1.27	1.30	1.45	1.14	1.12	1.27	





**Table 3** (continued)

Sample name	2011-2SGP								
$K_D^m$	0.31	0.26	0.32	(0.22)	0.26	(0.24)	(0.36)	0.33	0.30
Sample name	2011-2SGP								
Inclusion No. <sup>a</sup>	11-2SG-p8i1	11-2SG-p9i1	11-2SG-p10i1	11-2SG-p11i1	11-2SG-p12i1	11-2SG-p13i1	11-2SG-p13i2	11-2SG-p14i1	11-2SG-p15i1
Host phenocryst <sup>b</sup>	ol	ol	ol	ol	cpx	opx	opx	opx	opx
Host chemistry <sup>c</sup>	Fo76	Fo77	Fo77	Fo78	Wo43En40Fs17	Wo2En65Fs33	Wo2En64Fs34	Wo3En64Fs33	Wo3En66Fs32
Inclusion size (max, mm)	0.07	0.05	0.04	0.04	0.02	0.09	0.06	0.08	0.04
Accompanying phase <sup>d</sup>	A bubble(0.015)			A bubble(0.01)					
Bubble (vol%) <sup>e</sup>	1			2					
Overgrowth (in weight) <sup>f</sup>		0.002	0.008	0.010					
SiO <sub>2</sub>	57.71	56.07	55.94	52.49	73.33	74.23	73.52	71.62	72.31
TiO <sub>2</sub>	0.85	0.89	0.82	0.89	0.45	0.29	0.37	0.55	0.46
Al <sub>2</sub> O <sub>3</sub>	17.05	17.86	18.64	20.19	12.49	12.37	12.27	13.31	13.21
FeO <sup>t</sup>	8.34	8.53	7.97	8.13	2.70	3.50	4.09	4.32	3.59
MnO	0.20	0.15	0.20	0.15	0.10	0.06	0.10	0.06	0.07
MgO	3.85	3.84	3.51	3.70	0.74	1.00	1.08	1.01	0.90
CaO	8.17	8.99	8.99	9.56	2.28	2.03	2.16	2.47	2.12
Na <sub>2</sub> O	2.64	2.63	2.89	4.01	3.57	2.71	2.83	2.61	2.87
K <sub>2</sub> O	1.19	1.04	1.04	0.88	4.34	3.81	3.58	4.04	4.47
S	0.155	0.156	0.170	0.168	0.009	0.007	0.013	0.003	0.015
Cl	0.062	0.056	0.053	0.057	0.118	0.087	0.087	0.113	0.112
H <sub>2</sub> O <sup>g</sup>	4.6/4.7	7.0	5.9	3.0/3.1	1.4	3.7	3.5	3.6	2.6
CO <sub>2</sub> <sup>g</sup>	0.018/0.048	0.019	0.025	0.012/0.057	0.013	0.048	0.002	0.013	0.012
S(+6)/total S <sup>h</sup>	n.a	0.8	n.a	n.a	n.a	n.a	n.a	n.a	n.a
log fO <sub>2</sub> <sup>i</sup>	–	–9	–	–	–	–	–	–	–
Fe(+2)/total Fe <sup>l</sup>	–	0.7	–	–	–	–	–	–	–
FMQ (log unit) <sup>j</sup>	–	2.0	–	–	–	–	–	–	–
Sat. Press. (MPa) <sup>k</sup>	254/186	478/-	386/-	121/-	36/-	174/167	91/-	111/-	69/-
Temperature (°C) <sup>l</sup>	1001	966	958	995	946	990	1053	985	981
Pressure (MPa) (host-liquid) <sup>l</sup>	–	–	–	–	380	–	230	–	–
$K_D^m$	0.31	0.30	0.28	0.25	0.25	0.32	0.31	0.27	0.27
Sample name	2011-4VB								
Inclusion No. <sup>a</sup>		11-4 V-p1i1	11-4 V-p2i1	11-4 V-p3i1	11-4 V-p4i1	11-4 V-p5i1	11-4 V-p6i1	11-4 V-p7i1	
Host phenocryst <sup>b</sup>		ol	ol	cpx	cpx	cpx	opx	opx	
Host chemistry <sup>c</sup>		Fo75	Fo73	Wo44En40Fs16	Wo43En41Fs16	n.a	Wo2En69Fs29	Wo3En65Fs33	
Inclusion size (max, mm)		0.05	0.15	0.04	0.03	0.04	0.04	0.05	

**Table 3** (continued)

Sample name	2011-4VB								
Accompanying phase <sup>d</sup>	A bubble (0.05)								
Bubble (vol%) <sup>e</sup>	4								
Overgrowth (in weight) <sup>f</sup>									
SiO <sub>2</sub>	55.48	57.38	74.18	73.56	71.76	67.99	67.85		
TiO <sub>2</sub>	0.79	0.81	0.45	0.46	0.62	0.51	0.37		
Al <sub>2</sub> O <sub>3</sub>	18.88	16.98	11.79	11.63	13.09	14.79	13.85		
FeOt	7.69	8.65	2.73	2.84	3.19	4.11	4.73		
MnO	0.16	0.18	0.07	0.10	0.11	0.12	0.12		
MgO	3.19	3.40	0.85	0.78	1.09	1.62	1.32		
CaO	8.87	8.37	2.40	2.44	2.73	3.95	3.33		
Na <sub>2</sub> O	3.58	2.92	2.87	3.57	3.45	3.53	4.40		
K <sub>2</sub> O	1.35	1.31	4.67	4.61	3.97	3.38	4.03		
S	0.162	0.143	0.007	0.009	0.014	0.039	0.034		
Cl	0.067	0.071	0.131	0.129	0.115	0.125	0.141		
H <sub>2</sub> O <sup>g</sup>	2.4	2.1/2.2	4.8	4.7	3.4	3.8	3.3		
CO <sub>2</sub> <sup>g</sup>	0.036	0.027/0.267	0.031	0.016	0.016	0.019	0.028		
S(+6)/total S <sup>h</sup>	0.5	0.8	n.a	n.a	n.a	n.a	n.a		
log fO <sub>2</sub> <sup>i</sup>	-9	-9	-	-	-	-	-		
Fe(+2)/total Fe <sup>j</sup>	0.8	0.7	-	-	-	-	-		
FMQ (log unit) <sup>j</sup>	1.3	2.0	-	-	-	-	-		
Sat. Press. (MPa) <sup>k</sup>	141/127	106/-	199/186	167/153	110/-	129/-	120/126		
Temperature (°C) <sup>l</sup>	1015	1041	930	925	-	(963)	988		
Pressure (MPa) (host-liquid) <sup>l</sup>	-	-	600	450	-	-	-		
K <sub>D</sub> <sup>m</sup>	0.31	0.33	0.27	0.24	-	(0.42)	0.31		
Sample name	2018-1VGP								
Inclusion No. <sup>a</sup>	18-1 V-p1i1	18-1 V-p2i1	18-1 V-p3i1	18-1 V-p3i2	18-1 V-p4i1	18-1 V-p5i1	18-1 V-p6i1	18-1 V-p6i2	18-1 V-p7i1
Host phenocryst <sup>b</sup>	cpx	cpx	cpx	cpx	opx	opx	opx	opx	opx
Host chemistry <sup>c</sup>	Wo44En41Fs15	Wo43En40Fs17	Wo44En41Fs15	Wo43En41Fs16	Wo3En71Fs26	Wo3En74Fs23	Wo2En66Fs32	Wo2En62Fs35	Wo3En63Fs35
Inclusion size (max, mm)	0.05	0.05	0.03	0.03	0.05	0.04	0.03	0.02	0.02
Accompanying phase <sup>d</sup>	ap (0.005)					mt (0.005)			
Bubble (vol%) <sup>e</sup>									
Overgrowth (in weight) <sup>f</sup>									
SiO <sub>2</sub>	75.83	72.35	71.25	74.60	66.11	59.72	68.27	75.35	75.11
TiO <sub>2</sub>	0.29	0.72	0.49	0.32	0.78	0.82	0.78	0.23	0.39
Al <sub>2</sub> O <sub>3</sub>	11.68	11.83	13.58	11.67	14.44	16.92	14.61	11.79	11.28
FeOt	1.89	4.64	2.61	2.08	5.99	5.63	4.19	3.32	3.33
MnO	0.03	0.05	0.04	0.06	0.16	0.15	0.05	0.10	0.03
MgO	0.70	0.76	1.03	0.67	1.29	3.40	1.49	0.86	0.82
CaO	1.92	2.34	2.88	1.84	4.39	7.34	3.59	1.58	1.93
Na <sub>2</sub> O	2.94	3.52	3.70	3.66	3.67	4.32	3.34	3.25	2.73
K <sub>2</sub> O	4.73	3.80	4.41	5.10	3.17	1.70	3.68	3.52	4.39
S	0.005	0.003	0.009	0.005	0.009	0.138	0.020	0.008	0.010

**Table 3** (continued)

Sample name	2018-1VGP								
Cl	0.129	0.094	0.124	0.152	0.110	0.072	0.166	0.092	0.113
H <sub>2</sub> O <sup>g</sup>	3.5	0.5	2.2	3.2	1.2	5.0	2.3	3.1	2.7
CO <sub>2</sub> <sup>g</sup>	0.027	0.011	0.018	0.027	0.000	0.021	0.022	0.013	0.018
S(+6)/total S <sup>h</sup>	n.a.	n.a.	n.a.	n.a.	n.a.	0.7	n.a.	n.a.	n.a.
log fO <sub>2</sub> <sup>i</sup>	–	–	–	–	–	–10	–	–	–
Fe(+2)/total Fe <sup>l</sup>	–	–	–	–	–	0.8	–	–	–
FMQ (log unit) <sup>j</sup>	–	–	–	–	–	1.9	–	–	–
Sat. Press. (MPa) <sup>k</sup>	143/123	20/20	74/-	129/114	14/-	205/194	84/-	100/-	93/-
Temperature (°C) <sup>l</sup>	925	(960)	974	930	(1086)	(1031)	(993)	955	968
Pressure (MPa) (host-liquid) <sup>l</sup>	590	(480)	540	510	(240)	(470)	(230)	20	120
K <sub>D</sub> <sup>m</sup>	0.31	(0.15)	0.32	0.28	(0.17)	(0.43)	(0.39)	0.33	0.31

FeOt total FeO

<sup>a</sup> The abbreviations (TS, KP, 11-1P, 11-2SG, 11-4 V and 18-1 V) are defined in Table 1. Numbers with "p" and numbers with "i" of each sample indicate each phenocryst and each inclusion

<sup>b</sup> ol = olivine, cpx = clinopyroxene, opx = orthopyroxene, pl = plagioclase

<sup>c</sup> Chemical composition of host phenocrysts near the melt inclusions Fo = forsterite content (mol%) in the olivine. Wo En Fs = wollastonite, enstatite and ferrosite contents (mol%) in the pyroxene. An = anorthite content (mol%) in the plagioclase

<sup>d</sup> Accompanying phases in the melt inclusions. ap = apatite, mt = magnetite. Numbers in parentheses represent maximum sizes of the bubbles, apatite and magnetite (mm)

<sup>e</sup> Vol% of bubble in inclusion. See text

<sup>f</sup> Extent of the overgrowth in the olivine-hosted inclusions calculated from the chemical composition of the inclusions and their host olivines, assuming the temperature of the magma is 1030°C (Suzuki et al. 2013b). The chemical compositions of the olivine-hosted inclusions in this table were corrected for the overgrowth

<sup>g</sup> H<sub>2</sub>O and CO<sub>2</sub> contents of the inclusions were measured by SIMS. x/y: x is SIMS analysis, y is based on reconstruction of bulk inclusion composition by adding equilibrium gas (bubble) volume

<sup>h</sup> Mol fraction of S(+6) in total S in the inclusions calculated from the Ska radiation wavelength, assuming that all S in the inclusions is composed of S(+6) and S(-2). n.a., not analyzed

<sup>i</sup> Calculated from the mol fraction of S(+6) in total S in the inclusions by Wallace and Carmichael (1994). In these calculations, temperatures of 989°C was used for 1235 scoria, that was estimated from clinopyroxene-liquid thermobarometer applied to chemical composition of the melt of TS-p3i1 and its host phenocryst. Temperature of 948°C was used for 1716-1717 Gy pumices, based on the results of two pyroxene thermometry (Additional file 6). Temperatures for the olivine-hosted inclusions of the 2011 eruptions were assumed to 1030°C, that is temperature of mafic end member magma estimated by Suzuki et al. (2013b). Temperature of 942°C, that is the average temperature estimated from two pyroxene thermometry applied to 2018-1 and 2018-2 products, was used for 18-1 V-p5i1

<sup>j</sup> Calculated from the oxygen fugacity and chemical composition of the inclusions by Kilinc et al. (1983). Temperatures for these calculations were the same as the calculations of the oxygen fugacities

<sup>k</sup> x/y: x, Saturation pressures calculated from measured H<sub>2</sub>O and CO<sub>2</sub> contents of the melt inclusions using the silicate melt-H<sub>2</sub>O-CO<sub>2</sub> solution model by Newman and Lowenstern (2002). In these calculations, "basalt calculations" was used for olivine-hosted inclusions and "rhyolite calculations" was used for the other inclusions. y, the pressures calculated using the H<sub>2</sub>O-CO<sub>2</sub> mixed fluid saturation model of Ghiorso and Gualda (2015). An online app of the model, MagmaSat, made by Ghiorso and Gualda (2015) was used for these calculations. The mol ratio of Fe(+2) to total Fe in the melt was assumed to be 0.8. In the cases of low CO<sub>2</sub> contents, MagmaSat app was not available. Temperatures used in these calculations were the same as the calculations of the oxygen fugacities. Temperatures of pyroxene-hosted inclusions of the 2011 eruptions were assumed to 870°C, that is temperature of felsic end member magma estimated by Suzuki et al. (2013b)

<sup>l</sup> The temperatures of the magmas were estimated from the chemical compositions of the inclusions and their host olivines or plagioclases, using olivine-liquid and plagioclase-liquid thermometers (Putirka 2008). In addition, the temperatures and pressures of the magmas were estimated from the chemical compositions of the inclusions and their host clinopyroxenes or orthopyroxenes using clinopyroxene-liquid and orthopyroxene-liquid thermobarometers (Putirka 2008). Details of the geological thermometers and barometers are shown in Additional file 5

<sup>m</sup> K<sub>D</sub> of the melt inclusions in olivines, plagioclases, clinopyroxenes and orthopyroxenes. Details of the K<sub>D</sub> values are shown in Additional file 5. Values in parenthesis indicate that the calculated. K<sub>D</sub> values were not in the equilibrium range

silicic andesite end member (SiO<sub>2</sub> = 62–63 wt% and 43 vol% phenocryst content), as estimated by Suzuki et al. (2013b). The pumices, scoria, and lava from the 2018

eruptives contain no olivine phenocrysts, except for 2018-2VS with olivine phenocrysts of < 1 vol% (Additional file 2). The rare olivine phenocrysts in 2018-2VS

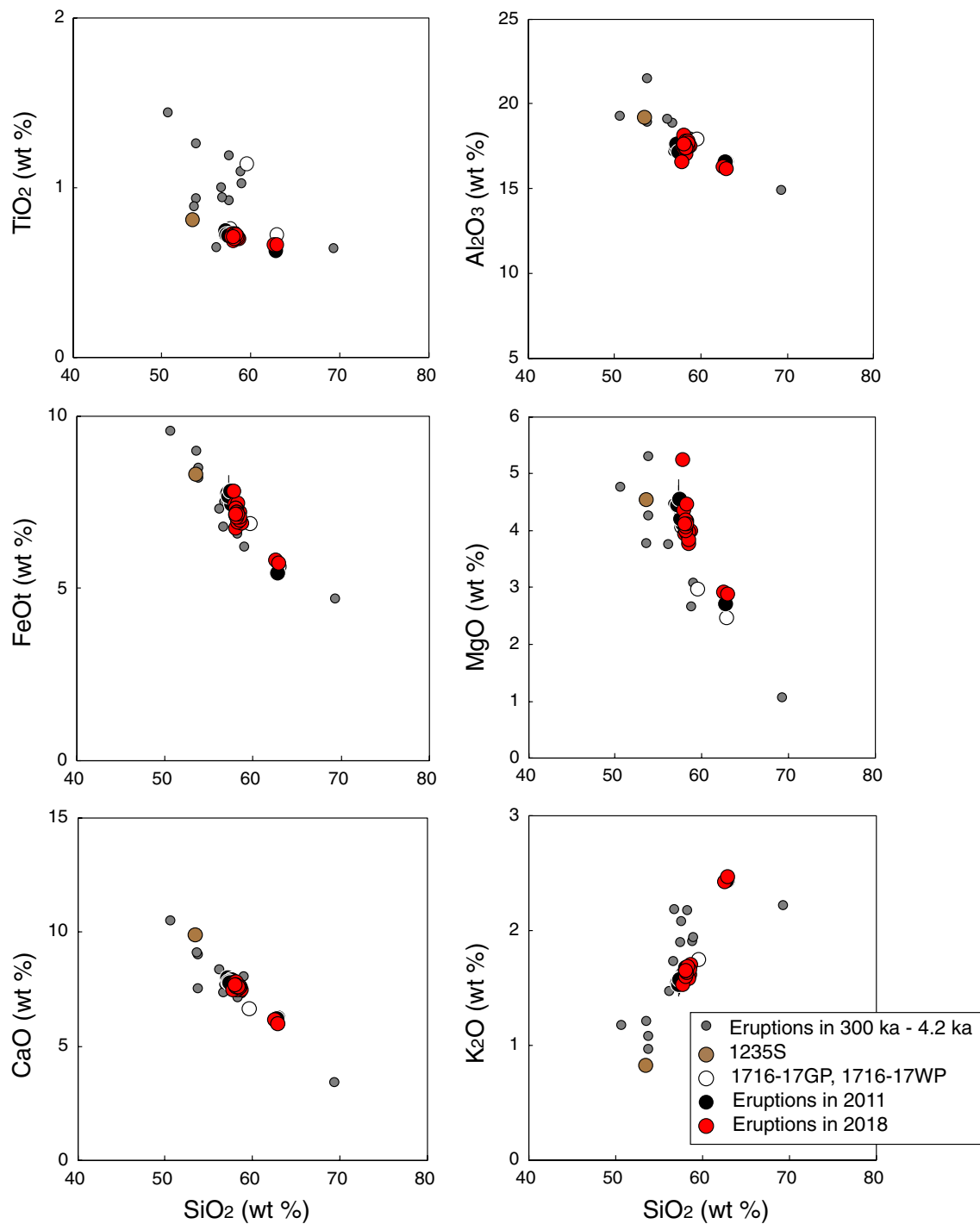


**Fig. 2** Whole-rock chemical compositions of products from the 1235, 1716–17, 2011, and 2018 eruptions (also shown in Table 2). Closed circles denoted “Eruptions in 2011” show the chemical compositions of 2011-2SGP, 2011-3SGP, 2011-4VB, 2011-5VL, and 2011-7VL. Red circles denoted “Eruptions in 2018” show the chemical compositions of 2018-1VGP, 2018-2VGP, 2018-2VS, 2018-3BB1 to BB3, and 2018-4L1 to L5. Open circles show the whole-rock compositions of 1716-17GP and 1716-17WP. Brown and small gray circles show the whole-rock compositions of 1235S and previous products of the younger Kirishima volcanoes (300 ka–4.2 ka), respectively. Error bars show standard deviations for each analysis (Tomiyama et al. 2013) shown in Table 2. Refer to Table 1 for sample names

have a reaction rim composed of orthopyroxene (Additional file 3 l). These observations suggest that olivine could not stabilize in the 2018 magma chamber.

#### Chemical compositions of minerals and groundmasses

The cores of the plagioclase phenocrysts (hereafter “plagioclase-phenocryst cores”) in the 2011 eruption products have variable composition ( $An_{42-94}$ ) with major  $An_{84-94}$  and  $An_{50-62}$  populations (Fig. 3a). The two populations indicate mixing of mafic magma with high-An plagioclases and felsic magma with low-An plagioclases. Significant variation was also observed in the rims of the plagioclase-phenocrysts (hereafter “plagioclase-phenocryst rims”) with two peaks at approximately  $An_{50-60}$  and  $An_{66-76}$  (Fig. 3b). In contrast, the plagioclase cores (<0.1 mm) in the groundmass (hereafter “groundmass-plagioclase cores”) have only one peak at approximately  $An_{60-74}$ , although they show a large variation in  $An_{40-90}$  (Fig. 3c). This suggests that most groundmass-plagioclases started to crystallize in a melt made by mixing. In comparison, the significant variation observed in the plagioclase-phenocryst rims suggests that the plagioclase phenocrysts did not regrow after mixing, implying that the eruption occurred soon after mixing. Similar variations are observed in the plagioclase-phenocryst cores ( $An_{44-91}$ ) and rims ( $An_{50-90}$ ), and in the groundmass-plagioclase cores ( $An_{57-88}$ ) of the 2018 products (Fig. 3a–c). This similarity indicates that the magmas that were erupted in 2011 and 2018 formed via mixing of the same end-member magmas.

Similar variations in chemical composition of the clinopyroxene-phenocryst cores are observed in the 2011 and 2018 products (Fig. 3g; Additional file 3). The orthopyroxene-phenocryst cores in the 2018 products show bimodal Mg# distribution, similar to those in the 2011 products (Fig. 3j; Additional file 3). These similarities in clinopyroxene and orthopyroxene cores indicate that the magmas that erupted in 2011 and 2018 were formed by mixing of the same end-member magmas. Although the orthopyroxene-phenocryst rims in the 2018 products have bimodal Mg# distribution in the same manner as the 2011 samples (Mg#64–68 and Mg#72–74; Fig. 3k), more high-Mg# (Mg#72–74) orthopyroxene-phenocryst rims formed as compared to 2011. This discrepancy suggests that the high-Mg# orthopyroxene-phenocryst rims from the 2018 samples were able to grow in the magma chamber over the period 2011–18. Detailed descriptions on clinopyroxenes and orthopyroxenes are shown in Additional file 3.

Of the 225 plagioclase phenocrysts from 2011, 10% (2011-1PP–2011-8A) have rims reaching >0.1 mm in length (Additional file 3), whereas 28% of the 85 plagioclase phenocrysts in the 2018 products have wide rims. The increase in the fraction of plagioclases with wide

rims suggests that the magma chamber was able to crystallize over this period. All clinopyroxene phenocrysts in the 2011 products observed in this study (100) have rims of <0.05 mm (Additional file 3). In contrast, 13% of the 68 clinopyroxene phenocrysts from 2018 have rims reaching >0.05 mm in length, and the maximum width of the clinopyroxene-phenocryst rims from the 2018 eruptions is 0.16 mm. The fraction of orthopyroxene phenocryst with rims >0.05 mm increased from 3% in 2011 (130) to 21% in 2018 (82). The maximum width of the orthopyroxene-phenocryst rims also increased from 0.07 mm in 2011 to 0.16 mm in 2018. The increases in the numbers of clinopyroxenes and orthopyroxenes with wide rims and the maximum width of the rims from 2011 to 2018 suggest that the magma chamber crystallized over time, as did the plagioclase-phenocryst rims.

The olivine phenocrysts in the 2011 products have core compositions of  $Fo_{74-80}$  (Fig. 3d). The olivine phenocrysts have rims that show normal zoning with widths <0.06 mm (Additional file 3), whereas olivine phenocrysts are rarely observed in the 2018 products (Additional file 2) and the phenocrysts that are present have large orthopyroxene rims (Additional file 3). No groundmass-olivines were found in the 2018 products. These observations indicate that the physical and chemical conditions during the formation of the 2018 magma were not stable enough for olivine formation.

The groundmasses of the eruption products from January 2011 (2011-1PP, 2011-2SGP, and 2011-3SGP) have andesite compositions: 61–62 wt%  $SiO_2$  and 2.1–2.2 wt%  $K_2O$  (normalized to volatile-free basis; Additional file 4; Fig. 4); however, 2011-2SWP has a rhyolitic composition (70.81 wt%  $SiO_2$  and 3.84 wt%  $K_2O$ ; Additional file 4; Fig. 4). The groundmasses of the products from February 2011 (2011-4VB and 2011-5VL) have slightly  $SiO_2$ - and  $K_2O$ -rich compositions (63–64 wt%  $SiO_2$  and 2.4 wt%  $K_2O$ ) compared to the subplinian gray pumices. The groundmasses in the eruption products from March–August 2011 (2011-6VA to 2011-9A) have richer  $SiO_2$  and  $K_2O$  compositions (62–65 wt%  $SiO_2$  and 2.0–2.8 wt%  $K_2O$ ), except 2011-8A (GG-type). The groundmass of 2011-8A (GG-type) has a highly evolved composition (68.42 wt%  $SiO_2$  and 3.50 wt%  $K_2O$ ), which is similar to that of 2011-2SWP. These results indicate that the melt in the magma chamber gradually transformed to a high- $SiO_2$  and - $K_2O$  composition between January–August 2011. The groundmasses of 2018-1VGP, 2018-1VS, 2018-2VGP, 2018-2VS, and 2018-4 L1 and L2 (dark-gray and lithic lava) have a dacite composition: 64–66 wt%  $SiO_2$  and 2.5–2.9 wt%  $K_2O$  (Additional file 4; Fig. 4). These compositions are similar to or a little evolved compared to the eruptive products from March–August 2011. This similarity suggests that the melt in the 2018 magma was

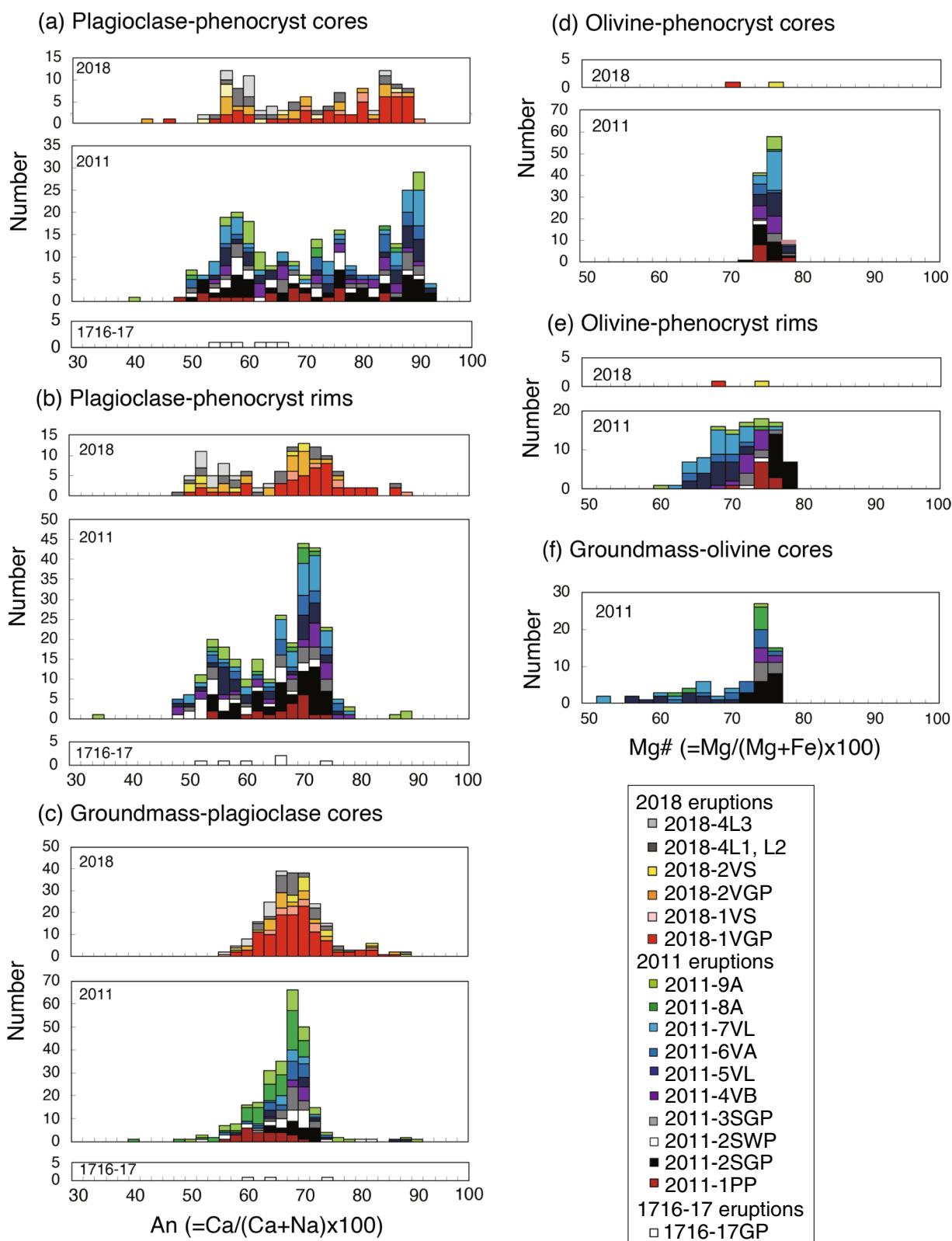


**Fig. 3** Chemical compositions of **a** plagioclase-phenocryst cores, **b** plagioclase-phenocryst rims, **c** groundmass-plagioclase cores, **d** olivine-phenocryst cores, **e** olivine-phenocryst rims, **f** groundmass-olivine cores, **g** clinopyroxene-phenocryst cores, **h** clinopyroxene-phenocryst rims, **i** groundmass-clinopyroxene cores, **j** orthopyroxene-phenocryst cores, **k** orthopyroxene-phenocryst rims, and **l** groundmass-orthopyroxene cores.  $An = Ca / (Ca + Na) \times 100\%$  in mol.  $Mg\# = Mg / (Mg + Fe) \times 100\%$  in mol. Refer to Table 1 for sample names

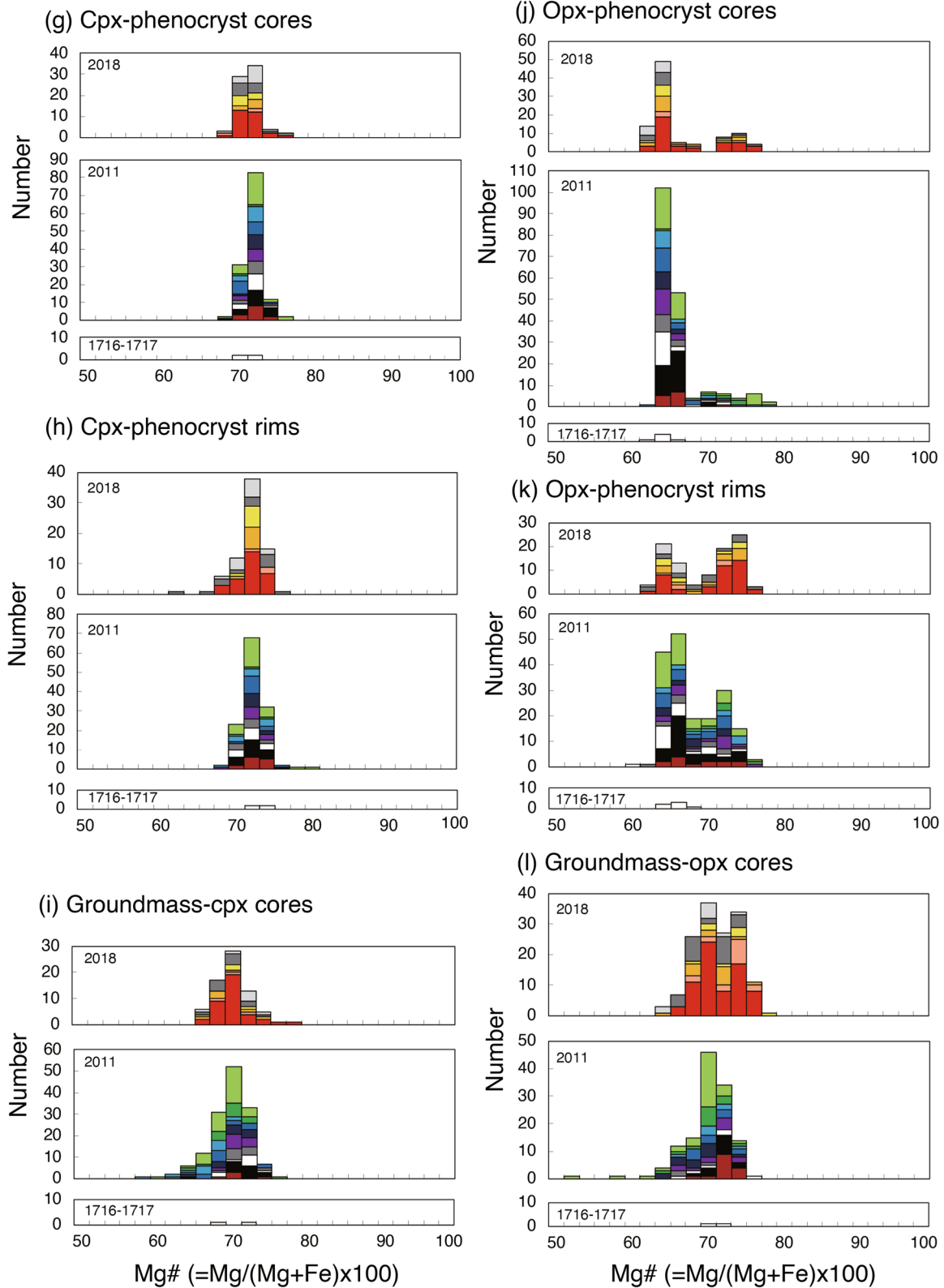


Fig. 3 continued



a remnant of the melt in the 2011 magma. In contrast, the groundmass of 2018-4L3 (gray and porous lava) has a rhyolite composition (74.83 wt% SiO<sub>2</sub> and 4.50 wt% K<sub>2</sub>O; Additional file 4; Fig. 4), which is the highest SiO<sub>2</sub> and K<sub>2</sub>O contents among the groundmasses observed in the 2011–18 products.

### Melt inclusions

Four melt inclusions from 1235S, 16 inclusions from 1716-17GP, 79 inclusions in the 2011 eruptive products (2011-1PP to 2011-7VL), and 24 inclusions from 2018-1VGP were analyzed in this study (Table 1; Table 3; Additional file 5). Chemical compositions of melt inclusions whose H<sub>2</sub>O and CO<sub>2</sub> contents were measured using SIMS are shown in Table 3. Chemical compositions of melt inclusions whose H<sub>2</sub>O content were measured using EPMA are shown in Additional file 5. Because the analytical error in H<sub>2</sub>O content measured using SIMS ( $\pm 0.2$  wt%; see Analytical methods section) is smaller than that by EPMA ( $\pm 1$  wt%; Additional file 5), H<sub>2</sub>O contents of melt inclusions shown in Table 3 was used for following discussion. Most inclusions are glassy, but several contain minerals and bubbles, and are found in the olivine, clinopyroxene, orthopyroxene, plagioclase, and ilmenite phenocrysts (Table 3; Additional file 5). Most inclusions are elliptical or quadrilateral in shape and range from 0.01 to 0.15 mm in diameter (Fig. 5). BSE images of the melt inclusions in the olivines show overgrowth of 1–2  $\mu$ m. The chemical compositions of these inclusions were corrected for post-entrapment crystallization by adding the host-olivine component until an olivine-melt equilibrium was reached, assuming that  $K_D (= (X_{FeO}^{Ol}/X_{FeO}^{Liq}) / (X_{MgO}^{Ol}/X_{MgO}^{Liq}))$ , distribution coefficient relating the partitioning of iron and magnesium between olivine and liquid) = 0.30 (Roeder and Emslie 1970; Saito et al. 2010). Olivine overgrowth of 0–5.3 wt% was estimated via this method (Table 3; Additional file 5).

One inclusion found in an olivine from 1235S has andesite composition (59.44 wt% SiO<sub>2</sub> and 1.31 wt% K<sub>2</sub>O), whereas three inclusions in the clinopyroxenes from 1235S have dacite composition (63–68 wt% SiO<sub>2</sub> and 1–2 wt% K<sub>2</sub>O) (Table 3; Fig. 6). Sixteen inclusions in 1716-17GP have dacite-to-rhyolite compositions (62–76 wt% SiO<sub>2</sub> and 2–5 wt% K<sub>2</sub>O; Table 3; Fig. 6; Additional file 5). Inclusions from the 2011 eruptions can be divided into two types: andesite inclusions in olivine phenocrysts

(34 inclusions) with 52–62 wt% SiO<sub>2</sub> and 0.9–3 wt% K<sub>2</sub>O, and dacite–rhyolite inclusions in the plagioclase, clinopyroxene, and orthopyroxene phenocrysts (8 inclusions with 72–76 wt% SiO<sub>2</sub> and 4–5 wt% K<sub>2</sub>O in the plagioclase phenocrysts, 18 inclusions with 68–76 wt% SiO<sub>2</sub> and 3–7 wt% K<sub>2</sub>O in the clinopyroxene phenocrysts, and 17 inclusions with 68–78 wt% SiO<sub>2</sub> and 3–5 wt% K<sub>2</sub>O in the orthopyroxene phenocrysts). The inclusions from the 2018 eruptions have andesite-to-rhyolite compositions; 6 inclusions in the plagioclase phenocrysts have 71–73 wt% SiO<sub>2</sub> and 4 wt% K<sub>2</sub>O, 6 inclusions in the clinopyroxene phenocrysts have 61–76 wt% SiO<sub>2</sub> and 3–5 wt% K<sub>2</sub>O, and 12 inclusions in the orthopyroxene phenocrysts have 60–75 wt% SiO<sub>2</sub> and 2–4 wt% K<sub>2</sub>O. The chemical composition of the andesite and rhyolite inclusions did not differ greatly (Fig. 6). Less-evolved chemical compositions of <60 wt% SiO<sub>2</sub> and <2 wt% K<sub>2</sub>O in the 2011 samples were not observed in the inclusions from 2018, which have intermediate compositions rather than the andesite and dacite–rhyolite inclusions observed in the 2011 eruptives.

Significant variation is observed in the H<sub>2</sub>O and CO<sub>2</sub> contents of the andesite inclusions within the olivine phenocrysts, which range from 2.1 to 7.0 wt% for H<sub>2</sub>O (by SIMS) and from 0.001 to 0.054 wt% for CO<sub>2</sub> (Fig. 8; Table 3). Although the andesite inclusions also have a large range of S content (0.019 to 0.170 wt%; Fig. 8; Table 3; Additional file 5), they are divided to two group; 28 inclusions of 2011-1PP, 2011-2SGP, and 2011-4VB with high S content (0.120–0.170 wt%); and 4 inclusions of 2011-4VB and 2011-5VL with low S content (0.019–0.060 wt%). These large variations in H<sub>2</sub>O and CO<sub>2</sub> contents are not correlated with the SiO<sub>2</sub> and K<sub>2</sub>O contents of the inclusions (Fig. 7), indicating that the differences were not the result of fractional crystallization. Furthermore, inclusions with high H<sub>2</sub>O content (>4 wt%) have high S content (0.148–0.170 wt%; Fig. 8; Table 3). These results indicate that the observed variation may have been caused by the exsolution of H<sub>2</sub>O and S from the andesite melt. Contrarily, variation in the Cl content of the inclusions (0.053–0.092 wt%) is relatively small, except for 2 inclusions in 11-4 V-p8i1 and 11-1P-p1i1 that have high Cl contents (0.165 and 0.121 wt%, respectively; Table 3; Additional file 5). These high-Cl content inclusions are accompanied by high SiO<sub>2</sub> and K<sub>2</sub>O contents (61.80 wt% SiO<sub>2</sub>, 2.91 wt% K<sub>2</sub>O; and 61.16 wt%

(See figure on next page.)

**Fig. 4** Chemical compositions of groundmass in products from the 1716–17, 2011 and 2018 eruptions. **a** TiO<sub>2</sub> vs. SiO<sub>2</sub> contents; **b** Al<sub>2</sub>O<sub>3</sub> vs. SiO<sub>2</sub> contents; **c** FeO vs. SiO<sub>2</sub> contents; **d** MgO vs. SiO<sub>2</sub> contents; **e** CaO vs. SiO<sub>2</sub> contents; and **f** K<sub>2</sub>O vs. SiO<sub>2</sub> contents. Large circles and error bars show the groundmass compositions of products and their standard deviations, respectively (also shown in Additional file 4). Chemical compositions of melts at pressures of 50–200 MPa calculated with the MELTS program (Gualda et al. 2012; Additional file 9) are also shown. Whole-rock chemical compositions of the products from the 1235, 1716–17, 2011 and 2018 eruptions are also shown using the same symbols in Fig. 2. The small gray circles show whole-rock compositions for products from the younger Kirishima volcanoes (300 ka–4.2 ka)

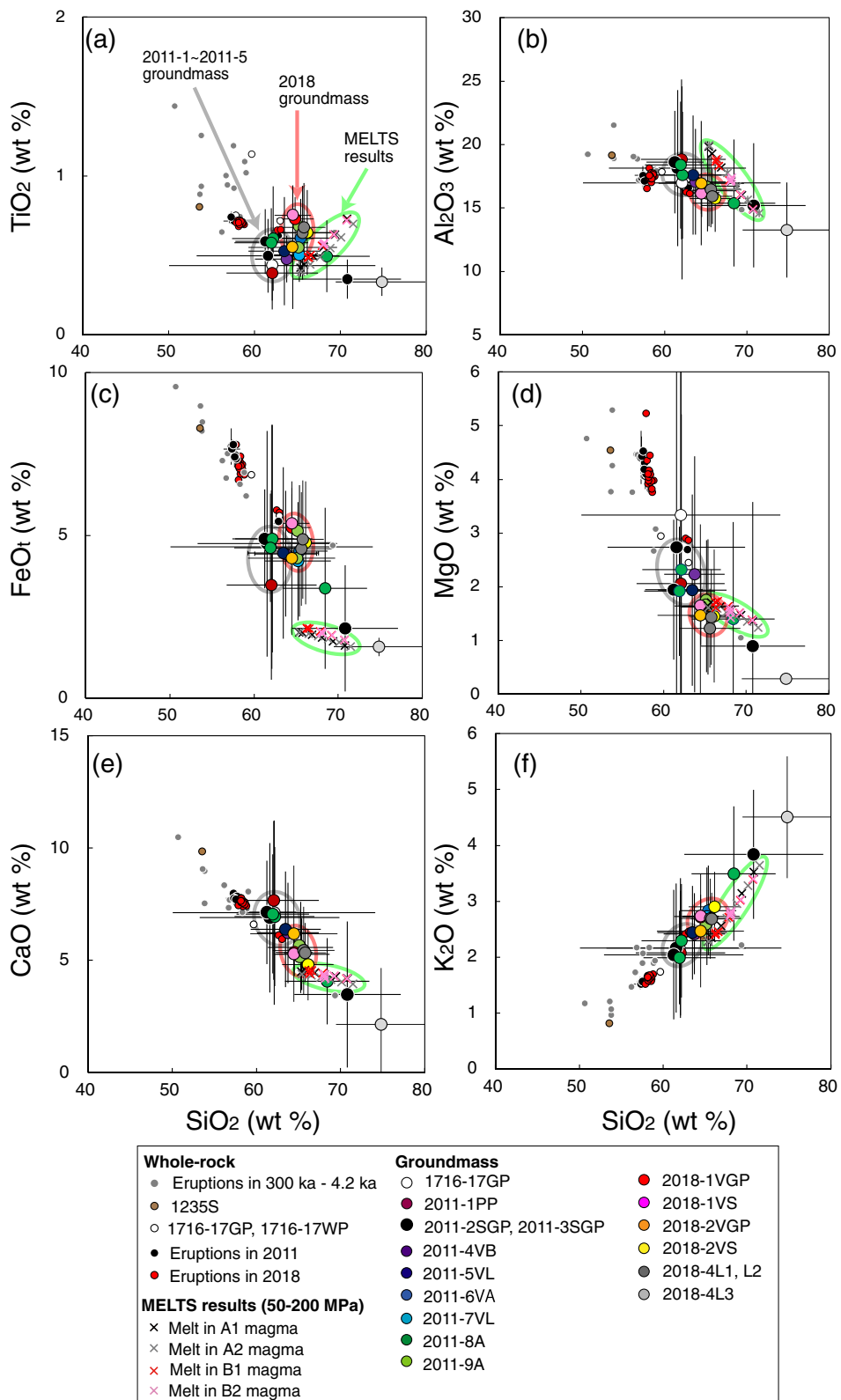
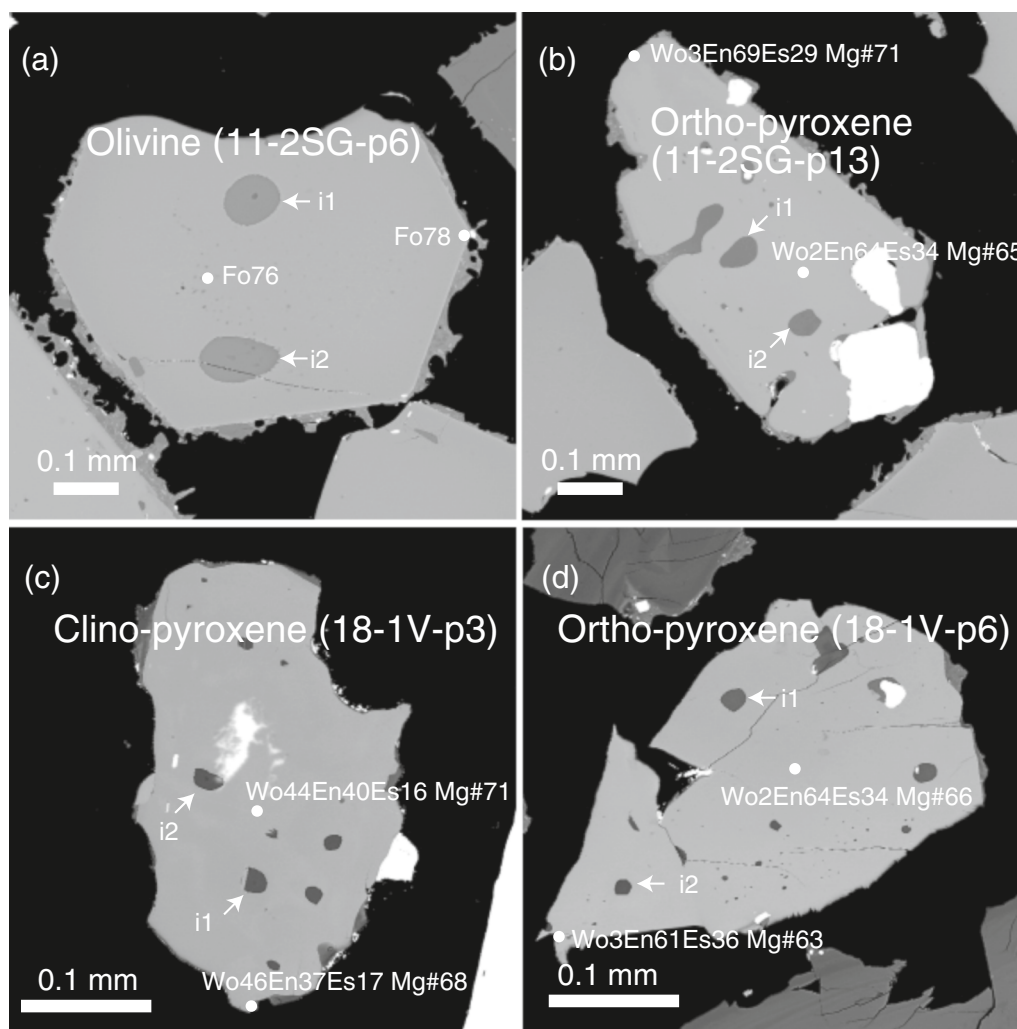


Fig. 4 (See legend on previous page.)



**Fig. 5** BSE images of melt inclusions (arrows) in **a** olivine phenocryst in 2011-2SGP (11-2SG-p6-i1 and 11-2SG-p6-i2); **b** orthopyroxene phenocryst in 2011-2SGP (11-2SG-p13-i1 and 11-2SG-p13-i2); **c** clinopyroxene phenocryst in 2018-1VGP (18-1 V-p3-i1 and 18-1 V-p3-i2); and **d** orthopyroxene phenocryst in 2018-1VGP (18-1 V-p6-i1 and 18-1 V-p6-i2). Chemical compositions of cores and rims in the host phenocrysts are also shown

SiO<sub>2</sub>, 2.84 wt% K<sub>2</sub>O, respectively), suggesting that this increase in the Cl content was due to crystallization.

Large variation is also observed in the H<sub>2</sub>O (1.4–4.8 wt%; by SIMS), CO<sub>2</sub> (0.002–0.048 wt%), and Cl (0.040–0.166 wt%) contents of the dacite–rhyolite inclusions from the 2011 eruptions (Fig. 8; Table 3; Additional

file 5). These large variations are uncorrelated with the SiO<sub>2</sub> and K<sub>2</sub>O contents in the same inclusions, indicating that the differences were not caused by fractional crystallization but were rather the result of degassing in the dacite–rhyolite melt. Most of the inclusions have S contents of <0.02 wt%, although four of the samples: 11-1P-p7i1,

(See figure on next page.)

**Fig. 6** Chemical compositions of melt inclusions in products from the 1235, 1716–17, 2011 and 2018 eruptions. **a** Al<sub>2</sub>O<sub>3</sub> vs. SiO<sub>2</sub> contents; **b** MgO vs. SiO<sub>2</sub> contents; **c** CaO vs. SiO<sub>2</sub> contents; and **d** K<sub>2</sub>O vs. SiO<sub>2</sub> contents. Large circles with error bars indicate chemical compositions of the groundmasses and the standard deviations, respectively (also shown in Fig. 4). Chemical compositions of groundmasses from the 2011 eruptions (2011-1PP, 2011-2SGP, 2011-2SWP, 2011-3SGP, 2011-4VB, 2011-5VL, 2011-6VA, 2011-7VL, 2011-8A, and 2011-9A) are denoted by gray circles. Chemical compositions of groundmasses from the 2018 eruptions (2018-1VGP, 2018-1VS, 2018-2VGP, 2018-2VS, and 2018-4L1 to L3) are represented by light red circles. Chemical composition of groundmasses in the form of gray pumices from 1716–17 are open circles. Whole-rock chemical compositions of products from the 2011 and 2018 eruptions and previous eruptions are also shown using the same symbols as in Fig. 4. Chemical compositions of melts (M1 and M2 magmas at pressure ranges of 50–500 MPa and F1, F2, A1, A2, B1, and B2 magmas at pressure ranges of 50–200 MPa) calculated using the MELTS program (Additional file 9) are also shown

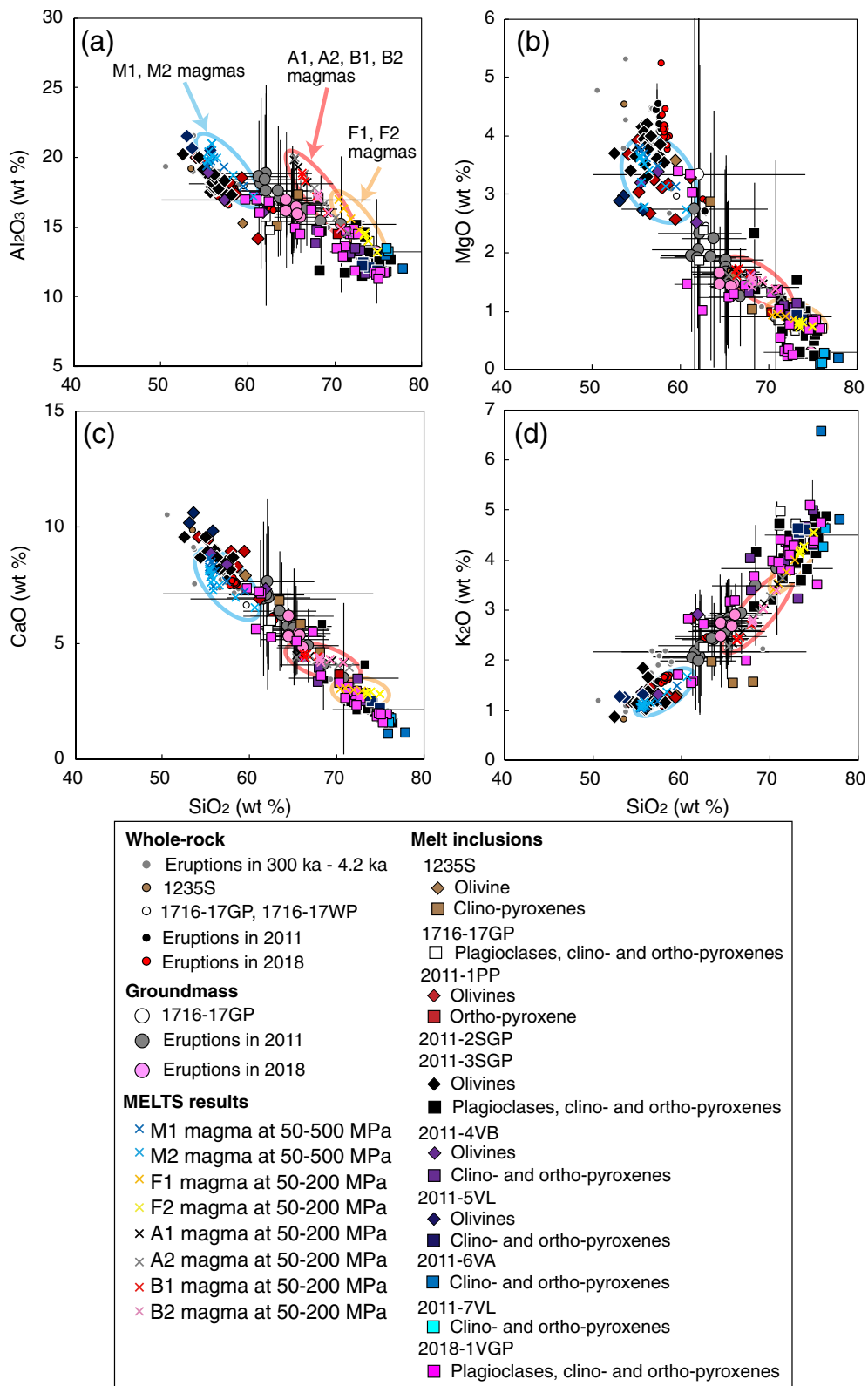
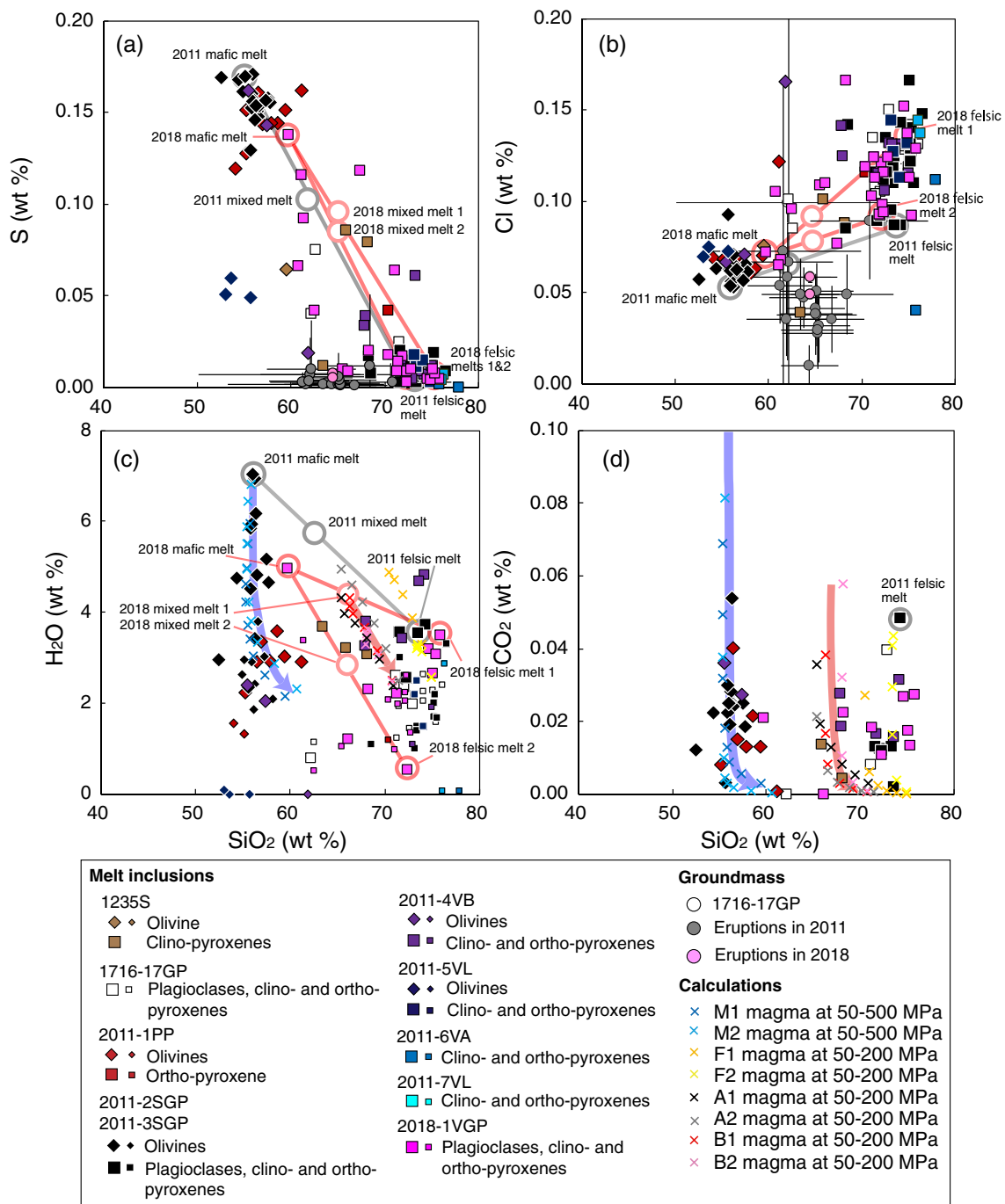


Fig. 6 (See legend on previous page.)



**Fig. 7** Volatile and SiO<sub>2</sub> contents in melt inclusions and groundmasses: **a** Sulfur vs. SiO<sub>2</sub> contents; **b** Cl vs. SiO<sub>2</sub> contents; **c** H<sub>2</sub>O vs. SiO<sub>2</sub> contents; and **d** CO<sub>2</sub> vs. SiO<sub>2</sub> contents. H<sub>2</sub>O and CO<sub>2</sub> contents of the melt inclusions were measured by SIMS and the S and Cl contents by EPMA, except for the small symbols in **c**, which indicate that the H<sub>2</sub>O content was measured by EPMA (shown in Additional file 5). Analytical errors for H<sub>2</sub>O and CO<sub>2</sub> by SIMS are ±0.2 wt% and ±0.0028 wt%, respectively (Saito et al. 2010). Analytical errors for H<sub>2</sub>O, S, and Cl by EPMA are ±1 wt%, ±0.007 wt%, and ±0.004 wt%, respectively (Saito et al. 2018). H<sub>2</sub>O, CO<sub>2</sub>, and SiO<sub>2</sub> contents of melts (M1 and M2 magmas at pressure ranges of 50–500 MPa and F1, F2, A1, A2, B1, and B2 magmas at pressure ranges of 50–200 MPa) calculated using the MELTS program (Additional file 9) are also shown. Gray lines with circles indicate mixing of mafic and felsic melts in the 2011 magma (Table 4). Red lines with circles indicate mixing of mafic and felsic melts in the 2018 magma (Table 4). Blue and red curves with arrows show the compositional changes in melts that are expected from a decrease in the pressures of the 2011 mafic magma and 2018 magma, respectively

11-4 V-p6i1, 11-4 V-p7i1, and 11-4 V-p12i1 have inclusion S contents of 0.034–0.061 wt%. These inclusions with relatively high S and low SiO<sub>2</sub> contents (67.85–70.35 wt%; Table 3; Additional file 5) suggest that the high S contents resulted from the mixing of high S content mafic melt with rhyolite melt.

The andesite–rhyolite inclusions in the 2018 eruptions also show large variations in terms of H<sub>2</sub>O (0.5–5.0 wt%; by SIMS), S (0.003–0.138 wt%), and Cl contents (0.065–0.166 wt%) (Fig. 7; Table 3; Additional file 5). The CO<sub>2</sub> contents in these inclusions are <0.027 wt%. The maximum H<sub>2</sub>O, CO<sub>2</sub>, and S contents in the andesite inclusions from the 2018 eruptions (5.0 wt% H<sub>2</sub>O, 0.021 wt% CO<sub>2</sub>, and 0.138 wt% S) are lower than those in the andesite inclusions from the 2011 eruptions (7.0 wt% H<sub>2</sub>O, 0.054 wt% CO<sub>2</sub>, and 0.0170 wt% S) (Fig. 7; Table 3; Additional file 5), suggesting that the andesite melt in the 2018 magma was volatile-poor compared to the 2011 magma. The large variations in the H<sub>2</sub>O, S, and Cl contents of the andesite–rhyolite inclusions from 2018 roughly correlate with the SiO<sub>2</sub> contents of the inclusions; those with lower SiO<sub>2</sub> content have higher H<sub>2</sub>O and S contents and lower Cl contents (Fig. 7). The results indicate that these variations were likely caused when mafic melt with high H<sub>2</sub>O and S and low Cl contents mixed with felsic melt of low H<sub>2</sub>O and S and high Cl contents.

Of the 123 melt inclusions analyzed in this study, 13% (16 inclusions) contain a bubble with a diameter of <0.0001–0.05 mm (Table 3; Additional file 5). The approximate bubble-to-inclusion ratio of the volume was estimated from the maximum sizes of the bubble and the inclusion, by assuming a spherical shape for the bubble and inclusion (Table 3; Additional file 5). The estimated ratios of the inclusions are <4 vol%, except for 11-5 V-p11i2 with the ratio of 20 vol% (Additional file 5). Small bubbles of less than a few vol% were probably formed by shrinkage of the melt during cooling (Anderson et al. 1989). Therefore, the small bubbles observed in this study were probably caused by the melt shrinkage after the inclusion entrapment. The H<sub>2</sub>O and CO<sub>2</sub> contents of 11 inclusions with small bubbles were estimated

by assessing the amount of H<sub>2</sub>O and CO<sub>2</sub> in the bubbles using the method described by Anderson et al. (1989; Table 3; Saito et al. 2001), with an assumption of gas-equilibrium between the melt and bubbles in these inclusions. The corrected H<sub>2</sub>O contents are almost equal to the measured values, indicating the effect of shrinkage bubbles is negligible. However, the corrected CO<sub>2</sub> contents are up to 12 times greater than the measured values. Because the presence of gas-equilibrium between the melt and bubbles in these inclusions is unknown, the corrected values might give maximum estimate, whereas the measured values without correction of shrinkage might give minimum estimate. Furthermore, the 20 vol% of 11-5 V-p11i2 is too large to have been formed by the melt shrinkage. This bubble may have derived from either leakage before quenching or entrapment of the bubble with the melt. The former case seems to be less likely because of the following two reasons: (1) optical observation did not indicate any leakage fractures, and (2) if there had been any inclusion leakage, the volatile content of the glass would have decreased. But S content of 11-5 V-p11i2 (0.060 wt%; Additional file 5) is similar or a little higher than those of two olivine-hosted inclusions (0.049 and 0.051 wt%) in 2011-5VL, that contain no bubbles. Thus, it is likely that the large bubble in the inclusion is trapped bubble.

## Physical and chemical conditions of the magma from 2011–18

### Magma temperature

Two-pyroxene thermometry (Putirka 2008) was applied to the compositions of the borders of intergrown clinopyroxene and orthopyroxene phenocrysts from the 1716–17, 2011, and 2018 eruptions. A temperature of 948 °C was recorded for the intergrown phenocrysts from the 1716–17 eruptions, and the intergrown phenocrysts from all the eruptions in 2011 (2011-1PP to 2011-9A) yielded similar temperatures (908–945 °C; Additional file 6), except 2011-8A, for which the intergrown phenocryst yielded a higher temperature estimate (1055 ± 10 °C). With a dacite whole-rock composition (Table 2), 2011-2SWP had the lowest

(See figure on next page.)

**Fig. 8** Volatile content of melt inclusions and groundmasses: **a** H<sub>2</sub>O - versus CO<sub>2</sub> contents, **b** S - versus CO<sub>2</sub> contents, **c** H<sub>2</sub>O - versus S contents, and **d** Cl - versus S contents. Error bars indicate analytical errors for H<sub>2</sub>O and CO<sub>2</sub> by SIMS and S and Cl by EPMA. The analytical errors in H<sub>2</sub>O by EPMA in **c** are ± 1 wt % (Saito et al. 2018). H<sub>2</sub>O and CO<sub>2</sub> contents in melts (M1 and M2 magmas at pressure ranges of 50–500 MPa and F1, F2, A1, A2, B1, and B2 magmas at pressure ranges of 50–200 MPa) calculated using the MELTS program (Additional file 9) are also shown. Solid and broken curves in (a) indicate solubilities of the H<sub>2</sub>O–CO<sub>2</sub> gas mixture in the 2011 mafic melt (Table 4) at 1030 °C and the 2011 felsic melt (Table 4) at 870 °C, respectively, calculated using the solubility model of Ghiorso and Gualda (2015). Gray lines with circles in **c** and **d** indicate mixing of mafic and felsic melts in the 2011 magma (Table 4). Red lines with circles in **c** and **d** indicate mixing of mafic and felsic melts in the 2018 magma (Table 4). Blue and red curves with arrows in **a** show expected compositional changes in the melts resulting from a decrease in the pressure of the 2011 mafic magma and 2018 magma, respectively. Yellow lines show CO<sub>2</sub>/H<sub>2</sub>O, CO<sub>2</sub>/S, S/H<sub>2</sub>O, and H<sub>2</sub>O/S ratios of the volcanic gases observed in 2011 (Shinohara 2013; Additional file 11). Green line in **b** shows CO<sub>2</sub>/S ratios of the volcanic gas observed in 2017 (GSJ/AIST 2017; Additional file 11). The same symbols are used as in Fig. 7

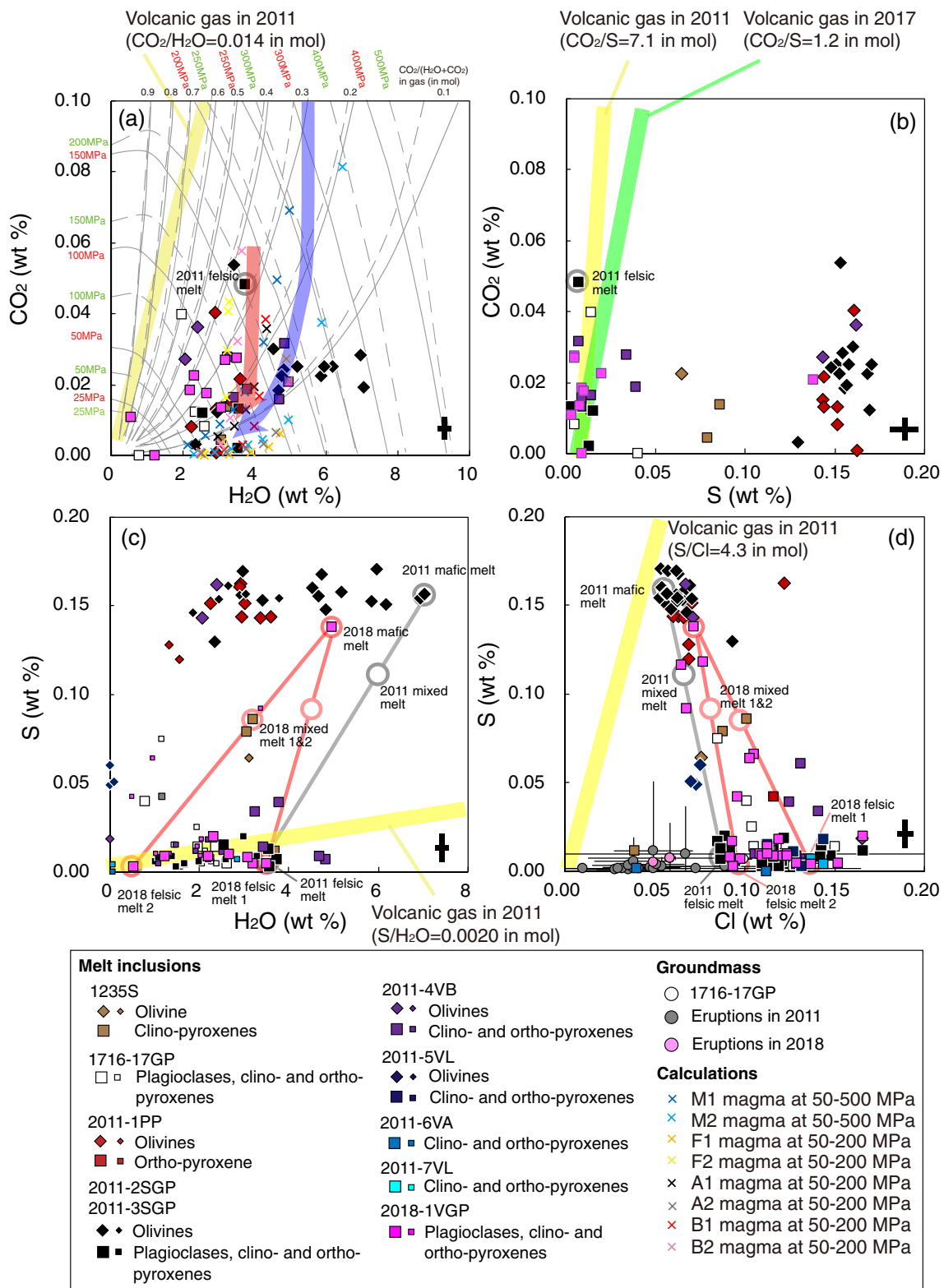


Fig. 8 (See legend on previous page.)

temperature of 908 °C among the 2011 eruptives. Two-pyroxene thermometry indicated that the temperature of the 2018 eruptives (914–944 °C) are similar to those of the 2011 eruptives. With a whole-rock dacite composition, 2018-4L3 showed the lowest temperature among the 2018 eruptives (914 °C), which is similar to that of 2011-2SWP (908 °C) with dacite composition.

Fe–Ti oxide thermometry (Anderson et al. 1993) was also applied to the border compositions of intergrown magnetite and ilmenite phenocrysts from the 1716–17, 2011, and 2018 eruptions (Additional files 6 and 7). The compositions of the intergrown phenocrysts in 1716-17GP yielded a temperature of 940 °C (Additional file 6) and an oxygen fugacity ( $\log f_{O_2}$ ) of -9.9 log units (2.0 log units above the FMQ buffer; Additional file 7), whereas the compositions of the intergrown phenocrysts from the 2011 eruptions (2011-3SGP to 2011-5VL) yielded temperatures of 928–977 °C (Additional file 6) and oxygen fugacity ( $\log f_{O_2}$ ) of -10.6 to -9.9 log units (1.2–1.7 log units above the FMQ buffer; Additional file 7). The temperature estimated for the 2011 magma by Fe–Ti oxide thermometry is similar to that obtained by two-pyroxene thermometry, except for the slightly higher temperature obtained for 2011-4VB (977 °C) by Fe–Ti oxide thermometry. In addition, the temperatures of 2018-1VGP, 2018-2VGP, 2018-2VS, 2018-4L1, and 2018-4L2 (940–985 °C) estimated by Fe–Ti oxide thermometry are similar to those obtained by two-pyroxene thermometry (914–944 °C). The oxygen fugacity of these eruptives (-10.5–9.9 log units and 1.2–1.7 log units above the FMQ buffer) are identical to those of the 2011 eruptives (-10.6–9.9 log units). Among all the 2018 products, the lowest temperature (873 °C) and oxygen fugacity (-11.2 log units) was shown by 2018-4L3.

The results of two-pyroxene thermometry and Fe–Ti oxide thermometry indicate that the temperature and oxidation state of the magma chamber did not change from 1716–17 to 2018. The lowest temperature (873 °C), which was obtained for 2018-4L3 with a dacite chemical composition (Table 2), is comparable to the temperature estimated for the felsic magma end member (870 °C for a silicic andesite magma with 62–63 wt% SiO<sub>2</sub>) by Suzuki et al. (2013b). Therefore, 2018-4L3 was derived from the low-temperature silicic part of the magma chamber. With a dacite chemical composition (Table 2), 2011-2SWP shows a relatively low temperature (908 °C), suggesting that it originated in the low-temperature silicic part of the magma chamber and was heated by high-temperature magma before the eruption.

Thereafter, the olivine-liquid thermometer (Putirka 2008) was applied to the chemical compositions of the melt and host phenocrysts of 22 olivine-hosted melt inclusions from the 2011 products to estimate

the temperature of the mafic end member magma that included olivine phenocrysts (Table 3; Additional file 5). Temperatures of 940–1041 °C (average  $990 \pm 25$  °C) were estimated, which is similar or slightly lower than that for basaltic andesite magma estimated by Suzuki et al. (2013b). We also applied plagioclase-liquid thermometers (Putirka 2008) to the chemical compositions of the melt and host phenocrysts of 10 plagioclase-hosted melt inclusions, clinopyroxene-liquid thermobarometers (Putirka 2008) to the chemical compositions of the melt and host phenocrysts of 20 clinopyroxene-hosted melt inclusions, and orthopyroxene-liquid thermobarometers (Putirka 2008) to the chemical compositions of the melt and host phenocrysts of 14 orthopyroxene-hosted melt inclusions (Table 3; Additional file 5). The temperature estimates for the plagioclase-, clinopyroxene-, and orthopyroxene-hosted melt inclusions in the 2011 products ( $938 \pm 23$ ,  $951 \pm 18$ , and  $978 \pm 36$  °C, respectively) are similar to those obtained by the two-pyroxene (912–945 °C for 2011-1PP, 2011-2SGP, 2011-3SGP, 2011-4VB, 2011-5VL, 2011-6VA, 2011-7VL and 2011-9A) and Fe–Ti oxide thermometry (928–977 °C for 2011-3SGP, 2011-4VB and 2011-5VL). In addition, the temperature estimates for the plagioclase-, clinopyroxene-, and orthopyroxene-hosted melt inclusions in the 2018 products ( $973 \pm 15$ ,  $955 \pm 33$ , and  $979 \pm 29$  °C, respectively) are similar to those obtained by two-pyroxene (936–944 °C) and Fe–Ti oxide thermometry (940–985 °C), except for 2018-4L3.

#### Magma pressure

The large variability observed in the H<sub>2</sub>O and CO<sub>2</sub> contents of the andesite inclusions in the olivine phenocrysts and dacite–rhyolite inclusions in the clinopyroxene- and orthopyroxene-phenocrysts from 2011 (Fig. 8) is not related to the SiO<sub>2</sub> content (Fig. 7), suggesting that magma degassing occurred with a decrease in the pressure. Gas saturation pressures were calculated from the H<sub>2</sub>O and CO<sub>2</sub> content of the inclusions by using the melt–H<sub>2</sub>O–CO<sub>2</sub> solubility models proposed by Newman and Lowenstern (2002) and Ghiorso and Gualda (2015). Gas saturation pressures of 62–486 MPa (average  $232 \pm 132$  MPa,  $n=22$ ) were obtained for the andesite inclusions in the olivine phenocrysts via the solubility model of Newman and Lowenstern (2002). The pressure range corresponds to a depth of 2–19 km under a lithostatic pressure gradient, assuming a crustal density of 2500 kg m<sup>-3</sup>. Gas saturation pressures of 127–225 MPa (average  $182 \pm 36$  MPa,  $n=9$ ) were calculated using the solubility model of Ghiorso and Gualda (2015), which is within the range estimated using the solubility model of Newman and Lowenstern (2002). The pressure range corresponds to a depth of 5–9 km under a lithostatic



pressure gradient. These results indicate that mafic magma ascended from a depth of at least 9 km to 2 km as the olivine crystallization occurred.

Large variability was also observed in the H<sub>2</sub>O and CO<sub>2</sub> contents of the dacite–rhyolite inclusions in the clinopyroxene- and orthopyroxene-phenocrysts from the 2011 products, which is not related to the SiO<sub>2</sub> content (Fig. 7), suggesting that magma degassing simultaneously occurred with a decrease in pressure. Gas saturation pressures were calculated using the H<sub>2</sub>O and CO<sub>2</sub> content obtained for the inclusions by the two melt–H<sub>2</sub>O–CO<sub>2</sub> solubility models. Gas saturation pressures of 36–199 MPa (average 120 ± 50 MPa, n=10) were obtained via the solubility model of Newman and Lowenstern (2002). The average pressure (120 MPa) corresponds to a depth of 5 km under a lithostatic pressure gradient. Gas saturation pressures of 126–186 MPa (average 152 ± 25 MPa, n=5) were calculated using the solubility model by Ghiorso and Gualda (2015), which is within the range obtained in the above estimates. These results indicate the presence of a felsic magma at a pressure of 120–152 MPa (corresponding to a depth of 5–6 km). The average gas saturation pressures obtained by the two solubility models (120 ± 50 and 152 ± 25 MPa) are in good agreement with the pressure estimated for silicic andesite magma (125 MPa) by Suzuki et al. (2013b).

Gas saturation pressures were similarly calculated using the H<sub>2</sub>O and CO<sub>2</sub> content of the andesite–rhyolite inclusions in the 2018 products and the above two melt–H<sub>2</sub>O–CO<sub>2</sub> solubility models. Gas saturation pressures of 74–205 MPa (average 118 ± 45 MPa, n=7) were obtained using the solubility model by Newman and Lowenstern (2002), except for the extremely low gas saturation pressures observed in 18-1 V-p2i1 and 18-1Vp4i1. The pressure range corresponds to a depth of 3–8 km under a lithostatic pressure gradient. The gas saturation pressures for the inclusions calculated using the solubility model by Ghiorso and Gualda (2015), were generally in the range 114–194 MPa (except for 18-1 V-p2i1), with an average of 144 ± 44 MPa, n=3, which is within the range of the above estimates. These estimates indicate that the 2018 magma was at depths of 3–8 km as the pyroxenes crystallized within the magma. The maximum estimate (8 km) is also similar to the source depth of the crustal deformation from July 2017 to March 2018 reported by JMA (2019b). The average gas saturation pressures estimated by the two solubility models (118 ± 45 and 144 ± 44 MPa) are the same as those estimated from the dacite–rhyolite inclusions in the 2011 products (120 ± 50 and 152 ± 25 MPa), indicating that the felsic magma was located at the same depth in 2011–18.

Gas saturation pressures were also calculated using the H<sub>2</sub>O and CO<sub>2</sub> content of the dacite–rhyolite inclusions in

1716-17GP and the andesite–dacite inclusions in 1235S using the two melt–H<sub>2</sub>O–CO<sub>2</sub> solubility models. Gas saturation pressures of 71–106 MPa (average 83 ± 20 MPa, n=3) were obtained for the dacite–rhyolite inclusions in 1716-17GP using the solubility model by Newman and Lowenstern (2002), whereas a pressure of 95 MPa was calculated for one plagioclase-hosted inclusion using the solubility model of Ghiorso and Gualda (2015). Extremely low gas saturation pressures were obtained for KP-p4i1. These results suggest that the 1716–17 magma was stored at a depth of 3–4 km. Gas saturation pressures of 89–156 MPa (average 119 ± 34 MPa, n=3) were obtained for the andesite–dacite inclusions in 1235S using the solubility model of Newman and Lowenstern (2002). The results suggest that the 1235S magma was stored at a depth of 4–6 km. Collectively, these results suggest that the magmas were generally stored at a depth of approximately 4 km before the eruptions.

#### Bulk volatile content of magma

Suzuki et al. (2013b) concluded that a mafic magma, a basaltic–andesite magma with a temperature of 1030 °C and 9 vol% phenocrysts of olivine and plagioclase, was mixed with a felsic magma, a silicic–andesitic magma with a temperature of 870 °C and 43 vol% phenocrysts of plagioclase, pyroxene, and Fe–Ti oxide before the 2011 eruptions. The andesite inclusions in the olivine phenocrysts were likely derived from the mafic magma, whereas the dacite–rhyolite inclusions in the pyroxene and plagioclase phenocrysts were sourced in the felsic magma. The H<sub>2</sub>O, S, and Cl contents of a melt in the 2011 mixed magma can be calculated from the volatile contents in the andesite and rhyolite inclusions, assuming that the melt was produced by the mixing of a melt from the mafic magma with that from the felsic magma (Table 4). The following assumptions were made: (1) inclusion 11-2SG-p9i1, with the highest H<sub>2</sub>O content of all the andesite inclusions from 2011-2SGP, can represent the mafic melt; (2) inclusion 11-2SG-p13i1, with the highest H<sub>2</sub>O content of all the rhyolite inclusions from 2011-2SGP, can represent the felsic melt; and (3) the mixed melt will have a SiO<sub>2</sub> content of 62 wt%, considering the SiO<sub>2</sub> content of groundmass of 2011-2SGP (Additional file 4). This calculation gave an H<sub>2</sub>O content of 5.9 wt%, an S content of 0.107 wt%, and a Cl content of 0.066 wt% for the 2011 mixed melt. Based on the content in a phenocryst from 2011-2SGP (28 vol%; Additional file 2), a bulk content of 4.0 wt% H<sub>2</sub>O, 0.072 wt% S, and 0.044 wt% Cl (A1 and A2 magmas in Table 4) was obtained. Both the andesite inclusions in the olivine phenocrysts and the dacite–rhyolite inclusions in the pyroxene and plagioclase phenocrysts of the 2011 products have lower CO<sub>2</sub>/H<sub>2</sub>O mass ratios than those of the volcanic

**Table 4** Calculation of bulk volatile contents in the 2011 and 2018 magmas. Details of the calculations are given in the text and the footnotes

2011 eruptions										
Assumptions			Results							
End member melts <sup>a</sup>			2011 mixed magma <sup>b</sup>				2011 mafic magma		2011 felsic magma	
2011 mafic melt	2011 felsic melt		2011 mixed melt of A1 magma	2011 mixed melt of A2 magma	Bulk volatile content of A1 magma	Bulk volatile content of A2 magma	Bulk volatile content of M1 magma	Bulk volatile content of M2 magma	Bulk volatile content of F1 magma	Bulk volatile content of F2 magma
SiO <sub>2</sub> (wt%)	56.07	74.23	62.00	62.00						
H <sub>2</sub> O (wt%)	7.0	3.7	5.9	5.9	4.0	4.0	6.2	6.2	3.7	1.9
CO <sub>2</sub> (wt%)	(1.5, 0.28)	0.048	1.00	0.21	0.70	0.14	1.4	0.25	0.048	0.025
S (wt%)	0.156	0.007	0.107	0.107	0.072	0.072	0.138	0.138	0.007	0.004
Cl (wt%)	0.056	0.087	0.066	0.066	0.044	0.044	0.050	0.050	0.087	0.045
2018 eruptions										
Assumptions			Results							
End member melts <sup>c</sup>			2018 magma <sup>d</sup>							
2018 mafic melt	2018 felsic melt 1	2018 felsic melt 2	2018 mixed melt 1		Bulk volatile content of B1 magma	2018 mixed melt 2	Bulk volatile content of B2 magma			
SiO <sub>2</sub> (wt%)	59.72	75.83	72.35	65.00		65.00				
H <sub>2</sub> O (wt%)	5.0	3.5	0.5	4.5	3.0	3.1	2.1			
CO <sub>2</sub> (wt%)	–	–	–	0.15	0.10	0.13	0.087			
S (wt%)	0.138	0.005	0.003	0.094	0.063	0.082	0.054			
Cl (wt%)	0.072	0.129	0.094	0.091	0.060	0.081	0.054			

<sup>a</sup> "2011 mafic melt" and "2011 felsic melt" indicate melts in a mafic and a felsic magma of the 2011 eruptions. The CO<sub>2</sub> contents of the 2011 mafic melts shown in parenthesis, 1.5 wt% of the melt of M1 magma and 0.28 wt% of the melt of M2 magma, were estimated as below

<sup>b</sup> The mixing mass ratio of the mafic and felsic melts in mixed magma (mafic:felsic = 0.67:0.33) was calculated from SiO<sub>2</sub> contents of the mafic, felsic and mixed melts. Water, S and Cl contents of the mixed melt were calculated from the mixing mass ratio and H<sub>2</sub>O, S and Cl contents of the mafic and felsic melts. Bulk CO<sub>2</sub> content of A1 magma was obtained from the bulk S content (0.072 wt%) and mass ratio of CO<sub>2</sub> and S in the volcanic gas (9.8). This mass ratio was calculated from mole ratio of SO<sub>2</sub> and H<sub>2</sub>S (SO<sub>2</sub>/H<sub>2</sub>S = 8) observed on 15 March 2011 and mole ratio of CO<sub>2</sub> and SO<sub>2</sub> (CO<sub>2</sub>/SO<sub>2</sub> = 8) observed on 18 May 2011 (Shinohara 2013; Additional file 11). Bulk CO<sub>2</sub> content of A2 magma was obtained from the bulk H<sub>2</sub>O content (4.0 wt%) and mass ratio of CO<sub>2</sub> and H<sub>2</sub>O in the volcanic gas (0.035), that was calculated from mole ratio of H<sub>2</sub>O and CO<sub>2</sub> (H<sub>2</sub>O/CO<sub>2</sub> = 70) of the volcanic gas (Shinohara 2013). The CO<sub>2</sub> contents of 2011 mixed melts were calculated to be 1.0 wt% for A1 magma and 0.21 wt% for A2 magma based on the bulk CO<sub>2</sub> contents and the phenocryst content in a case that the magmas had no gas phase

<sup>c</sup> "2018 mafic melt", "2018 felsic melt 1" and "2018 felsic melt 2" indicate melts in a mafic and a felsic magma of the 2018 eruptions

<sup>d</sup> The mixing mass ratio of 2018 mixed melt 1 (mafic:felsic = 0.67:0.33) was calculated from SiO<sub>2</sub> contents of the 2018 mafic melt, the 2018 felsic melt 1 and the mixed melt. Water, S and Cl contents of the mixed melt 1 were calculated from the mixing mass ratio and H<sub>2</sub>O, S and Cl contents of the mafic melt and the 2018 felsic melt 1. Bulk CO<sub>2</sub> content of B1 magma was obtained from the bulk S content (0.063 wt%) and mass ratio of CO<sub>2</sub> and S in the volcanic gas (1.6). This mass ratio was calculated from mole ratio of SO<sub>2</sub> and H<sub>2</sub>S (SO<sub>2</sub>/H<sub>2</sub>S = 2.7) and that of CO<sub>2</sub> and SO<sub>2</sub> (CO<sub>2</sub>/SO<sub>2</sub> = 1.6) observed on 12 October 2017 (GSJ/AIST 2017; Additional file 11). The mixing mass ratio of 2018 mixed melt 2 (mafic:felsic = 0.58:0.42) was calculated from SiO<sub>2</sub> contents of the 2018 mafic melt, the 2018 felsic melt 2 and the 2018 mixed melt 2. Water, S and Cl contents of the mixed melt 2 were calculated from the 2018 mixing mass ratio and H<sub>2</sub>O, S and Cl contents of the mafic melt and the felsic melt 2. Bulk CO<sub>2</sub> content of B2 magma was obtained from the bulk S content (0.054 wt%) and the mass ratio of CO<sub>2</sub> and S in the volcanic gas (1.6). The CO<sub>2</sub> contents of 2018 mixed melts were calculated to be 0.15 wt% for B1 magma and 0.13 wt% for B2 magma based on the bulk CO<sub>2</sub> contents and the phenocryst content

gas (Fig. 8). The disagreement in the CO<sub>2</sub>/H<sub>2</sub>O mass ratios of inclusions and volcanic gas is most likely due to the super-saturation of CO<sub>2</sub> at the time of inclusion

entrapment. This indicates that merely measuring the melt inclusions might lead to underestimation of the total volatile content in the magmas, especially for less-soluble

volatile species such as CO<sub>2</sub> (Papale 2005). Because the volcanic gas observed in 2011 was emitted from a mixed magma, the bulk CO<sub>2</sub> content of the magma was calculated from the bulk H<sub>2</sub>O and S contents and the mass CO<sub>2</sub>/S and CO<sub>2</sub>/H<sub>2</sub>O ratios of the volcanic gas (Table 4). A bulk CO<sub>2</sub> content of 0.70 wt% was calculated from the bulk S content (0.072 wt%) and the mass CO<sub>2</sub> and S ratio in the volcanic gas (9.8; A1 magma in Table 4), assuming that the mass CO<sub>2</sub> and S ratio in the volcanic gas was constant during the series of 2011 eruption. A bulk CO<sub>2</sub> content of 0.14 wt% was thus calculated using the bulk H<sub>2</sub>O content (4.0 wt%) and the mass CO<sub>2</sub> and H<sub>2</sub>O ratio in the volcanic gas (0.035; A2 magma in Table 4), assuming that the mass CO<sub>2</sub> and H<sub>2</sub>O ratio in the volcanic gas was constant during the series of 2011 eruption.

Similar to the method used for the 2011 mixed magma, the H<sub>2</sub>O, S, and Cl contents of a melt in the 2018 magma were calculated from the volatile contents in the andesite and rhyolite inclusions, assuming that the mixed melt in the 2018 magma was composed of mafic and felsic melts (Table 4). The following assumptions were made: (1) inclusion 18-1 V-p5i1, with the highest H<sub>2</sub>O content among all the inclusions in 2018-1VGP, can represent the mafic melt; (2) two felsic melts with low or high H<sub>2</sub>O contents were considered because the rhyolite inclusions particularly varied in terms of H<sub>2</sub>O content (0.5–3.5 wt%). Inclusion 18-1 V-p1i1 (has the highest H<sub>2</sub>O content among all the rhyolite inclusions in the 2018-1VGP) represents felsic melt 1, and inclusion 18-1 V-p2i1 (has the lowest H<sub>2</sub>O content among all the rhyolite inclusions in 2018-1VGP) represents felsic melt 2; and (3) a mixed melt has a SiO<sub>2</sub> content of 65 wt%, considering the SiO<sub>2</sub> content of groundmass of 2018-1VGP (Additional file 4). Mixing the 2018 mafic melt with 2018 felsic melt 1 gave a H<sub>2</sub>O content of 4.5 wt%, S content of 0.094 wt%, and Cl content of 0.091 wt% for 2018 mixed melt 1. Mixing the 2018 mafic melt with 2018 felsic melt 2 gave a H<sub>2</sub>O content of 3.1 wt%, S content of 0.082 wt%, and Cl content of 0.081 wt% for 2018 mixed melt 2. Based on the content of a phenocryst in 2018-1VGP (28 vol%; Additional file 2), a B1 magma with a bulk content of 3.0 wt% H<sub>2</sub>O, 0.063 wt% S, and 0.060 wt% Cl and a B2 magma with a bulk content of 2.1 wt% H<sub>2</sub>O, 0.054 wt% S, and 0.054 wt% Cl (Table 4) were obtained. Assuming super-saturation for CO<sub>2</sub> at the time of inclusion entrapment, we also calculated the bulk CO<sub>2</sub> content of the 2018 magma from the bulk S contents and mass CO<sub>2</sub>/S ratio in the volcanic gas. A bulk CO<sub>2</sub> content of 0.10 wt% was obtained from the bulk S content (0.063 wt%) and the mass ratio of CO<sub>2</sub> and S in the volcanic gas in October 2017 (1.6; GSJ/AIST 2017; B1 magma in Table 4). A bulk CO<sub>2</sub> content of 0.087 wt% was calculated from the bulk S content (0.054 wt%) and the same mass ratio of CO<sub>2</sub> and S in the volcanic gas (B2 magma in Table 4).

In addition, the bulk H<sub>2</sub>O, S, and Cl contents (6.2 wt% H<sub>2</sub>O, 0.138 wt% S, and 0.050 wt% Cl; Table 4) were estimated for the 2011 mafic magma from those of the 2011 mafic melt and phenocryst content (8.9 vol%) of the magma estimated by Suzuki et al. (2013b). The CO<sub>2</sub> content of the 2011 mixed melt was calculated to be 1.0 wt% from the bulk CO<sub>2</sub> content of A1 magma and its phenocryst content (28 vol%). Assuming that the CO<sub>2</sub> content of the 2011 felsic melt was equal to that of inclusion 11-2SG-p13i1 (0.048 wt%), which is the maximum in the rhyolite inclusions of the 2011 products, mass balance calculation yielded a CO<sub>2</sub> content of 1.5 wt% for the mafic melt from the CO<sub>2</sub> content of the 2011 mixed melt in A1 magma and the mixing ratio (mafic:felsic=0.67:0.33; Table 4). The bulk CO<sub>2</sub> content of the 2011 mafic magma (M1 magma in Table 4) was calculated to be 1.4 wt%, considering the phenocryst content (8.9 vol%). Similarly, in terms of the A2 magma, this calculation yielded a CO<sub>2</sub> content of 0.28 wt% for the mafic melt from the CO<sub>2</sub> content of the 2011 mixed melt in the A2 magma and the mixing ratio, resulting in a bulk CO<sub>2</sub> content of 0.25 wt% for the 2011 mafic magma (M2 magma in Table 4).

We could now estimate the bulk H<sub>2</sub>O, CO<sub>2</sub>, S, and Cl contents of the 2011 felsic magma, assuming that the H<sub>2</sub>O, CO<sub>2</sub>, S, and Cl contents of inclusion 11-2SG-p13i1 represent those of the felsic melt and no super-saturation of CO<sub>2</sub> occurred when the inclusions were entrapped. The bulk H<sub>2</sub>O, CO<sub>2</sub>, S, and Cl contents of felsic magma depend on the phenocryst content. Assuming that the felsic magma contained no phenocryst, a bulk content of 3.7 wt% H<sub>2</sub>O, 0.048 wt% CO<sub>2</sub>, 0.007 wt% S, and 0.087 wt% Cl were obtained (F1 magma in Table 4). However, if the phenocryst content was 43 vol%, as estimated for silicic-andesite magma by Suzuki et al. (2013b), a bulk content of 1.9 wt% H<sub>2</sub>O, 0.025 wt% CO<sub>2</sub>, 0.004 wt% S, and 0.045 wt% Cl is obtained (F2 magma in Table 4).

#### Chemical composition of melt in the magma

The chemical compositions of the groundmass in the 2018 products are slightly evolved as compared to the 2011 products (Fig. 4) in spite of the similarities between the whole-rock and phenocrysts chemical compositions from the two masses. MELTS calculation (Gualda et al. 2012) was used to investigate the differences in the whole-rock composition of 2011-2SGP (Table 2) and a temperature of 928 °C, pressures of 5–500 MPa, an FMQ+2 buffer of fO<sub>2</sub>, and the bulk H<sub>2</sub>O and CO<sub>2</sub> contents of the A1 and A2 magmas (4.0 wt% H<sub>2</sub>O and 0.70 wt% CO<sub>2</sub> or 0.14 wt% CO<sub>2</sub>; Additional file 9). The MELTS calculations indicate the presence of crystallized plagioclase, clinopyroxene, and orthopyroxene, and Fe–Ti oxide phenocrysts without any olivine phenocrysts (Additional file 9). The gas saturation pressures for the dacite–rhyolite inclusions

in the 2011 products (36–199 MPa) that were obtained in the previous section suggest that the pressure in the 2011 felsic magma chamber was 50–200 MPa. Melts in the A1 and A2 magmas have SiO<sub>2</sub> contents ranging from 65.37–71.48 wt% with 2.28–3.64 wt% K<sub>2</sub>O at pressures of 50–200 MPa (Fig. 4). These chemical compositions are slightly SiO<sub>2</sub>- and K<sub>2</sub>O-rich compared to the groundmass in the 2011 products (Fig. 4). Tomiya et al. (2013) proposed that the injection of mafic magma into the chamber occurred several weeks to days before the 2011 subplinian eruptions. Therefore, the difference between the chemical composition of the melts in the A1 and A2 magmas and the groundmass occurred because the 2011 mixed magma had not reached chemical equilibrium due to the short time period between mixing and eruption.

The MELTS calculation was also applied to the whole-rock composition of 2018-1VGP (Table 2) with a temperature of 944 °C, pressures of 5–500 MPa, an FMQ+2 buffer of fO<sub>2</sub>, and the bulk H<sub>2</sub>O and CO<sub>2</sub> contents of the B1 and B2 magmas (3.0 wt% H<sub>2</sub>O and 0.10 wt% CO<sub>2</sub> for B1 magma, 2.1 wt% H<sub>2</sub>O and 0.087 wt% CO<sub>2</sub> for B2 magma; Additional file 9). The MELTS calculation indicated crystallization of the plagioclase, clino- and orthopyroxene, and Fe–Ti oxide phenocrysts (Additional file 9) with melts containing SiO<sub>2</sub> contents of 66.31–70.76 wt% and 2.43–3.40 wt% K<sub>2</sub>O at pressures of 50–200 MPa. These chemical compositions are similar to the results for the A1 and A2 magmas and are similar or slightly SiO<sub>2</sub>- and K<sub>2</sub>O-rich compared to the groundmass in the 2018 products, except for that obtained for FeO (Fig. 4). The similar chemical compositions obtained for the groundmass in the 2018 products and the melts obtained by the MELTS calculation suggest that the 2018 magma was closer to chemical equilibrium. This suggests that the mixed magma from 2011 remained in the magma chamber and that the chemical reactions between the minerals and melt produced the 2018 magma. The rarity of olivine phenocrysts and lack of groundmass olivines in the 2018 products support this hypothesis because the results of the MELTS calculation indicate that olivines could not crystallize in the A1, A2, B1, and B2 magmas. The olivine phenocrysts that originated in the 2011 mafic magma, which were injected into the 2011 felsic magma, were probably dissolved in the mixed magma over time. The increase in the fractions of plagioclase phenocrysts with wide rims of >0.1 mm, and clinopyroxene and orthopyroxene phenocrysts with wide rims of >0.05 mm from the 2011 magma to the 2018 magma (mentioned previously), also supports this hypothesis.

In order to evaluate this hypothesis, compositional profiles from the core to the rim of 13 orthopyroxene phenocrysts from 2011-1PP to 2011-7VL and 12 orthopyroxene phenocrysts from 2018-1VGP and 2018-1VS

were measured, all of which show rims with reverse zoning under EPMA (Additional file 3). The compositional profiles of the orthopyroxene phenocrysts in the 2011 products show a large change in the Mg# at a distance of 0.02–0.03 mm from the rims, with widths of <0.005 mm. The Mg# profiles were calculated using Mg–Fe diffusion (e.g., Saunders et al. 2012) with a residence time of 1, 10, and 100 y at a temperature of 928 °C. The observed Mg# profiles were similar to those obtained for 1 y using the calculation (Additional file 3). Moreover, the compositional profiles of the orthopyroxene phenocrysts in the 2018 products show a large change in the Mg# at a distance of 0.04–0.10 mm from the rims. The widths of the Mg# range from 0.010 to 0.028 mm, which is larger than those obtained for the 2011 products, suggesting that Mg and Fe diffusion continued over this time period. The observed Mg# profiles appear to be closer to those obtained for 10 y by calculation (Additional file 3). Therefore, the observed compositional profiles of the core to rim of orthopyroxene phenocrysts in the 2011 and 2018 products are consistent with the above hypothesis, although more detailed analysis is required in the future.

#### Bubble volume and magma density

The density contrast between magma and crust can control the ascent of magma; magma can be trapped within a magma chamber if the density contrast becomes negligible (e.g., Walker 1989). In addition, the bubble volume of magma can control its eruption style; magmas with high bubble volume cause explosive eruptions, whereas those with poor bubble volume lead to effusive eruptions (e.g., Cashman and Mangan 1994). Therefore, obtaining the bubble volume and density of the magma is necessary to investigate the magma ascent and eruption processes. Both bubble volume and magma density are highly dependent on the bulk volatile content of a magma. Assuming that the gas bubbles formed by the exsolution of H<sub>2</sub>O and CO<sub>2</sub> from the melt did not separate from the magma during its ascent, the bubble volume and densities of the mafic and felsic magmas of the 2011 eruptions, the 2011 mixed magma, and the 2018 magma at different depths were calculated using the bulk H<sub>2</sub>O and CO<sub>2</sub> contents of the magma (Saito et al. 2018). Details of the calculation methods are provided in Additional file 9 and Additional file 4 of Saito et al. (2018).

The conditions applied for calculation of the 2011 mafic magmas (M1 and M2 magmas) were as follows: whole-rock composition and temperature of 1030 °C of basaltic–andesite magma estimated by Suzuki et al. (2013b), an oxygen fugacity controlled by the NNO buffer, and the bulk H<sub>2</sub>O and CO<sub>2</sub> contents of the M1 and M2 magmas (Table 4). The major-element compositions of the mafic melts at 50–500 MPa are similar to those of the andesite

inclusions in the olivine phenocryst (Fig. 6). The H<sub>2</sub>O and CO<sub>2</sub> contents of the mafic melts at 50–500 MPa are also similar to the distribution of the andesite inclusions (Figs. 7c, d, and 8a). These similarities indicate that the calculation results are close to the actual conditions. The calculation indicates that the mafic magmas (M1 and M2) had bubble volumes of 12.7–19.7 vol% and densities of 1987–2144 kg m<sup>-3</sup> at a pressure of 200 MPa (Additional file 9), indicating that mafic magma contained abundant bubbles and was of low density before it was injected into the felsic magma.

The conditions applied for calculation of the 2011 felsic magmas (F1 and F2 magmas) were as follows: a whole-rock composition of 2011-2SWP, the temperature of 870 °C for silicic–andesite magma estimated by Suzuki et al. (2013b), an oxygen fugacity controlled by 2 log units above the FMQ buffer, and the bulk H<sub>2</sub>O and CO<sub>2</sub> contents of the F1 and F2 magmas (Table 4). The major-element compositions of the felsic melts at 50–200 MPa are similar to those of the dacite–rhyolite inclusions in the 2011 products (Fig. 6). The H<sub>2</sub>O and CO<sub>2</sub> contents of the felsic melts at 50–200 MPa are also similar to the distribution in the dacite–rhyolite inclusions (Figs. 7c, d, and 8a). The calculation indicates that the felsic magmas (F1 and F2) had bubble volumes of <8.4 vol% and densities of 2264–2496 kg m<sup>-3</sup> at 125 MPa (Additional file 9), which is the pressure of the felsic magma chamber estimated using the gas saturation pressures for dacite–rhyolite inclusions in the 2011 products. Because the mafic magmas had lower densities of 1717–1835 kg m<sup>-3</sup> than the felsic magma at the same pressure, the density contrast may have caused mingling and mixing of the two magmas.

These calculations also provide information about the bubble volume and density of the 2011 mixed magma. Assuming that the chemical equilibrium obtained for the mixed magma is accurate, the 2011 mixed magma (A1 and A2 magmas) had a bubble volume of 3.2–9.2 vol% and a density of 2280–2401 kg m<sup>-3</sup> at 200 MPa, and 48.1–50.4 vol% and 1348–1402 kg m<sup>-3</sup> at 50 MPa. However, the difference between the chemical composition of the groundmass and that obtained by the MELTS calculation for the 2011 products reveals that the mixed magma had not attained chemical equilibrium upon eruption. Consequently, the above estimation for the A1 and A2 magmas might be an extreme example. Therefore, the bubble volume and density of the mixed magmas M1 (or M2) and F1 (or F2) were calculated by using the mass ratio for each magma in the mixing process (M1 or M2: F1 or F2=0.65:0.35; Additional file 10). This case defines the other extreme in which the two magmas simply “mingled” without any chemical reaction. The bubble volume and density of the mixed M1 + F1 magma are 13.8–57.1

vol% and 1162–2118 kg m<sup>-3</sup> at a pressure range of 50–200 MPa, whereas those of the M2 + F2 magma are 8.7–51.3 vol% and 1305–2263 kg m<sup>-3</sup>, respectively, at the same pressure range (Fig. 9; Additional file 10). These calculations indicate that the 2011 mixed magma had a high-volume content of approximately 50 vol% at a low pressure of 50 MPa, regardless of whether chemical equilibrium was attained in the magma.

Additionally, the bubble volume and density of the 2018 magma were calculated, assuming that chemical equilibrium was attained in this magma. The 2018 magma (B1 and B2 magmas) had a bubble volume of 0.5–1.1 vol% and a density of 2483–2549 kg m<sup>-3</sup> at 200 MPa, and 24.4–37.4 vol% and 1657–1983 kg m<sup>-3</sup> at 50 MPa. The bubble volume of the 2018 magma (24.4–37.4 vol%) at 50 MPa is smaller than those calculated for the M1 + F1 and M2 + F2 magmas (51.3–57.1 vol%) and the A1 and A2 magmas (48.1–50.4 vol%) at the same pressure (Fig. 9). Therefore, the lack of subplinian eruptions in 2018 may be because of the low bubble volume in the shallow part of the magma at that time.

#### Degassed-magma volume

The mass of degassed magma during volcanic activity is an important factor used in the degassing process investigations. The mass of degassed magma based on the estimated bulk volatile content of the 2011 and 2018 magmas, the measured SO<sub>2</sub> flux, and the chemical composition of the magmatic gas emitted from the summit crater, was calculated using the following equation:

$$M_{VE} = (C_{MM} - C_{DM}) \times M_{DM}$$

where  $M_{DM}$  is the mass of degassed magma (kg),  $C_{MM}$  is the bulk volatile content of the mixed magma (kg kg<sup>-1</sup>),  $C_{DM}$  is the bulk volatile content of the degassed magma (kg kg<sup>-1</sup>), and  $M_{VE}$  is the mass of the volatile material emitted from the summit crater (kg). The bulk volatile content of 0.072 wt% S and 0.044 wt% Cl (Table 4) that was obtained for the A1 (or A2) magma ( $C_{MM}$ ) was used to calculate the mass of degassed magma in 2011–12. The volatile content of degassed magma ( $C_{DM}$ ) was estimated from the S and Cl contents of the groundmass in the 2011 products (Additional file 4), assuming phenocryst contents of 28 vol% and no S or Cl contents in the phenocrysts. The mass of emitted sulfur was calculated from the SO<sub>2</sub> flux and the mole ratio of SO<sub>2</sub>/H<sub>2</sub>S (Additional file 11). The mole ratio was 8 on 15 March 2011, before decreasing to 0.8–3.3 after April (Shinohara 2013). Mole ratios of 8 and 2 were therefore assumed for these periods, respectively. We assumed a mole ratio of Cl/S was 0.235 based on the ratio in the ash–leachate (Vinet N Person. Communication; Additional file 11).

The mass of degassed magma (kg) was then converted to the degassed-magma volume ( $\times 10^6 \text{ m}^3$ ) for comparison with the erupted-magma volume and crust deformation, assuming a magma density of  $2500 \text{ kg m}^{-3}$ . The mass of the degassed magma in 2017–18 was also calculated for two cases in which the magma had: (1) the bulk S content of the B1 magma (0.063 wt% S) and (2) the bulk S content of the B2 magma (0.054 wt% S) before degassing (Table 4). The bulk S content of the magma after degassing was calculated from the minimum S content of the groundmass (0.002 wt% of 2018-4L1 in Additional file 4) and the phenocryst content (28 vol%) of the 2018 products. The mole ratio of  $\text{SO}_2$  and  $\text{H}_2\text{S}$  in the volcanic gas was assumed to be 2.7 based on observation of the volcanic gas (Additional file 11). A detailed description of the calculation used for the degassed magmas is given in Table 5 and Additional file 11. If the average, minimum, and maximum  $\text{SO}_2$  flux values are observed over a single day, the maximum value is at most 2.3 times larger and the minimum value is 0.2 times larger than the average, except for extremely high maximum value (2900 t/d), as compared to the average (770 t/d) observed on 25 February 2011 (Additional file 11). This suggests that an error of 20–230% for the degassed-magma volume is unavoidable.

The degassed-magma volume in 2011–12 is summarized in four periods, depending on the eruption style (Table 5). The degassed-magma volume calculated from bulk S content in each period is 1.25–1.5 times larger than that calculated from bulk Cl content (Table 5). Ratios of the degassed-magma volume calculated from bulk S content and that calculated from bulk Cl content

gradually increased with time; 1.25 on 26–27 January, 1.33 on 28 January–1 February, 1.38 on 2 February–7 September, and 1.5 on 8 September 2011–26 September 2012. The reason for the difference is unknown; however, the assumption that the molar ratio of Cl and S in the volcanic gas observed on 27 January 2011 (0.235) was constant during all periods in 2011–12 might cause the difference. Considering the uncertainty of molar ratio of Cl and S in the volcanic gas during 2011–12, we use only the degassed-magma volumes calculated from bulk S content in following discussion. The degassed-magma volume on 26–27 January ( $5 \times 10^6 \text{ m}^3$ ) seems to be smaller than the volume of magma that was erupted ( $7\text{--}11 \times 10^6 \text{ m}^3$ ; Maeno et al. 2014) during the subplinian eruptions on 26–27 January. However, considering the error in the  $\text{SO}_2$  flux measurement mentioned previously (20–230%), the degassed-magma volume is likely consistent with erupted-magma volume. The volume of degassed magma on 28 January–1 February ( $32 \times 10^6 \text{ m}^3$ ) was 2.1 times larger than that of erupted magma in the same period ( $15 \times 10^6 \text{ m}^3$ ; Kozono et al. 2013; Nakada et al. 2013). Similar to the case on 26–27 January, the degassed-magma volume is likely consistent with erupted-magma volume considering the error in the  $\text{SO}_2$  flux measurement mentioned above. This indicates that the  $\text{SO}_2$  gas emission on 28 January–1 February could be explained by degassing of the lava effused in the summit crater. On the other hand, the degassed-magma volume on 2 February–7 September ( $18 \times 10^6 \text{ m}^3$ ) is more than 90 times greater than that of the erupted magma in the same period ( $< 0.2 \times 10^6 \text{ m}^3$ ; Nishiki et al. 2013). Furthermore, during the period 8

(See figure on next page.)

**Fig. 9** Physical properties of magmas associated with the 2011 and 2018 eruptions at a pressure range of 5 to 500 MPa (M1 and M2 magmas at pressure ranges of 5–500 MPa and F1, F2, M1 + F1, M2 + F2, A1, A2, B1 and B2 magmas at pressure ranges of 5–200 MPa) calculated from bulk volatile content (Table 4) using MELTS calculation and the molar volume of the  $\text{H}_2\text{O}$  and  $\text{CO}_2$  gases (Additional file 8): **a** Bubble volume of magmas (vol%), **b** Density of magmas ( $\text{kg m}^{-3}$ ), **c** Melt fraction of magmas (vol%), and **d** Melt viscosity of magmas ( $\log \text{ Pa s}$ ). Further data is given in Additional files 9 and 10. Dark gray areas in **a** to **d** indicate depth of crustal deformation estimated by geophysical observation during 2009–2018 (6–10 km; GIAJ 2012; Ueda et al. 2013; Nakao et al. 2013; JMA 2019a). Light gray areas in **a** to **d** indicate depth of the silicic andesite magma chamber estimated by petrological study of the 2011 products (105–135 MPa; Suzuki et al. 2013b). Black broken lines in **a** indicate maximum and minimum porosities of the subplinian eruption products from 2011 (42–45 vol% for 2011-2SGP and 2011-3SGP; Additional file 2). The same bubble volumes are reproduced in the M1 + F1 to M2 + F2 magmas at pressure ranges of 50–75 MPa. Red broken lines in **a** indicate maximum and minimum porosities of the vulcanian eruption products in 2018 (19–49 vol% for 2018-1VGP, 2018-1VS, 2018-2VGP, and 2018-2VS; Additional file 2). The same bubble volumes were reproduced in B1 and B2 magmas at pressure ranges of 25–100 MPa. Broken lines in **b** indicate expected density structure of the crust based on a study by JMA (2013) that reports densities of  $2000\text{--}2500 \text{ kg m}^{-3}$  at depths of less than 0 km bsl (equivalent to depths of less than 1 km beneath the Shinmoedake summit) and approximately  $2500 \text{ kg m}^{-3}$  at depths of 0–1 km bsl (equivalent to depths of 1–2 km beneath the Shinmoedake summit) based on analyses of borehole samples around the Kirishima volcanoes. We assumed a density structure of  $2000\text{--}2500 \text{ kg m}^{-3}$  at a depth of 0–1 km and  $2500 \text{ kg m}^{-3}$  at depths of more than 1 km beneath Shinmoedake by considering the height of the Shinmoedake summit crater above sea level prior to the 2011 eruptions (1.2 km). Black broken lines in **c** indicate maximum and minimum groundmass content of the subplinian eruption products in 2011 (72–74 vol% for 2011-2SGP and 2011-3SGP). The same melt contents are reproduced in the M1 + F1 and M2 + F2 magmas at pressure ranges of 50–100 MPa. Red broken lines in **c** indicate maximum and minimum groundmass content in the vulcanian eruption products from 2018 (70–73 vol% for 2018-1VGP, 2018-1VS, 2018-2VGP, and 2018-2VS; Additional file 2). The same melt content was reproduced in the B1 magma at pressure ranges of 125–300 MPa; however, this melt content was not obtained for the B2 magma at pressure ranges of 5–500 MPa (Additional file 9), which suggests that the B1 magma with an  $\text{H}_2\text{O}$  content of 3.0 wt% might be more realistic for 2018 than the B2 magma. Blue curves with arrows (i) show expected physical property changes in the 2011 mafic magma during its ascent. Gray curves with arrows (ii) and red curves with arrows (iii) show expected physical property changes in the 2011 and 2018 magmas during their ascent, respectively

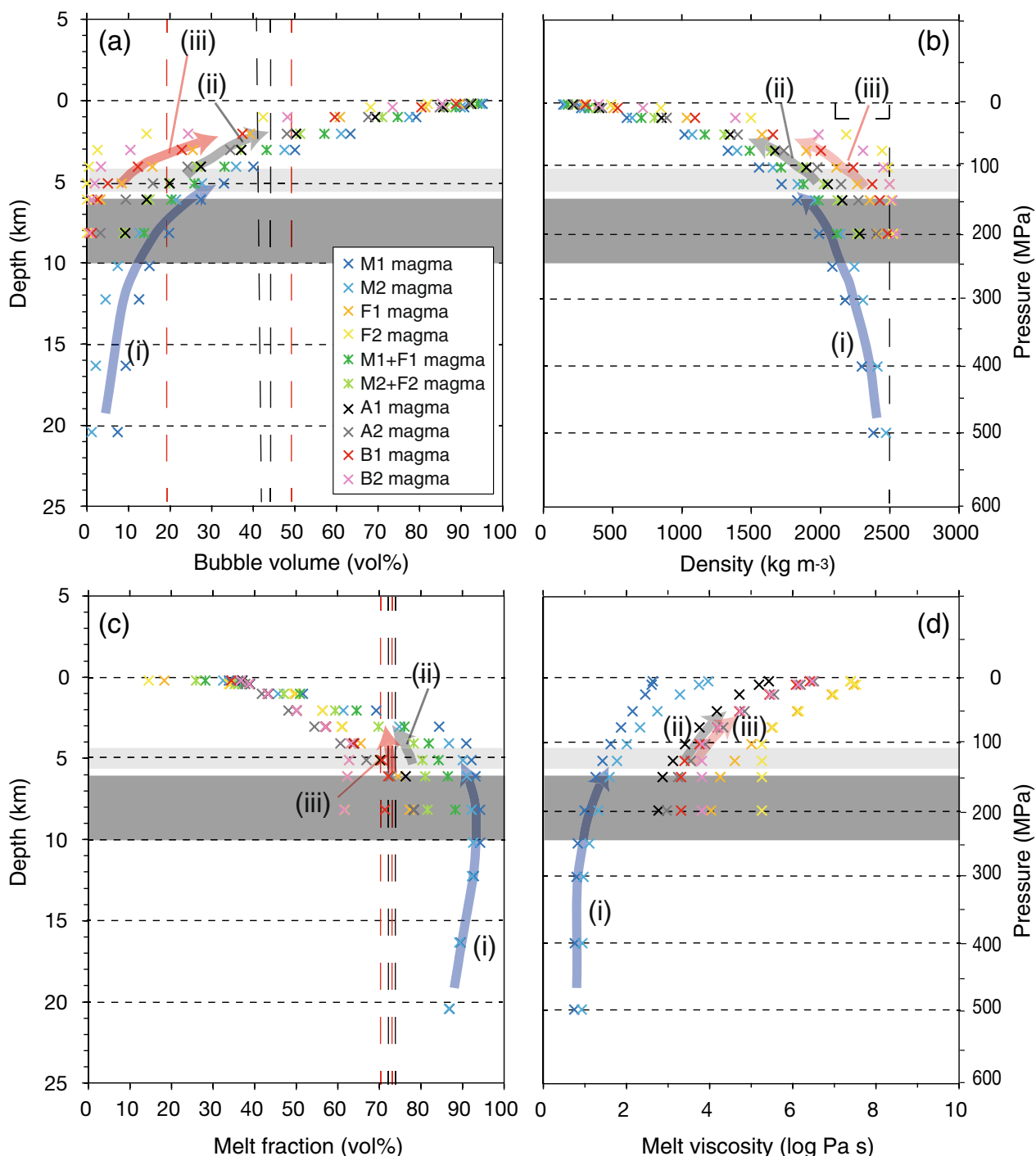


**Fig. 9** (See legend on previous page.)

September 2011–26 September 2012, approximately  $3 \times 10^6 \text{ m}^3$  of magma was degassed, although none was erupted. The excess degassing during the period 2 February 2011–26 September 2012 indicates that the magmatic gas was derived from the non-erupted magma located in a deeper part of the chamber. Because the

magma chamber is located at a depth of approximately 5 km (Suzuki et al. 2013b), such degassing may be due to magma convection in a conduit (Shinohara 2008). This excess degassing may have decreased the bulk volatile content of the 2011 magma in the chamber over time. Decrease in volatile content of magma in a

**Table 5** Degassed-magma volume for 2011–12 and 2017–18 calculated from the bulk S and Cl contents of the magmas and volcanic gas observation. List of erupted-magma volume and crustal deformation estimated from geological and geophysical observations

Date	Eruption style	Degassed magma <sup>a</sup>		Magma erupted <sup>b</sup> (10 <sup>6</sup> m <sup>3</sup> DRE)	Degassed magma/ Erupted magma		Crustal deformation estimated based on GPS observation (10 <sup>6</sup> m <sup>3</sup> ) <sup>c</sup>
		S	Cl		S	Cl	
		(10 <sup>6</sup> m <sup>3</sup> )	(10 <sup>6</sup> m <sup>3</sup> )				
2011–12							
26–27 Jan. 2011	Subplinian eruptions	5	4	7–11	0.5–0.7	0.4–0.6	+18~+21 (1 Nov. 2009—25 Jan. 2011) -13~-14 (25 Jan–1 Feb. 2011)
28 Jan.–1 Feb. 2011	Lava effusion with Vulcanian eruptions	32	24	15	2.1	1.6	
2 Feb.–7 Sep. 2011	Vulcanian eruptions, Ash emissions	18	13	<0.2	>90	>65	
8 Sep. 2011–26 Sep. 2012	No eruption with gas emission	3	2	0			+11 (1 Feb–1 Dec. 2011)
Total		58	43	22–26	2.2–2.6	1.7–2.0	
Date	Eruption style	Degassed magma <sup>d</sup>		Magma erupted <sup>e</sup> (10 <sup>6</sup> m <sup>3</sup> DRE)	Degassed magma/ Erupted magma		Crustal deformation estimated based on GPS observation (10 <sup>6</sup> m <sup>3</sup> ) <sup>f</sup>
		S (B1)	S (B2)		S (B1)	S (B2)	
		(10 <sup>6</sup> m <sup>3</sup> )	(10 <sup>6</sup> m <sup>3</sup> )				
2017–18							
11–16 Oct. 2017	Ash emissions	10	11	na			+11 (1 Jul. 2017–1 Mar. 2018)
17 Oct. 2017–28 Feb. 2018	No eruption with gas emission	4	4	0			
1 Mar.–9 Mar. 2018	Lava effusion with Vulcanian eruptions and ash emissions	29	33	15(lava, 6 Mar.–9 Mar.)	1.9	2.2	-7 (1 Mar–10 Mar.2018)
10 Mar.–27 Jun. 2018	Vulcanian eruptions, Ash emissions	5	6	0.3 (tephra, 1 Mar.–14 May)	17	20	+10 (10 Mar. 2018–31 Jan. 2019)
28 Jun.–13 Oct. 2018	No eruption with gas emission	3	3	0			
Total		51	57	15	3.4	3.8	

<sup>a</sup> Mass of the degassed magma was calculated from bulk S content of 0.072 wt% of A1 and A2 magmas (Table 4), bulk S content (0.0013 wt%) of the magma after degassing, chemical composition of volcanic gas and SO<sub>2</sub> flux. The bulk S content after degassing was calculated from minimum S content of the groundmass of 2011-25GP (0.002 wt%; Additional file 4) and the phenocryst content (28 vol%; Additional file 2). The SO<sub>2</sub> flux used in this calculation are shown in Additional file 11. We also calculated mass of the degassed magma from bulk Cl content of 0.044 wt% (A1 and A2 magmas in Table 4), bulk Cl content (0.020 wt%) of the magma after degassing, the chemical composition of the volcanic gas and the SO<sub>2</sub> flux. The bulk Cl content after degassing was calculated from minimum Cl content of the groundmass (0.030 wt% of 2011-7VL in Additional file 4) and the phenocryst content (28 vol%). Degassed-magma volume was obtained from the mass of the degassed magma assuming a rock density of 2500 kg m<sup>-3</sup>

<sup>b</sup> Data on amount of tephra and lava are from Maeno et al. (2014), Nakada et al. (2013), Kozono et al. (2013), Nishiki et al. (2013). Erupted-magma volume of the subplinian eruptions on 26–27 January was calculated from total mass of tephra (1.8–3.1 × 10<sup>10</sup> kg; Nakada et al. 2013), assuming a rock density of 2500 kg m<sup>-3</sup>. Erupted-magma volume on 28 January—1 February was based on that of lava effused within the summit crater (Kozono et al. 2013; Nakada et al. 2013). Erupted-magma volume on 2 February -7 September was after Nishiki et al. (2013)

<sup>c</sup> Crustal deformation data from Nakao et al. (2013) and JMA (2019a)

<sup>d</sup> Mass of degassed magma as shown in S (B1) was calculated from bulk S content (0.063 wt%) of B1 magma in Table 4), bulk S content (0.0013 wt%) of the magma after degassing, chemical composition of volcanic gas and SO<sub>2</sub> flux. The bulk S content after degassing was calculated from minimum S content of the groundmass of the 2018 eruptives (0.002 wt% of 2018-4L1 in Additional file 4) and the phenocryst content (28 vol%) of 2018-1VGP (Additional file 2). The SO<sub>2</sub> flux used in this calculation are shown in Additional file 11. In addition, mass of degassed magma as shown in S (B2) was calculated using bulk S content of B2 magma (0.054 wt%; Table 4) and the same bulk S content of the magma after degassing (0.0013 wt%), the SO<sub>2</sub> flux and the mol ratio of SO<sub>2</sub> and H<sub>2</sub>S of the volcanic gas. Degassed-magma volume was obtained from the mass of the degassed magma assuming a rock density of 2500 kg m<sup>-3</sup>. Estimation on amount of degassed magma using bulk Cl content of the magma could not be carried out because of lack of data on mole ratio of Cl and S in the volcanic gas in 2017–18

<sup>e</sup> Data on amount of tephra and lava are from Chiba et al. (2018), Oikawa et al. (2018)

<sup>f</sup> Crustal deformation data are from JMA (2019a)



magma chamber by excess degassing was also proposed for Satsuma-Iwojima volcano by Saito et al. (2003). They reported that H<sub>2</sub>O content of the rhyolite magma in the magma chamber decreased from 3 wt% to 1 wt% by magma convection in a conduit during the active degassing period of more than 800 years.

GPS observation indicates that deflation reaching 13–14 × 10<sup>6</sup> m<sup>3</sup> occurred between 25 January–1 February, which could be explained by the discharge of magma from the chamber to the surface (Nakada et al. 2013). The crustal deflation changed to inflation on 25 February, and this continued until December 2011. GPS observation indicates that the total volume of the inflation was 11 × 10<sup>6</sup> m<sup>3</sup> (Table 5). The inflation could be explained by continuous replenishment of the magma chamber from a deep source (Nakada et al. 2013; Nakao et al. 2013; Suzuki et al. 2013b). The mafic-magma proportion of the degassed magma on 2 February 2011–26 September 2012 could be 14 × 10<sup>6</sup> m<sup>3</sup> using a mixing ratio of 0.65 for mafic-to-mixed magma (Suzuki et al. 2013b) and a degassed-magma volume of 21 × 10<sup>6</sup> m<sup>3</sup> (Table 5). This estimate is similar to the inflation of the chamber observed by GPS, suggesting that mafic magma was injected to the chamber from deeper in the volcano during February–December 2011, causing inflation of the magma chamber, gas emission, and small eruptions.

As previously mentioned, the excess degassing of the magma chamber could decrease the volatile content of the chamber. However, if the mafic magma injected to the chamber had high volatile content as in M1 and M2 magmas (Table 4), the input of volatiles from the mafic magma to the chamber could cancel decrease in volatile content of magma by the excess degassing or might increase it. To evaluate the effects of both the excess degassing and mafic-magma input on volatile content of the magma chamber, mass balance calculation on sulfur in the 2011 magma were conducted as follows. Assuming inflation of the magma chamber of 18–21 × 10<sup>6</sup> m<sup>3</sup> at a depth of 8 km observed from 1 November 2009 to 25 January 2011 (Table 5; Nakao et al. 2013; JMA 2019a) was caused by injection of M1 or M2 magma, mass of the mafic magma (3.6–4.5 × 10<sup>10</sup> kg; Additional file 12) was calculated using the volume of inflation and densities of M1 and M2 magmas (1987 and 2144 kg m<sup>-3</sup> at 200 MPa; Additional file 9). Therefore, mass of 2011 magma (5.5–6.9 × 10<sup>10</sup> kg) was obtained from the mass of the mafic magmas and a mixing ratio of mafic and felsic magmas (mafic:felsic=0.65:0.35; Suzuki et al. 2013b). Assuming that the 2011 magma was composed of A1 or A2 magma, mass of S in the 2011 magma (4.0–5.0 × 10<sup>7</sup> kg; Additional file 12) was calculated from sulfur content of A1 (A2) magma (0.072 wt%; Table 4). Inflation of the magma chamber (11 × 10<sup>6</sup> m<sup>3</sup> at a depth of 8 km) was also

observed from 1 February to 1 December 2011 (Table 5; Nakao et al. 2013; JMA 2019a). Similar to the case of the inflation from 1 November 2009 to 25 January 2011, mass of the mafic magma injected into the chamber during this period was calculated to be 2.2–2.4 × 10<sup>10</sup> kg from the volume of inflation and densities of M1 and M2 magmas (1987 and 2144 kg m<sup>-3</sup> at 200 MPa; Additional file 9). Therefore, mass of the 2011 magma formed during this period (3.4–3.6 × 10<sup>10</sup> kg; Additional file 12) was obtained from the mass of the mafic magmas and mixing ratio of the mafic and felsic magmas. Assuming that the 2011 magma was composed of A1 or A2 magma, mass of S in the 2011 magma (2.4–2.6 × 10<sup>7</sup> kg; Additional file 12) was calculated from sulfur content of A1 (A2) magma (0.072 wt%; Table 4). Therefore, total mass of sulfur of the 2011 magma formed by the mixing process during 1 November 2009–1 December 2011 was 6.4–7.6 × 10<sup>7</sup> kg. In contrast, mass of sulfur emitted from the summit from 27 January 2011 to 26 September 2012 was calculated to be 1.0 × 10<sup>8</sup> kg based on averages of SO<sub>2</sub> fluxes and mole ratios of SO<sub>2</sub> and H<sub>2</sub>S in the volcanic gas (Additional file 11). This value is similar or a little larger than the total mass of sulfur in the 2011 magma in the chamber (6.4–7.6 × 10<sup>7</sup> kg), suggesting that the degassing in this period possibly caused decrease in volatile content of the 2011 magma, in spite of injection of mafic magmas with high volatile content as M1 and M2 magmas. The above comparison indicates that all sulfur in the 2011 magma was emitted as volcanic gas until September 2012, whereas sulfur content of 0.054–0.060 wt% was estimated for B1 and B2 magmas (Table 4). Notably, the estimation on total mass of sulfur emitted from the summit highly depends on accuracy of SO<sub>2</sub> flux measurement and its supposed error of 20–230%. Thereafter, we speculate that overestimation of SO<sub>2</sub> flux might result in greater value of calculated mass of emitted sulfur than the actual mass of sulfur in the 2011 magma in the chamber. For example, if 40% of average SO<sub>2</sub> flux (4.0 × 10<sup>7</sup> kg) is used for the above calculation, sulfur content of the magma after the degassing was calculated to be 0.029–0.064 wt%, similar to sulfur content of B1 and B2 magmas (0.060 and 0.054 wt%, respectively; Table 4). More quantitative study on sulfur budget of the 2011 magma chamber requires accurate estimation of mass of sulfur emitted from the magma chamber.

The degassed-magma volume in 2017–18 is summarized for five periods, depending on the kind of eruption that occurred (Table 5). The degassed-magma volume estimated for 11 October 2017–28 February 2018 (14–15 × 10<sup>6</sup> m<sup>3</sup>) is much larger than the erupted-magma during this period. The degassed-magma volume for 1 March–9 March (29–33 × 10<sup>6</sup> m<sup>3</sup>) is 1.9–2.2 times greater than the magma erupted in the same period

( $15 \times 10^6 \text{ m}^3$ ; Chiba et al. 2018). Considering the error in the  $\text{SO}_2$  flux measurement, the degassed-magma volume on 1 March–9 March is similar to the volume of erupted-magma, indicating that all the  $\text{SO}_2$  gas emitted in the summit crater was derived from the lava erupted during this period. The degassed-magma volume for 10 March–27 June ( $5\text{--}6 \times 10^6 \text{ m}^3$ ) is 17–20 times larger than erupted-magma volume in the same period ( $0.3 \times 10^6 \text{ m}^3$ ; Oikawa et al. 2018). Furthermore,  $3 \times 10^6 \text{ m}^3$  of magma was degassed from 28 June–13 October 2018, although no magma was erupted. Similar to 2011–12, a large degassed-magma volume greater than the erupted-magma volume was observed in a period of vulcanian eruptions that occurred with ash and gas emissions, suggesting that the degassing occurred by convection in a conduit (Shinohara 2008). GPS observation indicates that the deflation of the crust after 1 March reverted to inflation on 10 March and that the inflation continued until January 2019, with a total volume of  $10 \times 10^6 \text{ m}^3$  (Table 5). As discussed for 2011–12, the magma chamber must have undergone replenishment from a deep source during this period, causing inflation of the magma chamber, gas emission, and small eruptions.

#### Ascent and degassing processes of the magma

Based on the above estimation of the physical and chemical conditions in the magmas and the degassed-magmas, the magma ascent and degassing processes were estimated for the 2011 and 2017–18 Shinmoedake eruptions (Fig. 10). The subplinian eruptions in January 2011 were the result of mixed mafic and felsic magma. The mafic magma had basaltic–andesite composition, whereas the felsic magma had silicic–andesite composition, and the proportion of basaltic–andesitic magma in the mixed magma ranged from 0.6 to 0.7 (Suzuki et al. 2013b). The felsic magma must have been stored at a pressure of 70–177 MPa (equivalent to a depth of 3–7 km from the Shinmoedake summit; Fig. 10), considering the gas saturation pressures for the dacite–rhyolite inclusions in the 2011 products that were obtained using the two solubility models ( $120 \pm 50$  and  $152 \pm 25$  MPa). The felsic magma had relatively lower bulk volatile content (1.9–3.7 wt%  $\text{H}_2\text{O}$ , 0.025–0.048 wt%  $\text{CO}_2$ , 0.004–0.007 wt% S, and 0.045–0.087 wt% Cl; Table 4), bubble volumes of <9.3 vol%, and a bulk density of  $2241\text{--}2496 \text{ kg m}^{-3}$  at 125 MPa (Figs. 9 and 10). The density structure beneath Shinmoedake is estimated to be  $2000\text{--}2500 \text{ kg m}^{-3}$  at depths of <0 km bsl and approximately  $2500 \text{ kg m}^{-3}$  at depths of 0–1 km bsl (JMA 2013). Assuming that the density of the crust is  $2500 \text{ kg m}^{-3}$  at depths of >0 km bsl (equivalent to depths of >1 km beneath the summit), the felsic magma may not be able to ascend to shallower depths

because of the small contrast between the density of felsic magma and the crust. Considering that the major-element composition of 1716–17WP is similar to that of 2011–2SWP (Table 2; Fig. 2), which was likely derived from the felsic magma, the felsic magma can be assumed to have remained in the chamber following the 1716–17 eruptions.

The mafic magma with bulk volatile content of 6.2 wt%  $\text{H}_2\text{O}$  and 0.25–1.4 wt% of  $\text{CO}_2$  may have ascended from a depth of 19 km (at a pressure of 486 MPa) based on the gas saturation pressures of the andesite inclusions in the olivines from the 2011 products ((i) in Fig. 9). The mafic magma had bubble volumes of 27.6–33.0 vol% and densities of  $1717\text{--}1835 \text{ kg m}^{-3}$  at 125 MPa (M1 and M2 in Additional file 9). The lower density of the mafic magma than that of felsic magma ( $2264\text{--}2496 \text{ kg m}^{-3}$ ; Fig. 9; Additional file 9) suggests that it may have been injected into the felsic magma chamber, promoting mixing of the two magmas ((i) in Fig. 9). Comparison between the results of the MELTS calculation and the chemical composition of the groundmass in the 2011 products indicates that the mixed magma did not attain chemical equilibrium before eruption. Densities of  $1875\text{--}2022 \text{ kg m}^{-3}$  for the M1 + F1 and M2 + F2 magmas (Additional file 10) and  $2050\text{--}2147 \text{ kg m}^{-3}$  for the A1 and A2 magmas (Additional file 9) were obtained at a pressure of 125 MPa. Both densities are lower than that of the surrounding felsic magma at the same pressure ( $2264\text{--}2496 \text{ kg m}^{-3}$ ; Additional file 9), suggesting that the mixed magma may have continued ascending ((ii) in Fig. 9). Furthermore, the ascending mixed magma had bubble volumes of 51.3–57.1 vol% (M1 + F1 and M2 + F2 magmas; density of  $1162\text{--}1305 \text{ kg m}^{-3}$ ; Additional file 10) or 48.1–50.4 vol% (A1 and A2 magmas; density of  $1348\text{--}1402 \text{ kg m}^{-3}$ ; Additional file 9) at a pressure of 50 MPa. Such bubble-rich magma could have caused the subplinian eruptions (Fig. 10). Remarkably, the above densities and the bubble volumes were calculated with the assumption that gas bubbles that formed from the exsolution of  $\text{H}_2\text{O}$  and  $\text{CO}_2$  from the melt do not separate from the magma during its ascent. If the bubbles separated from the magma and rose up to an upper part of the chamber, the magma erupted at the subplinian eruptions could have a higher bubble volume than the above estimates. The chemical composition of the groundmass in March–August 2011 seems more evolved than that in January–February, and becomes close to that predicted by MELTS for a melt in the mixed magma, indicating that the chemical reaction partially proceeded in the magma during the period March–August (Fig. 10). Moreover, the volume of degassed-magma from 2 February 2011 to September 2012 was more than 105 times greater than that of the eruptive products during the same period.

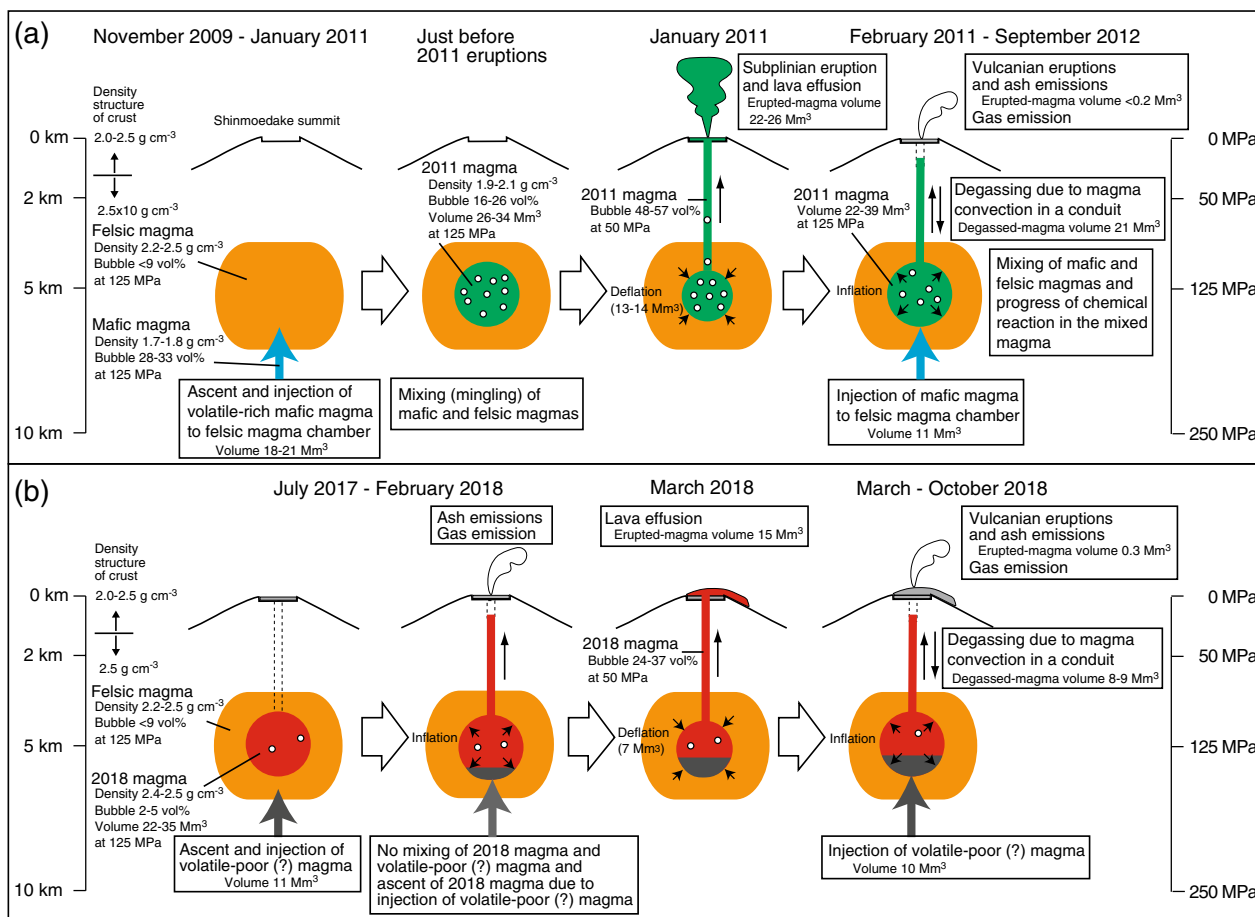


**Fig. 10** Schematic diagram of magma ascent and degassing processes of **a** 2011 and **b** 2017–18 eruptions of Shinmoedake volcano. The left axis shows depths below the summit of Shinmoedake. Expected density structure of crust around the Kirishima volcano based on a study by JMA (2013) is also shown. Densities and volumes of bubbles in mafic, felsic, 2011 and 2018 magmas at 125 MPa and 50 MPa estimated in this study are shown. Erupted-magma volumes for 26 January – 1 February 2011 ( $22\text{--}26 \times 10^6 \text{ m}^3$ ), 2 February – 26 September 2011 ( $<0.2 \times 10^6 \text{ m}^3$ ), 6–9 March 2018 ( $15 \times 10^6 \text{ m}^3$ ) and 1 March–14 May 2018 ( $0.3 \times 10^6 \text{ m}^3$ ) and degassed-magma volumes for 2 February 2011 – 26 September 2012 ( $21 \times 10^6 \text{ m}^3$ ) and 10 March–13 October 2018 ( $8\text{--}9 \times 10^6 \text{ m}^3$ ; Table 5) are also shown. Volumes of mafic magmas injected to the magma chamber ( $18\text{--}21 \times 10^6 \text{ m}^3$  from 1 November 2009 to 25 January 2011,  $11 \times 10^6 \text{ m}^3$  from 1 February to 1 December 2011,  $11 \times 10^6 \text{ m}^3$  from 1 July 2017 to 1 March 2018 and  $10 \times 10^6 \text{ m}^3$  from 10 March 2018 to 31 January 2019) are estimated from inflation of the magma chamber estimated from GPS observations (Nakao et al. 2013; JMA 2019a), assuming that the inflations were caused by injections of mafic magmas. Volumes of deflation of the magma chamber from 25 January to 1 February 2011 and from 1 to 10 March 2018 were estimated from GPS observations (Nakao et al. 2013; JMA 2019a). Volumes of the 2011 and 2018 magmas in the chamber estimated in this study ( $26\text{--}34 \times 10^6 \text{ m}^3$  of the 2011 magma just before the 2011 eruptions,  $22\text{--}39 \times 10^6 \text{ m}^3$  of the 2011 magma in February 2011 to September 2012 and  $22\text{--}35 \times 10^6 \text{ m}^3$  of the 2018 magma in July 2017; see Additional file 12 for details) are also shown. See text for details

This suggests that the magma in the chamber underwent degassing due to the convection of magma in a conduit (Fig. 10). This excess degassing may have decreased the bulk volatile content in the 2011 magma, overcoming volatile input from mafic magma injected into the chamber during the same period.

The similar whole-rock composition and variations in the plagioclase-, clinopyroxene-, and orthopyroxene-phenocryst cores of the 2011 and 2018 magmas indicates that the 2011 mixed magma remained following eruption. Similar gas saturation pressures (with averages of  $118 \pm 45$  and  $144 \pm 44$  MPa by the two solubility

models) were obtained from the  $\text{H}_2\text{O}$  and  $\text{CO}_2$  contents of the andesite–rhyolite inclusions in the 2018 products, indicating that the depth of the magma chamber did not change during 2011–2018. However, the rarity of the olivine phenocrysts; wide rims of plagioclase, clinopyroxene and orthopyroxene phenocrysts in the 2018 products; and the comparison between the MELTS calculation and groundmass in the 2018 products indicate that that chemical reaction of the magma proceeded to reach equilibrium. The estimated bulk volatile contents for the 2018 magma (3.0 wt%  $\text{H}_2\text{O}$  and 0.10 wt%  $\text{CO}_2$  for B1 magma, and 2.1 wt%  $\text{H}_2\text{O}$  and 0.087 wt%  $\text{CO}_2$  for B2

magma; Table 4) are lower than those obtained for the 2011 magma. The decrease in the volatile content may have been caused by the excess degassing of the 2011 magma in the magma chamber following the eruptions.

The density of the 2018 magma was 2374–2498 kg m<sup>-3</sup> at a pressure of 125 MPa, which is similar to that of the surrounding felsic magma (2264–2496 kg m<sup>-3</sup>; Fig. 9). Considering the small contrast between the density of the 2018 magma and surrounding felsic magma, the 2018 magma may not have ascended via buoyancy. Instead, the injection of new magma into the bottom of the 2018 magma chamber, inferred from the crust inflation from June 2017 to March 2018 (JMA 2019a), may have forced the 2018 magma into shallower depths, resulting in the 2018 eruptions ((iii) in Fig. 9; Fig. 10). We speculate that the new magma had relatively low bulk volatile content because if the magma had high volatile content like the 2011 mafic magma, it could have turned over to mix with the 2018 magma before eruption. The lower bubble volume of the 2018 magma (24.4–37.4 vol% at 50 MPa; (iii) in Fig. 9) is likely to have led to effusive rather than explosive eruption (Fig. 10). After the lava effusion in March 2018, the volume of degassed magma present was greater than the volume of erupted magma (more than 27-fold; Table 5), suggesting the degassing of magma by convection in a conduit. GPS observation indicates a total volume of 10×10<sup>6</sup> m<sup>3</sup> for the inflation that occurred from 10 March to 31 January 2019 (Table 5), suggesting that new magma injected into the chamber from greater depths. This injection of the magma might further push the upper 2018 magma in the chamber to cause vulcanian eruptions and ash and gas emissions (Fig. 10).

## Summary and conclusions

- a) Petrological observation and melt-inclusion analysis of products from the 2011 and 2018 eruptions at Shinmoedake in the Kirishima volcanic group were conducted to investigate the magma ascent and degassing processes. Whole-rock and chemical compositions of plagioclase-, clinopyroxene-, and orthopyroxene-phenocryst cores from the 2018 products were found similar to those of the 2011 products, suggesting that the 2018 magma was a remnant of the 2011 magma. Comparison of the mode and chemical compositions of the groundmass in the 2018 products with the results obtained using MELTS indicates that the magma approached chemical equilibrium between 2011 and 2018, suggesting that the changes observed could be explained by the magma approaching chemical equilibrium.
- b) Melt-inclusion analysis reveals that the inclusions obtained for the 2011 eruptions can be divided into two types; andesite inclusions in olivine phenocrysts and dacite–rhyolite inclusions in plagioclase, clinopyroxene, and orthopyroxene phenocrysts. Large variations were observed in the volatile content of the andesite and dacite–rhyolite inclusions, which are not correlated with the SiO<sub>2</sub> or K<sub>2</sub>O contents in the inclusions, indicating degassing of the andesite and dacite–rhyolite melt. The inclusions from the 2018 eruptions have andesite-to-rhyolite compositions with no gaps in the chemical compositions. Large variations were also observed in the H<sub>2</sub>O, S, and Cl contents of the andesite–rhyolite inclusions from the 2018 eruptions, which are roughly correlated with the SiO<sub>2</sub> contents of the inclusions, indicating that mafic melt with high H<sub>2</sub>O and S contents and low Cl content was mixed with felsic melt of low H<sub>2</sub>O and S contents and high Cl content.
- c) Two-pyroxene thermometry (Putirka 2008) was applied to the compositions of the borders of intergrown clinopyroxene and orthopyroxene phenocrysts from the 1716–17, 2011, and 2018 eruptions, with results indicating that the temperature of the 2018 magma was similar to those of both the 2011 and the 1716–17 magmas. The application of Fe–Ti oxide thermometry to the compositions at the borders of the intergrown magnetite and ilmenite phenocrysts from the 2018 products gave temperature and oxygen fugacity estimates similar to those obtained for the 2011 and 1716–17 magmas. These results indicate that the temperature and oxidation state of the magma chamber did not change between 1716–17 and 2018.
- d) Gas saturation pressures of the andesite inclusions in the 2011 products calculated using the H<sub>2</sub>O and CO<sub>2</sub> content range from 62 to 486 MPa (with averages of 232±132 and 182±36 MPa from the two solubility models). The gas saturation pressures of the dacite–rhyolite inclusions in the 2011 products range from 36 to 199 MPa and the averages obtained using the two solubility models (120±50 and 152±25 MPa) are in good agreement with an estimate (125 MPa) for silicic–andesite magma made by Suzuki et al. (2013b). The gas saturation pressures of the andesite–rhyolite inclusions in the 2018 products range from 74 to 205 MPa (averages of 118±45 and 144±44 MPa by the two solubility models), which is similar to the estimation made for the 2011 felsic magma.
- e) The bulk volatile contents of the magmas associated with the 2011 and 2018 eruptions were estimated based on the volatile content of the melt inclusions and the chemical composition of volcanic gas; the 2011 mixed magma had 4 wt% H<sub>2</sub>O and 0.14–0.70 wt% CO<sub>2</sub>, 2011 mafic magma had 6.2 wt% H<sub>2</sub>O and 0.25–1.4 wt% CO<sub>2</sub>, 2011 felsic magma had 1.9–3.7

wt% H<sub>2</sub>O and 0.025–0.048 wt% CO<sub>2</sub>, and 2018 magma had 2.1–3.0 wt% H<sub>2</sub>O and 0.087–0.10 wt% CO<sub>2</sub>.

- f) The bubble volume and density of the mafic and felsic magmas from the 2011 eruptions, 2011 mixed magma, and 2018 magma were calculated at a pressure range of 5–500 MPa using the bulk volatile content and whole-rock composition of the magmas. The calculations show that the mafic magmas were of lower density than the felsic magma, and that the mafic magma rose into the felsic magma within the magma chamber, promoting mixing. The 2011 magma had a particularly high bubble volume just before eruption (approximately 50 vol% at a pressure of 50 MPa), which caused the subplinian eruption. The 2018 magma had a lower bubble volume (24.4–37.4 vol% at 50 MPa) and thus failed to cause subplinian eruptions.
- g) The mass of degassed magma present was calculated based on the estimated volatile content of the magma, the measured SO<sub>2</sub> flux, and the chemical composition of the magmatic gas emitted from the summit crater. The degassed-magma volume from 2 February 2011 to September 2012 was more than 105 times larger than that of the eruptive products during the same period, suggesting that the degassing of magma in the chamber was due to magma convection in a conduit. This excess degassing decreased the bulk volatile content of the 2011 magma.
- h) The magma ascent and degassing processes of the 2011 and 2017–18 Shinmoedake eruptions are also proposed. Mafic magma with a high volatile content of 6.2 wt% H<sub>2</sub>O and 0.25–1.4 wt% CO<sub>2</sub> ascended from the depth of 19 km before the 2011 eruptions. The mafic magma, with high bubble volume and low density, was injected into and mixed with the felsic magma located at a depth of 5–6 km. The bubble volume of the mixed magma increased to approximately 50 vol% at a depth of 2 km, followed by fragmentation, and resulted in subplinian eruptions on 26–27 January 2011. Degassing of the magma in the chamber due to magma convection in a conduit started in February 2011, together with small eruptions. This excess degassing may have decreased the bulk volatile content of the magma. The mixed magma then proceeded towards chemical equilibrium. The 2018 magma, with a low volatile content of 2.1–3.0 wt% H<sub>2</sub>O and 0.087–0.10 wt% CO<sub>2</sub>, ascended again from the magma chamber, probably due to the injection of new magma into the bottom of the chamber, which likely started in 2017. This magma, with relatively low bubble content, could not cause a subplinian eruption and erupted instead via effusion in March 2018.

### Abbreviations

AIST	Advanced Industrial Science and Technology
BSE	Backscattered electron
bsl	Below sea level
CD	Volatile content of the degassed magma
CM	Volatile content of the magma
DRE	Dense rock equivalent
EPMA	Electron probe micro analyzer
FMQ	Fayalite + Magnetite + Quartz
GIAJ	Geospatial Information Authority of Japan
GSJ	Geological Survey of Japan
JMA	Japan Meteorological Agency
MD	Mass of degassed magma
MV	Mass of volatile material emitted from the crater
NNO	Nickel + Nickel Oxide
SEM	Scanning Electron Microscopy
SIMS	Secondary Ion Mass Spectrometry
XRF	X-ray fluorescence analysis

### Supplementary Information

The online version contains supplementary material available at <https://doi.org/10.1186/s40623-023-01836-1>.

**Additional file 1.** Whole-rock chemical compositions of products from the 1235, 1716–17, 2011, and 2018 eruptions (also shown in Table 2).

**Additional file 2.** Mode compositions and porosities of eruptives from the 2011 and 2018 eruptions.

**Additional file 3.** Description of chemical compositions of minerals and backscattered electron (BSE) images and zoning profiles of olivine, plagioclase, clinopyroxene, and orthopyroxene phenocrysts from the 2011 and 2018 eruptions. **a** Olivine, plagioclase, and clinopyroxene phenocrysts in 2011-2SGP. **b** Orthopyroxene phenocryst in 2011-6VA. **c** Olivine phenocryst in 2011-7VL. **d** Clinopyroxene phenocryst in 2011-7VL. **e** Orthopyroxene phenocryst in 2018-1VGP. **f** Plagioclase phenocryst in 2018-1VGP. **g** Orthopyroxene phenocryst in 2018-2VGP. **h** Clinopyroxene phenocryst in 2018-2VS. **i** Plagioclase phenocryst in 2018-4L2. **j** Orthopyroxene phenocryst in 2018-4L1. **k** Clinopyroxene phenocryst in 2018-4L1. **l** Olivines and orthopyroxenes in 2018-4L2.

**Additional file 4.** Chemical compositions (in weight percent) of ground-mass in eruptives from the 1716–17, 2011, and 2018 eruptions.

**Additional file 5.** Chemical compositions (in weight percent) of melt inclusions in phenocrysts from the eruptives in the 1235, 1716–17, 2011, and 2018 eruptions analyzed in this study.

**Additional file 6.** Magma temperature estimated from two-pyroxene and Fe–Ti oxide thermometry applied to the 1716–17, 2011 and 2018 eruptives.

**Additional file 7.** Magma temperature and oxygen fugacity estimated from Fe–Ti oxide thermometry applied to coexisting Fe–Ti oxide pairs in the 1716–17, 2011 and 2018 products.

**Additional file 8.** Densities of H<sub>2</sub>O and CO<sub>2</sub> gases at temperatures of 870, 928, 944, and 1030 °C calculated by the Modified Redlich–Kwong equation of state (Holloway 1981).

**Additional file 9.** Mode compositions (in volume percent), chemical compositions (in weight percent) and melt viscosities, bubble volumes, and densities of the A1, A2, B1, B2, M1, M2, F1, and F2 magmas at pressure ranges of 5–500 MPa calculated in this study.

**Additional file 10.** Mode compositions (in volume percent), chemical compositions (in weight percent) of melts, and bubble volume and density of mixed magmas (M1 + F1, M1 + F2, M2 + F1, and M2 + F2) calculated in this study.

**Additional file 11.** SO<sub>2</sub> fluxes and chemical compositions of the volcanic gas used for calculating the total amount of degassed magma (Table 5).

**Additional file 12.** Calculation of masses and volumes of 2011 magmas and reference list for additional files.

### Acknowledgements

We thank Dr. Nicolas Vinet for providing data on the Cl/S ratio of ash-leachate from the Shinmoedake eruption. We thank Drs. Nobuo Geshi, Yoshihiro Ishizuka, Ryuta Furukawa, and Masayuki Oishi for providing the rock samples used in this research and their helpful comments. We thank Dr. Isoji Miyagi for helping SIMS measurements. We would like to thank Editage ([www.editage.com](http://www.editage.com)) for English language editing. This manuscript was greatly improved through the helpful comments of anonymous reviewers.

### Author contributions

GS carried out the SEM, EPMA, and SIMS analyses of the eruptive products and the Melts calculation and drafted the manuscript. TO performed the geological survey of the 2018 eruption of Shinmoedake, Kirishima volcano group and collected the samples. OI carried out the whole-rock analyses of the eruptive products. All authors read and approved the final manuscript.

### Funding

Not applicable.

### Availability of data and materials

The datasets used and analyzed during the current study are available from the corresponding author on reasonable request.

### Declarations

#### Ethics approval and consent to participate

Not applicable.

#### Consent for publication

Not applicable.

#### Competing interests

The authors declare no competing interests.

#### Author details

<sup>1</sup>National Institute of Advanced Industrial Science and Technology, Geological Survey of Japan, Central 7, Higashi 1-1-1, Tsukuba, Ibaraki 305-8567, Japan.

Received: 14 March 2022 Accepted: 28 April 2023

Published online: 23 May 2023

### References

- Anderson AT (1973) The before-eruption water content of some high-alumina magmas. *Bull Volcanol* 37:530–552
- Anderson AT, Newman S, Williams SN, Druitt TH, Skirius C, Stolper E (1989) H<sub>2</sub>O, CO<sub>2</sub>, Cl, and gas in plinian and ash-flow Bishop rhyolite. *Geology* 17:221–225
- Anderson D, Lindsley DH, Davidson P (1993) QUILF: a pascal program to assess equilibria among Fe-Mg-Mn-Ti oxides, pyroxenes, olivine, and quartz. *Computers Geosci* 19:1333–1350
- Cashman KV, Mangan MT (1994) Physical aspects of magmatic degassing II. Constraints on vesiculation processes from textural studies of eruptive products. In: Carroll MR, Holloway JR (eds) *Reviews in Mineralogy*, Volume 30: Volatiles in magmas. Mineralogical Society of America, Washington, DC, pp 448–478
- Chiba T, Oikawa T, Sasaki H, Hirakawa Y, Miyabuchi Y, Nakada S (2018) Topography of the 2018 lava flow from Shinmoedake crater, Kirishima Volcanoes, Kyushu, Japan. In: *Abstracts of Volcanol Soc Japan 2018 Fall Meeting* (in Japanese), A1–01, Akita, Japan, 26–30 September 2018
- GSJ/AIST (Geological Survey of Japan, Agency of Industrial Science and Technology) (2017) Report on volcanic gas observation at Shinmoedake, Kirishima volcanoes on 12 October 2017. Paper presented at a meeting of Coordinating Committee for Prediction of Volcanic Eruption, 19 October 2017 (in Japanese)
- GIAJ (Geospatial Information Authority of Japan) (2012) Crustal deformation around Kirishima Volcano. Report of Coordinating Committee for Prediction of Volcanic Eruption 108:197–220 (in Japanese)
- Gerlach TM, Westrich HR, Symonds RB (1996) Preeruption vapor in magma of the climactic Mount Pinatubo eruption: Source of the giant stratospheric sulfur dioxide cloud. In: Newhall CG, Punongbayan RS (eds) *Fire and mud: eruptions and lahars of Mount Pinatubo*, Philippines. Philippine Institute of Volcanology and Seismology, University of Washington Press, Quezon City, Seattle and London, pp 415–433
- Geshi N, Takarada S, Tsutsui M, Mori T, Kobayashi T (2010) Products of the August 22, 2008 eruption of Shinmoedake Volcano, Kirishima Volcanic Group, Japan. *Bull Volcanol Soc Jpn* 55:53–64 (in Japanese with English abstract)
- Ghiorso MS, Gualda GAR (2015) An H<sub>2</sub>O-CO<sub>2</sub> mixed fluid saturation model compatible with rhyolite-MELTS. *Contrib Miner Petrol*. <https://doi.org/10.1007/s00410-015-1141-8>
- Gualda GAR, Ghiorso MS, Lemons RV, Carley TL (2012) Rhyolite-MELTS: a modified calibration of MELTS optimized for silica-rich, fluid-bearing magmatic systems. *J Petrol* 53:875–890
- Hauri E, Wang J, Dixon JE, King PL, Mandeville C, Newman S (2002) SIMS analysis of volatiles in silicate glasses 1. Calibration, matrix effects and comparisons with FTIR. *Chem Geol* 183:99–114
- Imura R, Kobayashi T (2001) Geological map of volcanoes 1:1, Geological map of Kirishima volcano, 1:50,000, Geological Survey of Japan (in Japanese with English abstract)
- Ishizuka O, Geshi N, Kawanabe Y, Ogitsu I, Taylor RN, Tuzino T, Sakamoto I, Arai K, Nakano S (2014) Long-distance magma transport from arc volcanoes inferred from the submarine eruptive fissures offshore Izu-Oshima volcano, Izu-Bonin arc. *J Volcanol Geotherm Res* 285:1–17
- Japan Meteorological Agency (2013) Development of quantitative detection techniques of magma activity and improvement of evaluation of volcanic activity level. *Tech Rep Meteorol Res Inst* 69:152–167. [https://doi.org/10.11483/mritechrepo.69\(inJapanese\)](https://doi.org/10.11483/mritechrepo.69(inJapanese))
- Japan Meteorological Agency (2014) Volcanic Activity of Kirishimayama Volcano –October, 2012 – March, 2013 -. Report of Coordinating Committee for Prediction of Volcanic Eruption. 114:174–199 (in Japanese)
- Japan Meteorological Agency (2019a) Volcanic Activity of Kirishimayama Volcano – September 1, 2017- January 31, 2019a -. Report of Coordinating Committee for Prediction of Volcanic Eruption 132:240–311 (in Japanese)
- Japan Meteorological Agency (2019b) Volcanic Activity of Kirishimayama Volcano – September 1, 2017- September 30, 2018 -. Report of Coordinating Committee for Prediction of Volcanic Eruption 131:280–350 (in Japanese)
- Johnson MC, Anderson AT, Rutherford MJ (1994) Pre-eruptive volatile contents of magmas. In: Carroll MR, Holloway JR (eds) *Volatiles in magmas*, *Reviews in Mineralogy*. Mineralogical Society of America, Washington DC, pp 281–330
- Kato K, Yamasato H (2013) The 2011 eruptive activity of Shinmoedake volcano, Kirishimayama, Kyushu, Japan - overview of activity and volcanic alert level of the Japan meteorological agency. *Earth Planets Space* 65:489–504. <https://doi.org/10.5047/eps.2013.05.009>
- Kawamoto S, Nogami K, Yokokawa M (2011) Crustal deformation associated with the eruption of Shinmoedake volcano, Kirishima volcanic group. *J Geogr Surv Inst* 121:179–182
- Kazahaya K, Shinohara H, Uto K, Odai M, Nakahori Y, Mori H, Iino H, Miyashita M, Hirabayashi J (2004) Gigantic SO<sub>2</sub> emission from Miyakejima volcano, Japan, caused by caldera collapse. *Geology* 32(5):425–428. <https://doi.org/10.1130/G20399.1>
- Kilinc A, Carmichael ISE, Rivers ML, Sack RO (1983) The ferric-ferrous ratio of natural silicate liquids equilibrated in air. *Contrib Mineral Petrol* 83:136–140
- Kita TN, Ikeda Y, Togashi S, Liu Y, Morishita Y, Weisberg MK (2004) Origin of ureilites inferred from a SIMS oxygen isotopic and trace element study of clasts in the Dar al Gani 319 polymict ureilite. *Geochim Cosmochim Acta* 68:4213–4235
- Kozono T, Ueda H, Ozawa T, Koyagichi T, Fujita E, Tomiya A, Suzuki YJ (2013) Magma discharge variations during the 2011 eruptions of Shinmoe-dake volcano, Japan, revealed by geodetic and satellite observations. *Bull Volcanol* 75:695. <https://doi.org/10.1007/s00445-013-0695-4>
- Lowenstern JB (2003) Melt inclusions come of age: volatiles, volcanoes, and Sorby's legacy. In: De Vivo B, Bodnar RJ (eds) *Melt inclusions in volcanic systems, methods, applications and problems*. Elsevier, Amsterdam, pp 1–22
- Maeno F, Nagai M, Nakada S, Burden RE, Engwell S, Suzuki Y, Kaneko T (2014) Constraining tephra dispersion and deposition from three subplinian

- explosions in 2011 at Shinmoedake volcano, Kyushu, Japan. *Bull Volcanol* 76:1–16. <https://doi.org/10.1007/s00445-014-0823-9>
- Miyabuchi Y, Hanada D, Niimi H, Kobayashi T (2013) Stratigraphy, grain-size and component characteristics of the 2011 Shinmoedake eruption deposits, Kirishima Volcano, Japan. *J Volcanol Geotherm R* 258:31–46. <https://doi.org/10.1016/j.jvolgeores.2013.03.027>
- Miyagi I, Hoshizumi H, Suda T, Saito G, Miyabuchi Y, Geshi N (2023) Importance of long-term shallow degassing of basaltic magma on the genesis of massive felsic magma reservoirs: a case study of Aso Caldera, Kyushu, Japan. *J Petrology* 64:egad009. <https://doi.org/10.1093/petrology/egad009>
- Mori T, Kato K (2013) Sulfur dioxide emissions during the 2011 eruption of Shinmoedake volcano, Japan. *Earth Planets Space* 65:573–580. <https://doi.org/10.5047/eps.2013.04.005>
- Nakada S, Nagai M, Kaneko T, Suzuki Y, Maeno F (2013) The outline of the 2011 eruption at Shinmoe-dake (Kirishima), Japan. *Earth Planets Space* 65:475–488. <https://doi.org/10.5047/eps.2013.03.016>
- Nakao S, Morita Y, Yakiwara H, Oikawa J, Ueda H, Takahashi H, Ichianagi M, Ohta Y, Matsushima T, Iguchi M (2013) Volume change of the magma reservoir relating to the 2011 Kirishima Shinmoe-dake eruption – Charging, discharging and recharging process inferred from GPS measurements. *Earth Planets Space* 65:505–515. <https://doi.org/10.5047/eps.2013.05.017>
- Newman S, Lowenstern JB (2002) VolatileCalc: a silicate melt-H<sub>2</sub>O-CO<sub>2</sub> solution model written in visual basic for EXCEL. *Comput Geosci* 28:597–604
- Nishiki K, Oikawa T, Furukawa R, Oishi M, Nakano S, Miyagi I (2013) Amounts of tephra fall deposits from Shinmoedake volcano, during March 2011–February 2012: A preliminary study for immediate estimation of the eruptive mass. *Bull Volcanol Soc Jpn* 58:353–363 (in Japanese with English abstract)
- Ohba T, Hitabayashi J, Nogami K, Kusakabe M, Yoshida M (2008) Magma degassing process during the eruption of Mt. Unzen, Japan in 1991 to 1995: modeling with the chemical composition of volcanic gas. *J Volcanol Geotherm R* 175:120–132. <https://doi.org/10.1016/j.jvolgeores.2008.03.040>
- Oikawa T, Nagai M, Nakada S, Tajima Y, Miyabuchi Y, Shimano T, Miwa T, Iriyama Y, Ishizuka O, Kawanabe Y, Ito J, Maeno F, Hasenaka T, Kawaguchi M (2018) Amounts of tephra fall deposit from Shinmoedake (Kirishima volcanoes) 2018 eruption (Report 1). In: Abstracts of Volcanol Soc Japan 2018 Fall Meeting (in Japanese), P105, Akita, Japan, 26–30 September 2018
- Oishi M, Miwa T, Geshi N, Shinohara H, Vinet N (2013) Magma ascent mechanism during the 2011 eruption of Shinmoedake, Kirishima Volcano, Japan, deduced from the analysis of morphology and texture of volcanic ashes. In: Abstracts of Am Geophys Union Fall Meeting, V21B-2712, San Francisco, California, 9–13 December 2013
- Papale P (2005) Determination of total H<sub>2</sub>O and CO<sub>2</sub> budgets in evolving magmas from melt inclusion data. *J Geophys Res* 110:B03208. <https://doi.org/10.1029/2004JB003033>
- Putirka KD (2008) Thermometers and barometers for volcanic systems. In: Putirka KD, Tepley FJ (eds) *Reviews in Mineralogy & Geochemistry*, Volume 69: Minerals, inclusions and volcanic processes. Mineralogical Society of America, Virginia, USA, pp 61–120
- Roeder PL, Emslie RF (1970) Olivine-Liquid Equilibrium. *Contr Mineral and Petrol* 29:275–289. <https://doi.org/10.1007/BF00371276>
- Saito G, Kazahaya K, Shinohara H, Stimac J, Kawanabe Y (2001) Variation of volatile concentration in a magma system of Satsuma-Iwojima volcano deduced from melt inclusions analyses. *J Volcanol Geotherm R* 108:11–31
- Saito G, Stimac JA, Kawanabe Y, Goff F (2002) Mafic-felsic interaction at Satsuma-Iwojima volcano, Japan: Evidence from mafic inclusions in rhyolites. *Earth Planets Space* 54:303–325
- Saito G, Kazahaya K, Shinohara H (2003) Volatile evolution of Satsuma-Iwojima volcano: degassing process and mafic-felsic magma interaction. In: De Vivo B, Bodnar RJ (eds) *Melt inclusions in volcanic systems, methods, applications and problems*. Elsevier, Amsterdam, pp 129–146
- Saito G, Morishita Y, Shinohara H (2010) Magma plumbing system of the 2000 eruption of Miyakejima volcano, Japan, deduced from volatile and major component contents of olivine-hosted melt inclusions. *J Geophys Res* 115:B11202. <https://doi.org/10.1029/2010JB007433>
- Saito G, Ishizuka O, Ishizuka Y, Hoshizumi H, Miyagi I (2018) Petrological characteristics and volatile content of magma of the 1979, 1989, and 2014 eruptions of Nakadake, Aso volcano, Japan. *Earth Planets Space* 70:197. <https://doi.org/10.1186/s40623-018-0970-x54:303-325>
- Saunders K, Blundy J, Dohmen R, Cashman K (2012) Linking petrology and seismology at an active volcano. *Science* 336:1023. <https://doi.org/10.1126/science.1220066>
- Shinohara H (2008) Excess degassing from volcanoes and its role on eruptive and intrusive activity. *Rev Geophys*. 46:RG4005. <https://doi.org/10.1029/2007RG000244>
- Shinohara H (2013) Composition of volcanic gases emitted during repeating Vulcanian eruption stage of Shinmoedake, Kirishima volcano, Japan. *Earth Planets Space* 65:667–675. <https://doi.org/10.5047/eps.2012.11.001>
- Suzuki Y, Nagai M, Maeno F, Yasuda A, Hokanishi N, Shimano T, Ichihara M, Kaneko T, Nakada S (2013a) Precursory activity and evolution of the 2011 eruption of Shinmoe-dake in Kirishima volcano—insights from ash samples. *Earth Planets Space* 65:591–607. <https://doi.org/10.5047/eps.2013.02.004>
- Suzuki Y, Yasuda A, Hokanishi N, Kaneko T, Nakada S, Fujii T (2013b) Syneruptive deep magma transfer and shallow magma remobilization during the 2011 eruption of Shinmoe-dake, Japan—Constraints from melt inclusions and phase equilibria experiments. *J Volcanol Geotherm R* 257:184–204. <https://doi.org/10.1016/j.jvolgeores.2013.03.017>
- Tomiya A, Miyagi I, Saito G, Geshi N (2013) Short time scales of magma mixing processes prior to the 2011 eruption of Shinmoedake volcano, Kirishima volcanic group. *Japan Bull Volcanol* 75:750. <https://doi.org/10.1007/s00445-013-0750-1>
- Ueda H, Kozono T, Fujita E, Kohno Y, Nagai M, Miyagi Y, Tanada T (2013) Crustal deformation associated with the 2011 Shinmoe-dake eruption as observed by tiltmeters and GPS. *Earth Planets Space* 65:517–525. <https://doi.org/10.5047/eps.2013.03.001>
- Walker GPL (1989) Gravitational (density) controls on volcanism, magma chambers and intrusions. *Aus J Earth Sci* 36:149–165
- Wallace PJ, Carmichael ISE (1994) S speciation in submarine basaltic glasses as determined by measurements of SKa X-ray wavelength shifts. *Am Mineral* 79:161–167

## Publisher's Note

Springer Nature remains neutral with regard to jurisdictional claims in published maps and institutional affiliations.

Submit your manuscript to a SpringerOpen® journal and benefit from:

- Convenient online submission
- Rigorous peer review
- Open access: articles freely available online
- High visibility within the field
- Retaining the copyright to your article

Submit your next manuscript at ► [springeropen.com](https://www.springeropen.com)